

Kinetic modeling of electrodynamic space tethers

by

Jean-Marie A. Deux

Ingénieur diplômé de l'Ecole Polytechnique, France (2003)

Submitted to the Department of Aeronautics and Astronautics
in partial fulfillment of the requirements for the degree of

Master of Science in Aeronautics and Astronautics

at the

MASSACHUSETTS INSTITUTE OF TECHNOLOGY

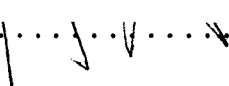
January 2005 [June 2005]

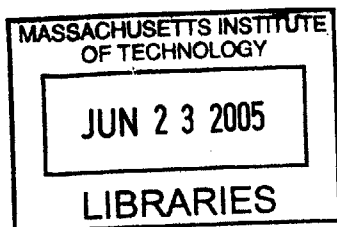
© Massachusetts Institute of Technology 2005, All rights reserved.

Author 
Department of Aeronautics and Astronautics
January 14, 2005

Certified by 
Manuel Martínez-Sánchez
Professor of Aeronautics and Astronautics
Thesis Supervisor

Certified by 
Oleg Batishchev
Principal Research Scientist
Thesis Supervisor

Accepted by 
Jaime Peraire
Professor of Aeronautics and Astronautics
Chair, Committee on Graduate Studies



AERO

Kinetic modeling of electrodynamic space tethers

by

Jean-Marie Deux

Submitted to the Aeronautics and Astronautics
on December 22, 2004, in partial fulfillment of the
requirements for the degree of
Master of Science

Abstract

Electrodynamic space tethers provide propellant-less orbit boosting and de-orbiting of Low Earth Orbit (LEO) satellites. On the one hand, when driven by a current, their interaction with the Earth's magnetic field creates a thrusting Lorentz force. On the other hand, current can be collected from the ionospheric electrons, which also creates a drag. Although the principle is simple, one theoretical issue still has to be addressed: How much current is collected in realistic LEO conditions by a tether of a given section and potential ? The current theories of current collection fail to explain in-space experimental results and previous kinetic modeling was limited from the computational and physical standpoints: wake partly outside the simulation domain, artificial ion/electron mass ratios, single tether, etc.

In the present work we improve our computational techniques and physical model to simulate the tether interaction with the ionosphere. We built a full PIC code which allows to study realistic configurations with the 3V modelling of plasma-probe interactions in external and self-induced magnetic fields. The model uses real electron-ion mass ratio and can simulate domains larger than the wake created in a flowing plasma, thanks to the implementation of a Fast Poisson Solver. Multiwire modelling is available as well to study the interference and efficiency of parallel tether array configurations.

The theory of current collection has then been further developed, by showing the existence of electron trapping around the probe, and evaluating the consequences on current collection. This analysis was supported and discussed through several simulations ran with the PIC code.

We will present results of kinetic studies of current collection for different tether bias, shapes and configurations, including orbit visualizations and statistical diagnostics. Our numerical results will be compared to existing theories of current collection by a moving wire in the OML regime [4]. Eventually, results outside this restricted regime, which are not predicted accurately by any theory, will be discussed.

Thesis Supervisor: Manuel Martínez-Sánchez

Title: Professor of Aeronautics and Astronautics

0.1 Acknowledgements

Many people made my fifteen month stay in Boston at MIT an unforgettable experience. First, let me thank my advisor, Professor Manuel Martínez-Sanchez, for his permanently renewed passion for science, his thorough insights, the last busy times he shared with me, and, above all, his will to let every student find his own best way. Dr. Oleg Batishchev is without any doubt the one who has provided the most long lasting support and the greatest technical help. I would like to thank him for both accepting my ideas and offering me some (better) alternatives.

At MIT, the Space Propulsion Lab, especially my office mates Jose, Murat, Felix and Justin were always able to make me forget the nasty colour of the no-window walls. I will never forget how Jose and I changed the world a thousand times and how Felix, Justin and I discussed with great enthusiasm about the assets of all kinds of coffee.

Here is a great opportunity to show my love and gratefulness to my family, which will one day, I swear, understand what I am doing.

Last but not the least, the French community of the greater Boston area deserves more than a few lines, for the strongest support of my tedious work at MIT. Amandine, Thomas, Serge, mais aussi Antoine, Jeff, Rick, Riadh, Guillaume, Adrien, J-B, Henry, Francois et tous les francais qui ont fait de Boston leur nouveau chez eux, avec crêpes, pinard et fromage a la clé. On se revoit au pays. Petit clin d'oeil à ma princesse des dunes qui a traversé l'océan au bon moment.

Chapter 1

Theory of current collection by a probe in a plasma

1.1 The electrodynamic tether (EDT): a probe in a plasma

Electrodynamic tethers are conducting wires attached to a spacecraft. Unlike mechanical tethers, which are meant to transfer mechanical momentum between two spacecrafts attached at each side of the tether, the EDT is mainly used to interact with the ionospheric plasma (Low Earth Orbit satellites). Bare wires are now thought to be the most efficient way to collect electrons from the ionosphere. A current can be driven from the satellite batteries, which flows through the wire and is finally emitted by a contactor at the end of the tether. The current loop then ends in the conductive ionosphere, back to the tethered satellite. The interaction between this current and the Earth's magnetosphere induces a Lorentz force, which is a thrust when the current is driven by the batteries. Used passively, the conductive wire can collect electrons from the ionosphere, allowing to charge the satellite batteries. In this case, the resulting Lorentz force is a drag, which progressively de-orbit the satellite. A more detailed explanation of the different configurations of interest is given by [1]Onishi (2002) in his background chapter.

Due to the current and the wire resistivity, a local bias is created at the wire surface, which either attracts or repels the charged species in the ionosphere. Then, the particle fluxes into

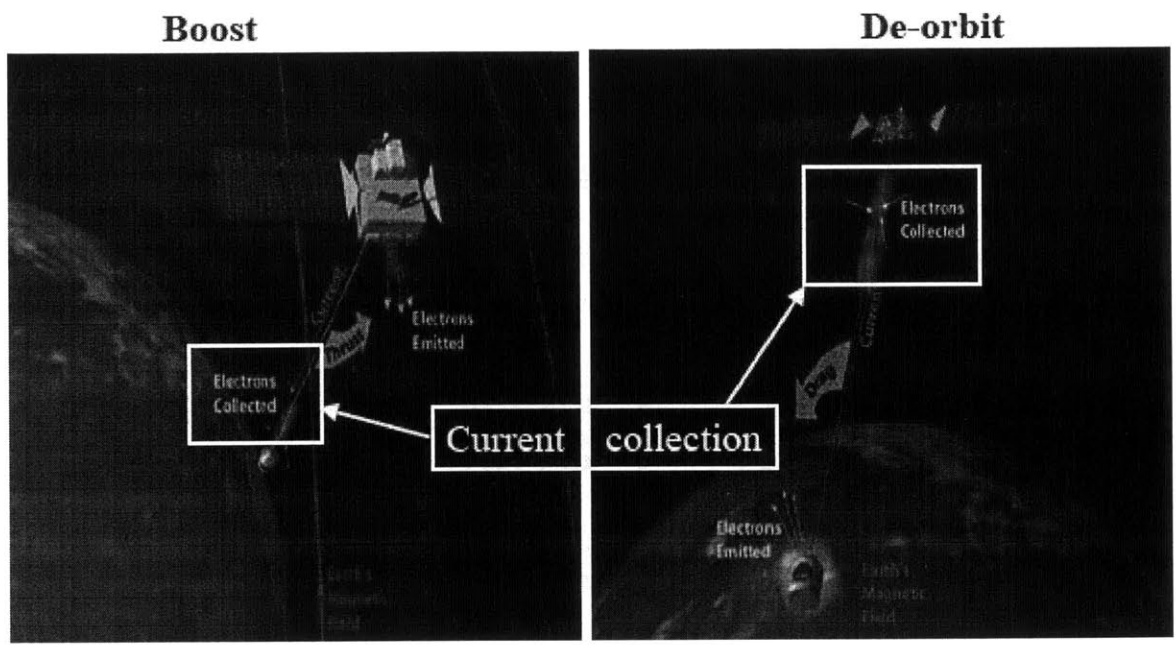


Figure 1-1: EDT can be used in two configurations: active (orbist-boost), where the Lorentz force created by the interaction of the flowing current with the Earth's magnetic field is a thrust, and passive (de-orbit), where it is a drag.

the tether, and thus the collected current, depends on this local bias. Therefore, understanding how a given biased conductive surface interacts and collects the ambient charged particles is then the key of the analysis and efficiency evaluation of EDT. The plasma diagnostics area has been studying for a long time such "plasma-wall interactions", providing some insight in the collection regimes of tethers. However, no accurate theory has been developed so far to understand current collection by tethers in ionospheric conditions, where the satellite orbital velocity and the Earth's magnetic field change the collection regime.

1.2 Plasma sheath theory

1.2.1 Velocity distribution and particle flux

According to the kinetic theory of gases, collisions drive the velocity distribution of species. If the collision frequency is independent of the particle energy, as it is for Coulomb collisions in a plasma (electric interactions between particles), the steady-state unperturbed plasma has a Maxwellian distribution. Consider such unperturbed quasineutral plasma in contact with a given solid material, say a probe (or a tether) for instance. Each species k of the plasma has a particle mass m_k , a particle charge q_k , a density n_k and is at temperature T_k . The isotropic Maxwellian distribution function is:

- in three-dimensional problems :

$$f_k^{3V}(\vec{v}) = \frac{n_k}{(2\pi T_k/m_k)^{\frac{3}{2}}} \exp\left(-\frac{v_x^2 + v_y^2 + v_z^2}{2T_k/m_k}\right). \quad (1.1)$$

The number of particles k in the velocity range $dv_x dv_y dv_z$ is then:

$$dn_k(\vec{v}) = f_k(\vec{v})d\vec{v} = f_k(v)dv_x dv_y dv_z \quad (1.2)$$

Then, the flux of particles k through a surface $x = cst$, or number of particles k hitting the material per unit area and unit time, is:

$$\Gamma_k = \iiint_{v_x \geq 0} n_k(\vec{v}) \vec{v} \cdot \vec{e}_x dv_x dv_y dv_z \quad (1.3)$$

yielding:

$$\Gamma_k = n_k \sqrt{\frac{T_k}{2\pi m_k}}, \quad (1.4)$$

according to [24]Hutchinson, 1987. This flux is of course much higher for light particles like electrons.

- in two-dimensional problems, the distribution is integrated over v_z :

$$f_k^{2V}(v_x, v_y) = \int_{-\infty}^{\infty} f_k^{3V}(\vec{v}) dv_z, \quad (1.5)$$

or :

$$f_k^{2V}(v_x, v_y) = \frac{n_k}{2\pi T_k/m_k} \exp\left(-\frac{v_x^2 + v_y^2}{2T_k/m_k}\right). \quad (1.6)$$

The number of particles k in the velocity range $dv_x dv_y$ is:

$$dn_k(\vec{v}) = f_k(v) dv_x dv_y \quad (1.7)$$

Then, the flux of particles k through a surface, or number of particles k hitting the material per unit area and unit time, is:

$$\begin{aligned} \Gamma_k &= \iint_{v_x \geq 0} f_k^{2V}(v_x, v_y) \vec{v} \cdot \vec{e}_x dv_x dv_y \\ \Gamma_k &= n_k \int_{-\infty}^{\infty} dv_y \int_0^{\infty} \frac{1}{2\pi T_k/m_k} \exp\left(-\frac{v_x^2 + v_y^2}{2T_k/m_k}\right) v_x dv_x, \\ \Gamma_k &= n_k \int_0^{\infty} \frac{1}{2\pi} \exp\left(-\frac{v_x^2}{2T_k/m_k}\right) d\left(\frac{v_x^2}{2T_k/m_k}\right) \times \int_{-\infty}^{\infty} \exp\left(-\frac{v_y^2}{2T_k/m_k}\right) dv_y, \\ \Gamma_k &= n_k \times \frac{1}{2\sqrt{\pi}} \times \sqrt{2T_k/m_k} \frac{1}{\sqrt{\pi}}, \end{aligned}$$

yielding eventually the same flux as a 3V distribution:

$$\Gamma_k = n_k \sqrt{\frac{T_k}{2\pi m_k}}. \quad (1.8)$$

1.2.2 Sheath formation

When the probe is biased at a fixed potential $\Phi_p > 0$, the flux for each particle increases if $q_k < 0$, say for electrons, and decreases if $q_k > 0$, say for ions. The computation of a probe characteristic $\Gamma_k(\Phi_p)$ is actually complex, for it depends on the fine plasma structure around the probe, which is also a function of Φ_p . Figure 1-2 shows a standard probe characteristic, where the overall current into the probe is represented as a function of the bias. Determining particle trajectories to obtain the collected flux Γ_k requires to solve consistently the Vlasov-Poisson equations, which is a non-linear differential equation system involving the potential Φ and the charged species densities ρ_k . Usually, it cannot be solved analytically. In an electrically perturbed plasma, with particle fluxes through the boundaries (external boundaries or probe surface), as it is the case for biased probes, a complicated iterative process is required to obtain the solution.

Nonetheless, a very useful quantity characterizes the extent of the plasma perturbation around the probe. Considering the probe as a potential perturbation in the plasma, the plasma shields this perturbation within a region of size $R_s \sim \lambda_D$ around the probe, where $\lambda_{Dk} = \sqrt{\frac{\epsilon_0 T_k}{q_k^2 n_\infty}}$ is the Debye length of species k , which is the same for every species in the case of single-ionized, mono-temperature species. Therefore, we shall take the electron Debye length λ_{De} as the typical shielding length.

Thus, we can define a perturbed zone around the probe. In this region, quasi-neutrality fails, for (positive) ions are repelled and (negative) electrons are attracted by the probe, which creates a zone around the probe with almost only electrons. The entire region surrounding the probe where the plasma is perturbed is called is referred as the plasma sheath.

Unfortunately, the size and structure of the sheath depend on both the probe bias and geometry and on the plasma parameters. [24] Hutchinson shows that a proper sheath forms

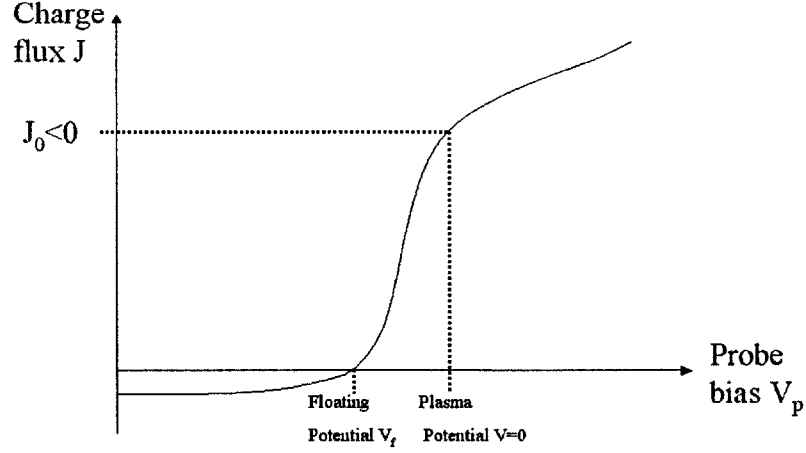


Figure 1-2: Langmuir probe characteristic. The floating potential is defined for $J = 0$. At the plasma potential, the electron flux is higher than the ion flux (for $m_i \gg m_e$), so the total flux J_0 is negative.

only at $\Phi_p > \frac{T_e(eV)}{2} \sim 0.05V$ in the ionosphere F-layer. If this condition is fulfilled, the sheath thickness can be calculated through Poisson's equation, under the assumption that the ion density vanishes in the sheath. For probes with a radius much larger than the electron Debye length:

$$R_s \simeq \left[\sqrt{\frac{e\Phi_p}{T_e} - \frac{1}{\sqrt{2}}} \right]^{\frac{1}{2}} \left[\sqrt{\frac{e\Phi_p}{T_e} + \sqrt{2}} \right] \lambda_{De}. \quad (1.9)$$

[14]Laframboise and Rubinstein (1976) (from section) first gave reliable numerical expressions for the size R_s of the sheath surrounding a thin probe. The dimensionless thickness is:

$$\frac{R_s - R}{\lambda_D} = \left[2.5 - 1.54 \exp\left(-\frac{0.32R}{\lambda_D}\right) \right] \sqrt{\chi_p}, \quad (1.10)$$

which depends on the probe radius and should remain valid for very thin tethers.

More recent results, from both an experimental fit by Choinière and Gilchrist (unpublished) and an analytical derivation by Sanmartín (unpublished) yield the implicit relation:

$$\chi_p = 2.554 \left(\frac{R_s}{\lambda_D} \right)^{\frac{4}{3}} \ln \left(\frac{R_s}{R} \right). \quad (1.11)$$

These semi-analytical and experimental results are compared with measurements from our PIC simulations in Chapter "Current collection: benchmarking with symmetric cases"

Then, following Bohm and Langmuir theory for large probes, we get easily the electron current across the sheath surface, which is a good approximation of the total current into the tether for high bias χ_p and a large probe radius $R \gg \lambda_{De}$:

$$I_{Bohm-Langmuir} = \exp \left(-\frac{1}{2} \right) \pi R_s^2 e n_e \sqrt{T_e/m_e}, \text{ for } R \gg \lambda_{De} \quad (1.12)$$

1.3 The Orbital Motion Limited (OML) regime (cf. [8])

However, the Bohm-Langmuir approximation for the collected current fails for very thin tethers like bare wires, which usually have $R \sim \lambda_{De}$. In this case, a significant part of the flux across the sheath surface is not actually collected by the tether (Figure (1-3)).

When

$$e\Phi_p \gg kT_e + kT_i, \quad (1.13)$$

the repelled particle (ions) density is given by the Boltzmann law:

$$n_i = n_\infty \exp \left(\frac{-kT_i}{e\Phi(r)} \right), \quad (1.14)$$

and is thus fully negligible near the probe. So, ion collection is negligible.

In order to compute the electron current into the probe, a global analysis of their orbits is required. The energy E and angular momentum J of an incoming electron are:

$$E = \frac{1}{2} m_e (v_r^2 + v_\theta^2) - e\Phi(r), \quad (1.15)$$

$$J = m_e r v_\theta. \quad (1.16)$$

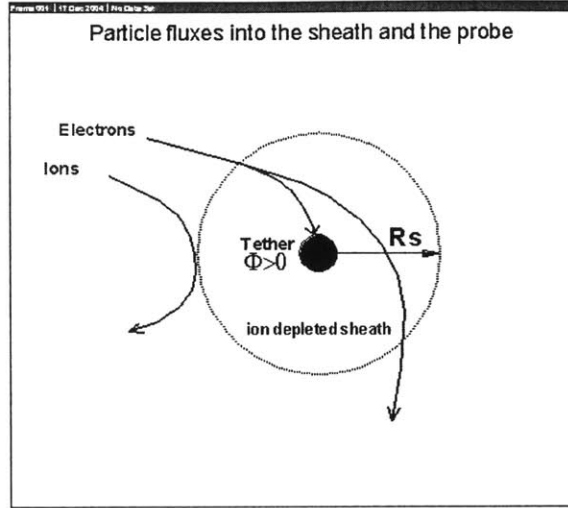


Figure 1-3: When a probe is positively biased in a plasma, an ion-depleted sheath forms. All ions are repelled at the sheath boundary. When the sheath is large enough, the electron flux into the sheath is not fully collected by the probe.

They are assumed to be conserved in a collisionless plasma. Then, the following relations hold:

$$m_e^2 r^2 v_r^2 = J_r(E)^2 - J^2, \quad (1.17)$$

$$J = m_e r v_\theta, \quad (1.18)$$

where:

$$J_r(E) = 2m_e r^2 [E + e\Phi(r)]. \quad (1.19)$$

Then, assuming a Maxwellian distribution faraway, a change of variables $(v_r, v_\theta) \rightarrow (J, E)$ yields:

$$\frac{n_e}{n_\infty} = \iint \frac{\exp(-E/kT_e) dE dJ}{2\pi kT_e \sqrt{Jr^2(E) - J^2}}. \quad (1.20)$$

If $Jr^2(E) - J^2$ becomes once negative outside the probe, the electron is repelled by an effective potential barrier before reaching the tether. Therefore, the integration range for J is only $[0, J_r^*(E) = \min\{J_{r'}(E), r \leq r' < \infty\}] = J_{r_{\min J}}(E)$. $r_{\min J}$, the radius at which the minimum occurs, is in general dependent on the energy E . Electrons in the range $J_r^*(E) < J \leq J_r(E)$ never reach r and must be excluded from the integration. The latter inward trajectories, if traced back in time, turn around at radii between r and $r_{\min J}$ and are therefore unpopulated. For outgoing electrons, the range $[0, J_R^*(E)]$ must also be removed from the integration for it corresponds to particles having disappeared in the probe.

With this restricted integration range, the density can now be written:

$$\frac{n_e}{n_\infty} = \int_0^\infty \left[2 \arcsin \frac{J_r^*(E)}{J_r(E)} - \arcsin \frac{J_R^*(E)}{J_r(E)} \right] \exp(-E/kT_e) \frac{dE}{kT_e}. \quad (1.21)$$

Obviously, the dependence on $\Phi(r)$ through $J_R^*(E)$ would require an iterative solving of Poisson's equation. This analytical complexity disappears if the tether potential induces no effective potential barrier for electrons at the tether surface $r = R$, which means:

$$J_R^*(E) = J_R(E). \quad (1.22)$$

In this case, which is called Orbital Motion Limited (OML) regime, the amount of collected current is maximized and can be written:

$$I_{OML}/I_{th} = \frac{2}{\sqrt{\pi}} \left[\sqrt{\chi_p} + \exp \chi_p \operatorname{erf} c \left(\sqrt{\chi_p} \right) \right] \quad (1.23)$$

where $\chi_p = \frac{e\Phi_p}{kT} \geq 0$ is the normalized tether bias and $\operatorname{erf} c$ is the complementary error function. $I_{th} = pL \times \Gamma_e$ is the thermal current into the cylinder (cross section perimeter p , length L). Γ_e is the electron flux from formula 1.8.

When the tether bias is large compared to the plasma temperature : $\chi_p \gg 1$, the last term of equation 1.23 vanishes:

Then, the following approximation holds:

$$I_{OML}/I_{th} = \frac{2}{\sqrt{\pi}} \sqrt{\chi_p}, \quad (1.24)$$

which yields the simple behavior for $I_{OML} \propto \sqrt{\chi}$. Or, in dimensional form:

$$I_{OML} = 2n_\infty R \sqrt{2e\Phi_p/m_e}, \quad (1.25)$$

which is clearly independent of the temperature.

It turns out clearly that the "no-potential-barrier at r " condition $\{J_r^*(E) = J_r(E), 0 \leq E < \infty\}$ is always verified if $J_r^*(0) = J_r(0)$. Then, from $J_r(0)^2 \propto r^2\Phi(r)$, the OML condition, "no-potential-barrier at R ", can be written more explicitly:

$$R^2\Phi_p \leq r'^2\Phi(r'), \forall r' \geq R. \quad (1.26)$$

According to [19]J.R. Sanmartín and R.D. Estes (1998), this requires the tether radius to be small enough:

$$R \leq R_{max} \simeq \frac{\sqrt{\pi} \left(\sigma_1 \frac{e\Phi_p}{kT_i} \right)^{1/4}}{\sqrt{\kappa} \left(c \ln \sqrt{\sigma_1 \frac{e\Phi_p}{kT_i}} - b \right)^{3/4}} \lambda_{Di}, \quad (1.27)$$

where σ_1 , κ , c and b are given in [19]J.R. Sanmartín and R.D. Estes (1998). This article gives numerical calculations for several $\frac{e\Phi_p}{kT_i}$, which yield $R_{max}/\lambda_{Di} \in [0.75; 1.1]$ at conditions of interest for tethers ($\frac{T_e}{T_i} \sim 1$ and $e\Phi_p/kT_i \in [10; 10^4]$).

1.4 Extension of OML to larger probe radius

First, let us give more insight about the validity of the OML condition. The radial motion of a collisionless electron in a central potential is determined by the following form of Newton's law:

$$m_e \ddot{r} = \frac{d}{dr} \left(-e\Phi(r) + \frac{J^2}{2mr^2} \right) = \frac{dU_{eff}^J}{dr}, \quad (1.28)$$

where $\Phi(r)$ is the local potential, $L = mrv_\theta$ the angular momentum and $U_{eff}^J(r) = -e\Phi(r) + \frac{J^2}{2mr^2}$ is called effective potential. Depending on the shape of Φ and on the value of J , U can take various forms as shown later on Figure 5-13. Assume $U_{eff}^J(r)$ exhibits a bump at r_{bump} , which is higher than its value at the probe surface:

$$U_{eff}^J(r_{bump}) > U_{eff}^J(r = R). \quad (1.29)$$

From Equation 1.28 integrated from R to r_{bump} , this property is written explicitly:

$$\left[-e\Phi(r) + \frac{J^2}{2mr^2} \right]_R^{r_{bump}} > 0; \quad (1.30)$$

Then, electrons coming from infinity (to the right) with an energy $E < U_{eff}^J(r_{bump})$ cannot go through the bump to reach the sheath where they could actually be captured. Therefore, these electrons will never be collected by the probe, because they are blocked by an effective potential barrier. On the contrary, if the bump is always lower than $U_{eff}^J(r = R)$, all electrons which could exist at the probe vicinity (implying a low enough angular momentum J) can be collected. This optimal collection regime is what has been called the OML regime.

Note that, if the condition given by Equation 1.26 is fulfilled, we get:

$$\left[-e\Phi(r) + \frac{J^2}{2mr^2} \right]_R^{r'} \leq \left(1 - \frac{r^2}{R^2} \right) e\Phi_p + \frac{J^2}{2mr^2} - \frac{J^2}{2mR^2}, \forall r' \geq R; \quad (1.31)$$

$$\left[-e\Phi(r) + \frac{J^2}{2mr^2} \right]_R^{r'} \leq \left(1 - \frac{r^2}{R^2} \right) \left[e\Phi_p + \frac{J^2}{2mr^2} \right]. \quad (1.32)$$

Given $e\Phi_p + \frac{J^2}{2mr^2} > 0$ and $1 - \frac{r^2}{R^2} \leq 0$, this implies:

$$\left[-e\Phi(r) + \frac{J^2}{2mr^2} \right]_R^{r_{bump}} \leq 0, \quad (1.33)$$

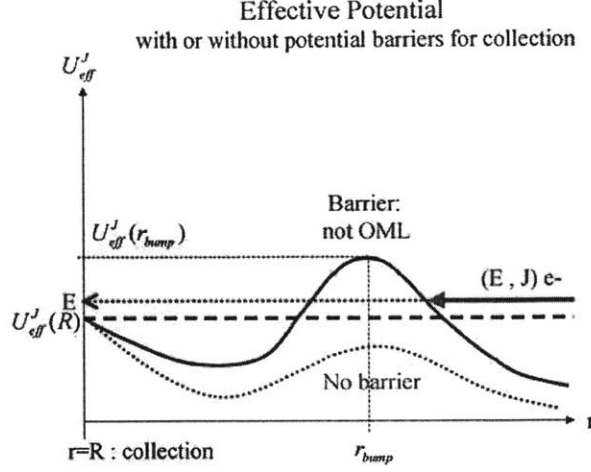


Figure 1-4:

which is not compatible with the "high bump condition" (Equation 1.30).

Although the reverse implication is not true, if a potential fulfills Equation 1.26, it cannot exhibit an effective potential barrier (Figure 1-4), which reduces the electron collection. Therefore, Equation 1.26 is a necessary condition for the potential to be in the OML collection regime.

From Figure and Equation 1.28, it can be seen that for higher tether radii, $U_{eff}^J(r = R)$ gets smaller, which makes it easier for the effective potential bump to overshoot its value at the surface. Above a certain tether radius R_{max} , there exists a certain r_{bump} far away from the probe where $R^2\Phi(R) > r_{bump}^2\Phi(r_{bump})$. This means that some hypothetical trajectories that would hit the probe do not come from the faraway plasma at $r \rightarrow \infty$, but actually from the surface of the probe itself after having turned back at $r \sim r_{bump}$. This happens for incidence angles onto the probe, which are too small: $|\theta| < \theta_{max}$, with $\theta_{max} < \frac{\pi}{2}$.

Therefore, the collected current is reduced by $G(R/R_{max})$, where:

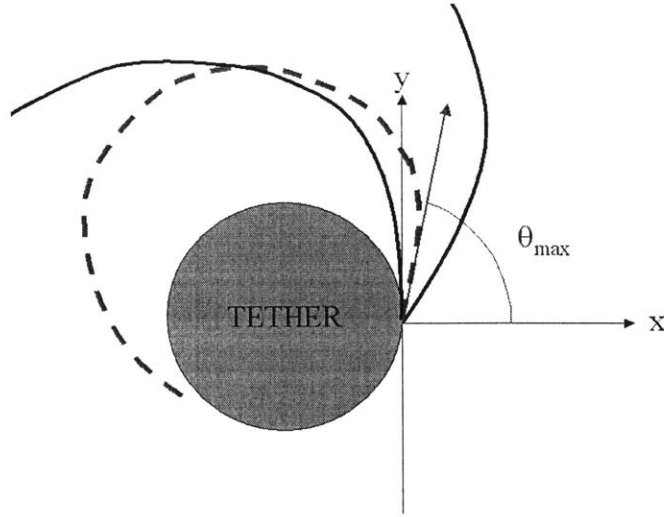


Figure 1-5: When the probe radius is too large, trajectories hitting the probe above a certain incidence, do not come from infinity, but from the probe itself, which means that they cannot be followed by actual particles.

$$I(p, R) = G(R/R_{max}) \times I_{OML}, \quad (1.34)$$

where:

$$G(R/R_{max}) = 1, \forall R \leq R_{max},$$

$$G(R/R_{max}) < 1, \forall R > R_{max},$$

according [19]Sanmartín and Estes (1999). Their Parametric studies show clearly that at any interesting bias and plasma conditions, the collected current in an non-magnetized steady plasma should be at least 80% I_{OML} up to tether radius equal to 3 Debye lengths or more than 2cm (for LEO satellites)), which is very thick for a bare wire. The collection reduction is very weak for tether radii only a few times larger than the Debye length. Then, the weight of the wire, and not its efficiency as a collector, seems to be the most stringent restriction against the use of thick bare wires as ionospheric tethers.

1.5 Advantages of a non circular cross section: thin tape

Note that the OML regime actually holds for arbitrary cross section shapes, as far as the "no-potential barrier" is true all along the surface. In this case, the current density on the surface is simply uniform, which means that the collected current is proportional to the cross section perimeter.

Thin tape cross sections are interesting for bare tethers because:

- their **surface over mass ratio** is much higher than circular cross sections
- their shape avoids almost any **risk of rupture** due to micro-meteorites impacts. Indeed, an impact onto a thin tape would only result in a hole, whereas a tether with a circular cross section could be fully broken, as it happened with. Results similar to the cylindrical case are found for an elliptical thin tape of width $2a$, substituting R by $a/2$. Current collection by a thin tape with $a \leq 2R_{max}$ is found to be only 1% below the OML current ([19]).

1.6 Array of parallel tethers: interference

[22]Sanmartín and Estes (2001) studied analytically the effects of non circular, either convex or non convex tether cross section. Of course, an array of tethers can be considered as a single tether, whose cross section is not convex, not even connected. At a high bias Φ_p , the field near the probe can be solved by Laplace equation (8.1), for space charge effects have negligible effects in some area around the probe. The collected current current is still given by equation (1.34):

$$I = I(p_{eff}, R_{eq}), \tag{1.35}$$

which can be calculated by:

- finding an **effective perimeter** p_{eff} of the array, which takes into account the fact that some trajectories enter the convex envelope of the array without hitting any probe in the array: $R_e = p_{eq} - p_f$, where p_{eq} is the perimeter of the convex envelope of the array and p_f the part of the perimeter where incoming trajectories won't hit any probe inside the

envelope. p_{eff} must be used instead of p in the OML part of the current in equation (1.34).

- computing the **equivalent cross section** radius R_{eq} to be used as R in the OML formula (1.34), which depends on the shape of each single probe cross section and their configuration. This can be done by solving Laplace's equation between the cross section defined by $\Phi(r, \theta) = \Phi_p$ and a circular contour $r = r_\infty$ where $\Phi = 0$, far from the probes. Far enough from the cross section, the potential is approximately cylindrical:

$$\Phi(r) = \Phi_p \frac{\ln(r_\infty/R_{eq})}{\ln(r_\infty/r)}. \quad (1.36)$$

For a general convex envelope, one can use circular harmonics expansion and conformal mapping of the potential in order to find $\Phi(r, \theta)$ and therefore R_{eq} by identification with equation (1.36) at $r \rightarrow \infty$.

Among other relevant cross sections, the equivalent radius of an elliptical thin tape is given in [22] Sanmartín and Estes (2001). And for two nearby circular cross sections, which centers are separated by a distance d , $R_{eq} \simeq 2.06R$, $p_{eq} = (2\pi R + 2d)$ and $p_f = 2d(1 - f)$, with f determined by solving for trajectories in the Laplace near field, in order to exclude trajectories which go between the two tethers within hitting either.

When bringing the wires from large next-neighbour distances to contact (strongest interference), the collection is reduced by 18% for two nearby wires (in contact), $\frac{2}{\pi} = 36\%$ for a long unidimensional array and by $\frac{4}{\pi N}$ for a $N \times N$ two-dimensional array. Size effects (variation of R_{eq}) may also be dramatic, above all for two-dimensional arrays where R_{eq} increases from R to $1.18NR$ approximately, when wires are brought from large next-neighbour distances to contact.

1.7 Effects of the Earth's magnetic field

The closer the magnetic field orientation is to the tether axis, the stronger the magnetic effects. They increase with the two dimensionless parameters R/r_{Le} and $\lambda_D/r_{Le} \propto \frac{B}{\sqrt{n_\infty}}$, with r_{Le} the electron Larmor radius. $\lambda_D/r_{Le} \simeq 1$ in the higher and lower parts of the ionosphere, where

the density drops dramatically, but it remains very small in most of the F-layer where the density remains above 10^5cm^{-3} . But the sheath size, which is a key parameter in the physics of collection, actually depends on the probe potential. Therefore, instead of the Debye length λ_D , [15]Szuszczewicz and Takacs (1979) considered the normalized sheath size R_s/r_{Le} as the relevant parameter. They define three categories: weak, transition and strong magnetic field. Their experiments, in good agreement with Laframboise's calculations for limit cases (Laframboise, 1966 and [14]Laframboise and Rubinstein, 1976) , provide data for the transition field case, corresponding to ionospheric tethers, with various magnetic field directions.

[16]D.Naujoks (2001) used a 1D PIC method to evaluate charge shielding in magnetized plasmas (cf. Boris method and Thomas algorithm) . Instead of a fixed potential at the boundary of a probe, a fixed test charge was used, in the middle of a steady, globally neutral and perpendicularly magnetized plasma. Around a LEO tether (F-layer), $\lambda_D/r_{Le} \simeq 0.3$. Naujoks showed that charge shielding by electrons is significantly perturbed in this case. At $\lambda_D/r_{Le} \geq 1$, the potential shielding is much weaker than in a non-magnetized plasma. This is due to the fact that light particles like electrons are strongly bounded to magnetic field lines and become inefficient in shielding a charge. Nonetheless, for ionospheric ions, $\lambda_D/r_{Li} \simeq 0.7/540 \ll 1$, so they remain able to cross magnetic field lines and shield efficiently a space charge like a tether. As a consequence, even if ionospheric electrons are unable to operate such an efficient shielding as they do in an non-magnetized plasma, the potential distribution around the tether should be less disturbed by the Earth magnetic field effect than expected from pure electron shielding. Nonetheless, [1]Onishi (2002) showed that the potential topology could be significantly affected by magnetic effects in PIC simulations.

[9]Parker and Murphy (1967) first predicted an upper bound for the collected current by a (spherical) charged body in a magnetized plasma:

$$I_{PM}/I_0 = 1 + \sqrt{\frac{8e\Phi_p}{m_e\omega_{ce}^2 R^2}}, \quad (1.37)$$

which yields conveniently in *cgs* units:

$$I_{PM}/I_{th} = 1 + 45.6 \sqrt{\frac{\Phi_p (V)}{B(\text{Gauss})^2 R(\text{cm})^2}}, \quad (1.38)$$

Their result has been widely extrapolated in further theories and as a reference for several experiments and computations, even if their law makes no space-charge considerations. Their method is based on the geometrical analysis of the intersection between particle quasi helicoidal orbits and the probe surface inspired [14]Laframboise and Rubinstein (1976), who built a more accurate theory for cylindrical probes, such as bare wires, and took into account space charge effects due to non-zero λ_{De}/r_{Le} . This case corresponds closely to our simulations; therefore we used their results rather than Parker and Murphy's as a theoretical reference. They define and study two limit regimes, both independent of the detailed form of the sheath potential:

- the **adiabatic limit** $r_{Le}/L_\Phi \rightarrow 0$, when the guiding center approximation becomes valid;
- an **upper bound** for any given non zero r_{Le}/L_Φ .

where $L_\Phi = \frac{\Phi}{\nabla\Phi}$ is the characteristic scale of changes in the sheath potential. Both are obtained in the non-dimensional form:

$$I/I_0 = i(\chi_p, \beta, \theta) \quad (1.39)$$

where $\chi_p = e\Phi_p/(kT_e)$, $\beta = R/r_{Le}$ and θ is the angle between the tether axis and the magnetic field. In order to find the collected current in these limits, the velocity space is considered everywhere on the tether surface and they find out which orbits are not populated, which means that they do not contribute to the electron collection. The theory relies on two major assumptions:

- The existence of a uniform potential neighborhood of the tether, where particle orbits are perfect helices, must be assumed to fulfil the calculations.

- R/λ_{De} and $\beta = R/r_{Le}$ are not simultaneously large enough to produce extrema in the tether sheath potential.

These assumptions can be discussed through the results of our simulations. The upper bound is then found as:

$$i = \frac{2}{\pi} \sin \theta \left(1 + \chi_p + 1/\beta \left\{ \frac{4}{3\sqrt{\pi}} \chi_p^{3/2} + \frac{2}{\sqrt{\pi}} \left[\sqrt{\chi_p} + g \left(\sqrt{\chi_p} \right) \right] \right\} \right), \quad (1.40)$$

where:

$$g(s) = \exp s^2 \int_s^\infty \exp(-t^2) dt \sim \frac{1}{2s} \xrightarrow{s \rightarrow \infty} 0 \quad (1.41)$$

For a high bias, it simplifies into:

$$i_{\max} \simeq \frac{8}{3\pi^{3/2}} \frac{\sin \theta}{\beta} \chi_p^{3/2}. \quad (1.42)$$

With typical ionospheric bare tether parameters ($B = 0.3G$, yielding $r_{Le} = 2.5cm$, $\theta = \frac{\pi}{2}$, $T = 0.1eV$ and $r_{Le} = 2.5cm$ and $R = 0.7cm$), this upper bound is typically $i_{\max} \simeq 1.71\chi_p^{3/2}$. it can be compared to the OML limit $I_{OML} = \frac{2}{\sqrt{\pi}} \sqrt{\chi_p}$:

$$\frac{i_{\max}}{I_{OML}} \simeq \frac{4}{3\pi} \frac{\sin \theta}{\beta} \chi_p \quad (1.43)$$

$$\frac{i_{\max}}{I_{OML}} \simeq 1.52\chi_p \gg 1, \quad (1.44)$$

which means that the magnetic limited upper bound i_{\max} is less stringent than the OML upper bound, unless the magnetic field is very strong (on other planets, such as Jupiter for instance), or θ is small.

The case $\theta = 0$ is studied separately. Although it is of no practical electrodynamic interest, for the Lorentz force when $\vec{B} \parallel \vec{i}$, the corresponding results are useful to benchmark our code. The upper bound and adiabatic limit current are then given respectively by equations

(25) and (26) in [14]Laframboise and Rubinstein (1976) (see also Amemiya and Dote, 1969). We used numerical applications from them to discuss our results with $\vec{B} = B_z \vec{e}_z$, parallel to the tether. Still working in velocity space, they eventually predict a linear dependence of the current reduction on B :

$$i = i(\theta = 0) - C(\theta, \chi_p) \beta, \quad (1.45)$$

It has been found later on that there is a threshold body potential beyond which this upper bound can almost be reached.

On the one hand, this threshold was found analytically, assuming a potential $\Phi(r) \propto r^{-n}$ in the non-neutral sheath around the probe. Sonmor and Laframboise (1991) took $n = 1$ and found that the upper bound is approached for very large potential only. But Singh and Chaganti (1994), using $n = 3$, showed that moderate potentials (a few V) might be enough to reach the Parker-Murphy upper bound.

On the other hand, Singh et al. (1994) showed through a three-dimensional PIC simulation ($m_i/m_e = 100$ or 400) that moderate body potentials ($\sim 8V$ only) already allow collected currents closely given by the upper bound values. Indeed, for $e\Phi \gg m_e \omega_{ce}^2 R^2$, most electrons entering the sheath around the tether are demagnetized by high perpendicular electric field gradient and thus quickly collected. Numerical applications yield $\Phi_{\min} \sim 1V$ if $R \sim 1mm$. This means that the Parker-Murphy law is an excellent approximation for standard ionospheric tethers. Nonetheless, if the body size R is too small, only a slight remaining magnetization might deflect the electron trajectories sufficiently, such that many of them enter the sheath without being collected. This effect, relevant for a very thin wire, was not quantified in the previous PIC simulation.

1.8 Effects of the self induced magnetic field

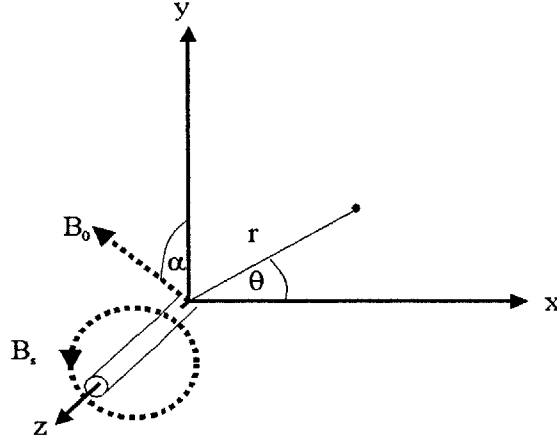


Figure 1-6: Earth's magnetic field (in the y-z plane) and current-induced magnetic field.

1.8.1 Magnetic field topology and collection area

magnetic field lines

The development of tether systems aims at increasing their current, which produces a magnetic field of proportional amplitude around the wire. As a result, the current-induced magnetic field can be larger than the Earth's magnetic field in a significantly wide region around the tether. In this region, the Larmor radius of the particle is decreased, which alters the critical ratios $\frac{\lambda_D}{r_{Le}}$ and $\frac{R}{r_{Le}}$. Even more relevant could be the complete transformation of the magnetic field topology near the tether. [11]Khazanov et al. first analyzed the role of the current-induced magnetic field in different regimes of collection.

The static magnetic field around a wire flown by a current I is merely given by Ampere's law in cylindrical coordinates (r, θ, z) :

$$\vec{B}^s = B^s \vec{e}_\theta \quad (1.46)$$

with $B^s = \frac{\mu_0 I}{2\pi r}$ (in IS units) or $B^s = \frac{2I}{cr}$ (cgs units), where c is the velocity of light.

Adding a homogeneous Earth's magnetic field $\vec{B}_0 = B_0 \cos \alpha \vec{e}_y + B_0 \sin \alpha \vec{e}_z$

(cf. Figure 1-6) yields:

$$\vec{B} = B_0 \cos \alpha \sin \theta \vec{e}_r + (B^s + B_0 \cos \alpha \cos \theta) \vec{e}_\theta + B_0 \sin \alpha \vec{e}_z. \quad (1.47)$$

In such a field topology, a magnetic field line equation in the (x-y) plane can be obtained as (cf. Equations 2.58)

$$\xi = r^* \ln \frac{r}{r^*} + r \cos \alpha \cos \theta = cst \quad (1.48)$$

where:

$$r^* = \frac{\mu_0 I}{2\pi B_0}. \quad (1.49)$$

There exists a separatrix $\xi = \xi_s$, which divides space into two regions:

- external region where the (x, y) projections of the magnetic field surfaces are open and tend to straight lines far from the wire;
- internal region around the wire, where these projections are closed and tend to circles in the tether vicinity.

The separatrix is the curve where the projection of the Earth's magnetic field onto (x, y) and the current-induced field are equal, which happens at $\theta = \pi$ for:

$$B_0 \cos \alpha = B^s(r) \Leftrightarrow r = r^*. \quad (1.50)$$

So:

$$\xi_s = -r^* (1 + \ln \cos \alpha) \quad (1.51)$$

and eventually:

$$\ln \left(\frac{r}{r^* / \cos \alpha} \right) + \frac{r}{r^* / \cos \alpha} \cos \theta + 1 = 0, \quad (1.52)$$

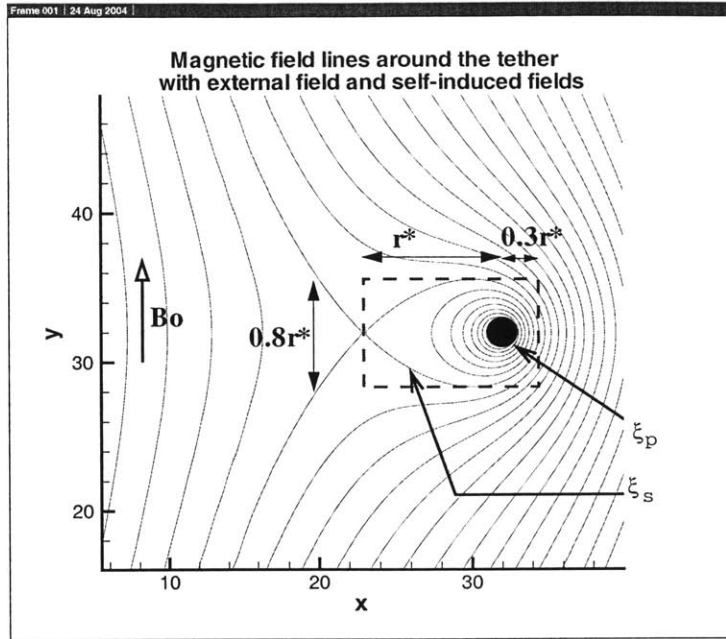


Figure 1-7: Magnetic field lines for a 10A current with the length unit $\lambda_{De} = 0.7cm$

r^* turns out to be the characteristic size of the region inside the separatrix. Indeed, the separatrix extends from $-r^*$ to $0.3r^*$ along x and from $-0.4r^*$ to $0.4r^*$ along y .

The criterion for strong current induced effects requires the plasma sheath to lie somehow inside the separatrix, so r^* actually is a new relevant characteristic length of the system to define various collection regimes.

Applying the motion conservation laws for particles under the assumption that they do not face any potential barrier ([11]Khazanov et al., 2000), just as was done to compute the OML current in the isotropic case, allows to determine the region of electron collection. With the present magnetic field topology, an electron must come from infinity, reach the separatrix and cross it to get to the wire in order to be collected (if the 3D end-effects are neglected).

For electrons coming from the weaker magnetic field side ($x \leq 0$ here), the momentum along z is minimum at the separatrix (where the magnetic field is weakest). [11]Khazanov et al. show then that the ($x \leq 0$) collection region is determined by the collection to the separatrix. This region is the set of all magnetic field lines $\xi^+ = \xi_0^+$, where:

$$\xi_0^+ \geq \xi_s^-(E) = \xi_s - \frac{1}{\omega_c} \left(v_{z0} + \sqrt{(2/m)(E - e\Phi_s)} \right). \quad (1.53)$$

On the larger magnetic field side ($x \geq 0$ here), the separatrix most often is not a potential barrier anymore for electrons. We thus assume that the region of collection for the separatrix is not less than for the wire on this side, which was never the case on the other side ($x \leq 0$). Analytically, we have:

$$\xi_p^+(E) := \xi_p + \frac{1}{\omega_c} \left(v_{z0} + \sqrt{(2/m)(E - e\Phi_p)} \right) \leq \xi_s^+(E). \quad (1.54)$$

This condition depends very weakly on the particle energy if the tether bias is much larger than the thermal energy ($\sim 0.1eV$) and is usually verified. So, some electrons reaching the separatrix, may miss the wire surface. The ($x \geq 0$) collection region is then the area where particles are collected by the wire itself. This region is the set of all magnetic field lines $\xi^- = \xi_0^-$ verifying:

$$\xi_0^- \leq \xi_p^+(E), \quad (1.55)$$

where $\xi = \xi_p$ is the tether surface, at potential Φ_p .

Thus, the total collection region for particles with energy E is defined by:

$$Coll(E) = \left\{ (x_0, y_0) / \xi_s^-(E) \leq \xi_0 = r^* \ln \frac{\sqrt{x_0^2 + y_0^2}}{r^*} + x_0 \cos \alpha \leq \xi_p^+(E) \right\}. \quad (1.56)$$

A relevant parameter to characterize this region is its width $\Delta x_\infty(E)$ far from the probe ($y_0 \rightarrow \pm\infty$):

$$\Delta x_\infty [Coll(E)] = \frac{\xi^+(E) - \xi^-(E)}{\cos \alpha}, \quad (1.57)$$

Figure 1-8 shows the field topology and the whole collection region at a given energy as well.

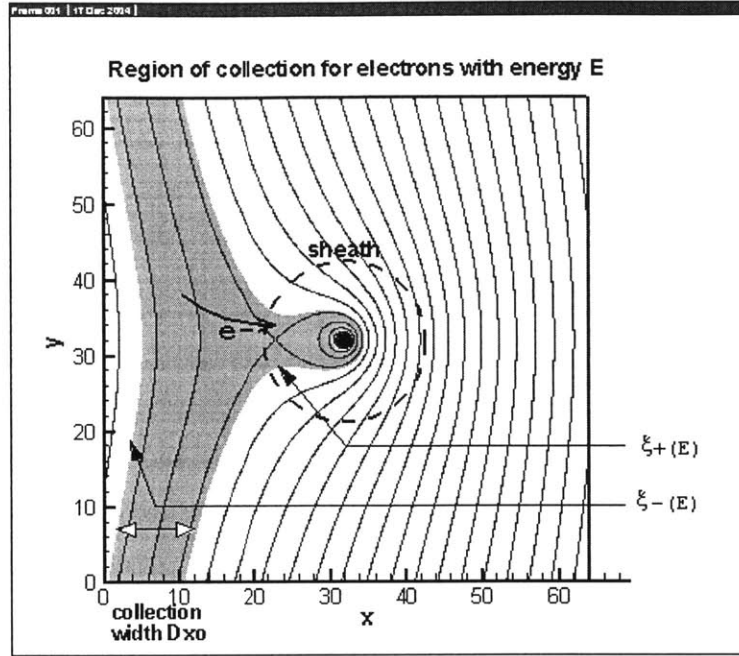


Figure 1-8: If the separatrix size is smaller than the sheath radius, the "magnetic bottle" approximation holds and a collection region can be defined at every electron energy.

Knowing the width of the collection region allows to calculate the upper bound for the collected electron current with this field topology:

$$i = \frac{\xi_w - \xi_s}{\pi R} + \frac{1}{\beta \pi^{\frac{3}{2}}} 3 \left(\sqrt{\chi_p} + \sqrt{\chi_s} \right) + \sqrt{\frac{\pi}{4}} (3 - 2\chi_s) \left(\text{erf } c\sqrt{\chi_s} \right) \exp \chi_s + \sqrt{\frac{\pi}{4}} (3 - 2\chi_p) \left(\text{erf } c\sqrt{\chi_p} \right) \exp \chi \quad (1.58)$$

with i , β , χ_p and χ_s defined as in equation 1.40 and $\text{erf } c(x) = \frac{2}{\sqrt{\pi}} \int_x^{\infty} \exp(-t^2) dt$

1.8.2 Effects on collected current

The refined criterion used by [12]Khazanov et al.(2001) to estimate self-induced current reduction is:

- full collection if $2\pi R_s \geq p_s$, where p_s is the perimeter of separatrix, which yields numeri-

cally:

$$R_s < \frac{0.514}{\cos \alpha} r^*. \quad (1.59)$$

- reduced collection, by a coefficient $\varepsilon \leq 1$, otherwise:

$$\varepsilon = \frac{2g}{3\sqrt{\pi}} \exp(-g^2) + \operatorname{erf} c(g), \quad (1.60)$$

$$g = -\frac{\omega_c r^*}{2} \sqrt{\frac{m}{2T}} \left[(1 + \ln \cos \alpha) + \frac{\xi_s}{r^*} \right], \quad (1.61)$$

which derivation can be found in [12]Appendix A, from the collection width 1.57.

[12]Khazanov et al. (2001) [13]Sanmartín and Estes (2002) eventually concluded from their parametric study on self-field effects, based on the previous modelling, that they are:

- fully negligible in power generation regime;
- significant in thruster regime: around $\sim 15\%$ current reduction for long tethers;
- always negligible for thin tapes and round tethers conductive in a layer;
- increasing with respect to the wire radius and plasma density .

1.9 Effects of the orbital velocity

The 2D-OML law (1.23) does not actually require rotational symmetry. Nonetheless, the OML regime cannot be applied when the plasma flow is mesosonic as is the case for an orbiting tether in the ionosphere. Indeed, with a $8km/s$ orbital velocity, the ion flow onto the probe is hypersonic (Mach number $M_i > 10$) and the electron flow subsonic ($M_e < 0.1$), which seems to result in a paradox: In this case, Laframboise and Parker showed that the ion density n_i should be more than n_∞ in a broad region on the ram side of the flow, while the electron density

cannot exceed n_∞ . Such an effect would violate quasi-neutrality in a domain which would be much larger than R_s , whereas R_s is supposed to characterize the extent of the perturbation.

The resolution of the previous paradox lies in the existence of significant collisionless electron trapping, a process which compensates the original quasi-neutrality breakdown (cf.[34] and [1]). A significant portion of electrons have an energy $E < 0$. These accumulate around the moving probe, for they can't escape to infinity (at least in a short time scale of the order of ω_{pe}^{-1}). So they could be finally captured by the probe but were not taken into account in the OML calculation (the E integration range was $[0, \infty]$). Could this phenomenon explain a possible departure from the OML regime when the probe is in high-speed motion? Further discussion on trapping is given in the Chapter "Particle Trapping".

[17]J.G. Laframboise (1996) eventually constructed a conceptual model of the disturbed surroundings of a biased *spherical* probe in a flowing magnetized plasma, which fits pretty well the TSS-1 measurements. Although he focused on conditions similar to our simulation: orbital velocity $8km/s$ (ion kinetic/ram energy $5.35eV$), $T_e = T_i = 0.1eV$ and $n_\infty = 10^5 cm^{-3}$, the TSS-1 has a different geometry and is much larger ($1.6m$ diameter sphere) than our bare cylindrical tether ($< 1cm$). He showed that the orbital velocity is responsible for an elongation of the collection region in the upstream direction. The satellite motion creates indeed a large intersection between this zone and the electron depletion zone, where electrons are very sensitive to the tether positive bias and are accelerated toward it. This effect increases the Parker-Murphy area of collection by a factor 2. The Parker-Murphy upper bound for collected current must then be doubled. He then studied the departure from symmetry due to a magnetic field, defining:

1. an **ion enhancement region**, where ions slow down when approaching the probe (so their density doubles). They are then suddenly reflected on:
2. a **magnetic pre-sheath**, whose boundary is defined by quasi-neutrality. The potential inside is above $7V$, more than the mean ion kinetic energy. Laframboise regards its forward boundary as the effective electron absorber for the probe. Indeed, ions do not penetrate it, so electrons reaching this boundary are quickly accelerated towards the probe and collected.

3. An electrostatic **sheath** also exists very near the tether, but it is assumed to remain entirely in the collection zone, defined by the magnetic pre-sheath.

Numerical applications using the OML approximation, with the pre-sheath boundary instead of the probe contour yield an electron flux increased by a factor 3 approximately compared to the thermal flux used by Parker and Murphy. Thus, the total collected current in a $0.3G$ magnetized and $8km/s$ flowing plasma turns out to have an upper bound:

$$I \simeq 6I_{PM}, \tag{1.62}$$

which fits much better the TSS-1 current. This theory has been worked out further, with no great improvement in the numerical comparisons with space measurements. In the case of thin bare wires, this upper bound, is of the order $I_{Max} \simeq 20I_{OML}$, which means that there is room for collection enhancement in ionospheric conditions compared to the OML regime. Such a huge departure from the OML regime seems improbable, though.

1.10 Other phenomena increasing the current collection

A full thermalization in the magnetic pre-sheath 2 should increase the collection. Radio Frequency (RF) heating from the tether, used as an antenna, could enhance these oscillations and produce such a thermalization. Very little work has been done on this collection enhancement method. Some basic 1D PIC simulations and experimental work by [23]Choinière et al. show that the amount of collected current can be higher than the OML current (cf. Equation 1.23) if the plasma is excited by Radio-Frequency waves. Their simulations show that the excitation of the plasma by waves emitted from the tether make electrons scatter off of their standard OML trajectories and increases their probability to be collected. The time-averaged width of the plasma sheath then turns out to be higher than without wave emission. A large current enhancement, up to 750%, has been reached both numerically and experimentally at some frequencies slightly below the plasma frequency $f_{pe} \simeq 200MHz$ in their case. Nonetheless,

probably too much RF power would be spent by operating in this resonant layer. [23]Choinière et al. found out that the "lowest cost "of current enhancement occurs at a frequency $f = 90$ Hz, well below the resonance frequency. The current collection is then enhanced by 9% for every Watt of RF power per meter of tether length.

More simulations, including magnetic and flow, might help understand the mechanism of this enhancement, may be related to the Bohm instability. They may also find the best affordable efficiency.

Chapter 2

Specifications and basic benchmarking of the code

2.1 PIC (Particle-In-Cell) method

The Particle-In-Cell method has been used widely to model low density plasmas, when fluid codes become useless. Charged plasma species (ions and electrons) are modelled as individual macro-particles (each macro-particle represents a large number of real particles). Particles move in the plasma using Newton's law of motion and self-consistently calculated electric fields resulting from both applied voltages and inter-particle Coulomb forces. Electric fields are solved self-consistently due to the superposition of external (applied) fields and internal fields from charge distributions. This is done by using a non-physical grid across the plasma (the "cell" part of the name) and determining the charge density at each grid position by assigning particles to the grid according to their position, and a weighting scheme. Once the charge density at the grid positions is known the potentials can be calculated using Poisson's equation. Then the electric fields at the grid can be determined and finally fields at the particle positions are determined using an inverse weighting scheme. Particles can then be moved via Newton's equations, using a leap-frog finite differencing method, on a continuous position space (Particles do NOT move from one cell to another by discrete steps !)

Particle-In-Cell Method

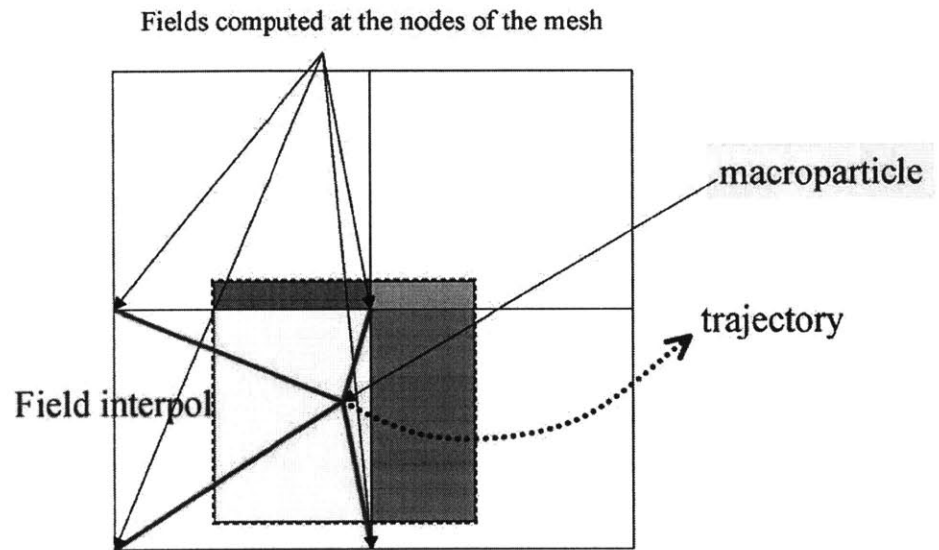


Figure 2-1: The space charge fields are computed at each node, from the weighted contribution (coloured areas) of the macroparticle in each of the 4 partly covered cells. Then, the macro-particle is moved according to the interpolated value of the fields at its location.

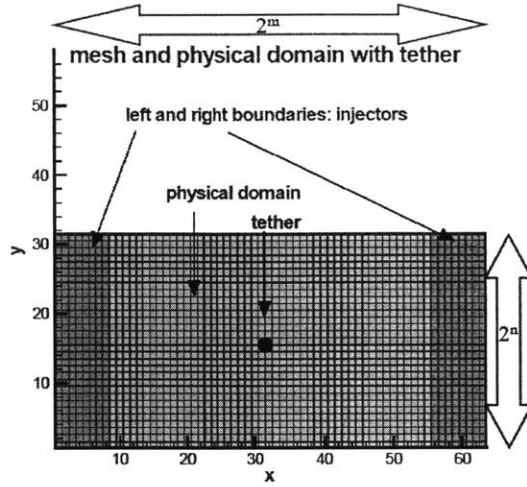


Figure 2-2:

2.2 Specifications of our model

2.2.1 Domain

- The **two-dimensional mesh**, which is a $n_{x \max} \times n_{y \max}$ cell grid, is built into three parts (cf. Figure 2-2):
- The **physical domain**, simulating the ionospheric plasma and the tethers
- Two thin **injection zones** at the left ($n_x \leq 10$) and at the right ($n_x \geq 10$) of the physical domain, which provide particles to the physical domain at each time step, according to well-chosen velocity distribution functions.

2.2.2 Successive steps

1. **Initialization** of the macro-particles in the domain

In the center of each cell of the mesh, the same number of macro-electrons and simply ionized macro-oxygen ions is created, at various velocities, according to the discretization of the velocity distribution that is chosen (cf. Figure 3-1 and related section).

2. Computation of the electric potential and field by the **Fast Poisson Solver**

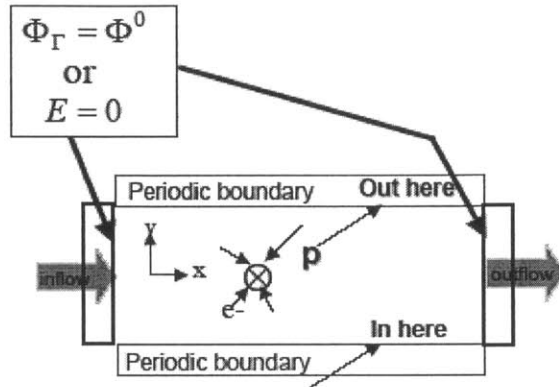


Figure 2-3:

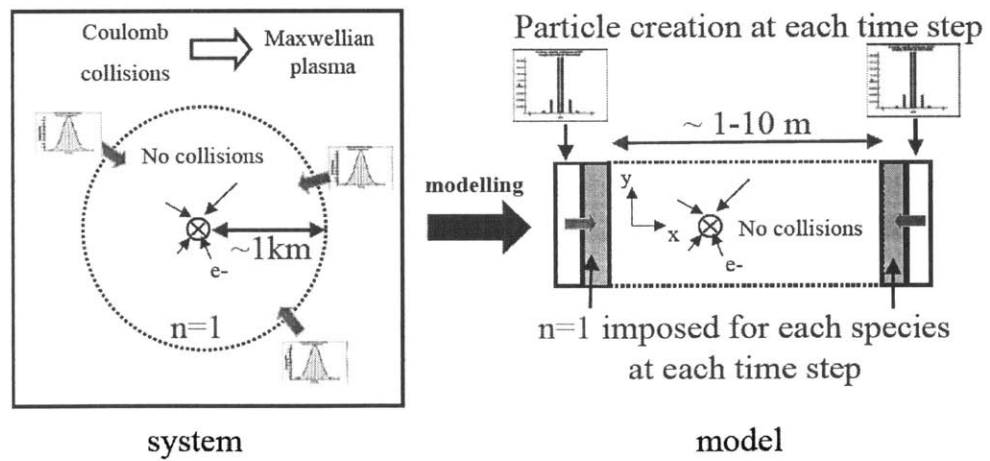


Figure 2-4: In the ionosphere, the plasma around the tether is Maxwellized by Coulomb collisions. The mean free path being very large, more than 1km or $10^3 \lambda_{De}$, we cannot introduce collisions efficiently in our numerical model and must artificially inject a Maxwellian plasma into the domain.

An innovation of our code is the implementation of a Fast Poisson Solver, which allows to reduce dramatically the computation time required to solve the Poisson equation (here in cgs units):

$$\Delta\phi = -4\pi\rho \quad (2.1)$$

everywhere on the mesh. The Fast Fourier Transform method allows the computation of the electric potential at each node of a $2^k \times 2^l$ (k, l positive integers) mesh, from the given charge density everywhere, by diagonalization of a tri-diagonal matrix, which is extremely quick compared to a standard solver.

3. Particle motion: 3 step finite-difference scheme

4. Particle suppression in the sinks and injectors

All particles whose straight trajectories during the time step cross the tether boundary (defined analytically) are destroyed. All particles which lie in one of the two injector regions at the end of their motion are destroyed as well.

5. Particle creation in the injectors

New particles are then created again in the injector regions, through the same process as in step 1, except that this creation occurs only in the two injectors.

2.2.3 Fast Poisson Solver on a uniform structured grid

The main advantage of Dr. Batishchev's code, compared with previous models such as the one build by [1], is the Poisson Solver, which uses the **Fast Fourier Transform (FFT)** technique to compute the local electric field from the space charge throughout the domain, given some chosen boundary conditions.

The 2D Cartesian Poisson equation is written, still in cgs units:

$$\frac{\partial^2\phi}{\partial^2x} + \frac{\partial^2\phi}{\partial^2y} = -4\pi\rho, \quad (2.2)$$

which can be discretized on a (p, q) grid. Let us assume $p = q$ in the sake of notation simplicity. The discretization scheme in matrix notation is written:

$$J.V + V.J = h^2 F, \quad (2.3)$$

where $J = Tridiag_p(2, -1, 2)$ is the differential operator (central differences scheme), $V = [\phi(ih, jh)]_{i,j}$, the potential matrix, $F = [-4\pi\rho(ih, jh)]_{i,j}$ the space charge source term matrix and $h = \frac{1}{p+1}$ the spatial step.

The diagonalization of J for $p \times p$ square matrices is:

$$J = Q_p \cdot \Delta_p \cdot Q_p,$$

where $Q_p = [\sqrt{2h} \sin(ij\pi h)]_{i,j} = \sqrt{2h} S_p$ verifies $Q_p^2 = 1$ and $\Delta_p = Diag[4 \cdot \sin^2(i\pi h/2)]$.

After multiplying on each side by Q_p , the discretized Poisson equation becomes:

$$\Delta_p \cdot W + W \cdot \Delta_p = h^2 B, \quad (2.4)$$

with $W = Q_p \cdot V \cdot Q_p$ and $B = Q_p \cdot F \cdot Q_p$.

Since Δ_p is diagonal with eigenvalues $\lambda_i = 4 \cdot \sin^2(i\pi h/2)$, we get directly $W = [h^2(\lambda_i + \lambda_j)B_{i,j}]$. Eventually, the potential matrix can be obtained from the reverse relation: $V = Q_p \cdot W \cdot Q_p$.

Therefore, in order to find V , we need to do the matrix multiplications $S_p \cdot A$ and $A \cdot S_p$ for some matrix A . The matrix product $S_p \cdot A$ is called the Direct Sine Transform (DST) of A . Then, $A \cdot S_p$ is the transpose of the DST of A^T .

If we define $F_{N,M} = \left[\exp\left(-\frac{2i\pi}{N}\right)^{(j-1)(k-1)} \right]_{j,k} \in \mathbb{R}^{N,M}$, the so-called Fourier matrix, and $z(x) = (0, x_1, \dots, x_p, 0, -x_p, -x_{p-1}, \dots, -x_1)^T \in \mathbb{R}^{2p+2}$ for any vector $x \in \mathbb{R}^p$, the following relation holds:

$$(S_p \cdot x)_k = \frac{i}{2} (F_{2p+2} \cdot z(x))_{k+1}, \forall k = 1, \dots, p. \quad (2.5)$$

So, if we find a way to compute easily FC , where $c_{i,j} = z(a_{i,j})$, we get the product SA . It turns out that F has a nice recursive property, which allows to compute this product at order $2p$ from the order p :

$$F_{2p}F_{2p} = \begin{array}{|c|c|} \hline F_p & D_p F_p \\ \hline F_p & -D_p F_p \\ \hline \end{array}, \quad (2.6)$$

where $D_p = \text{Diag} \left(1, \exp \left(-\frac{2i\pi}{N} \right), \left[\exp \left(-\frac{2i\pi}{N} \right) \right]^2, \dots, \left[\exp \left(-\frac{2i\pi}{N} \right) \right]^{p-1} \right)$ and

$P_N = (e_1, e_3, \dots, e_{N-1}, e_2, e_4, \dots, e_N)$ is the matrix which reorganizes the columns of F_{2p} , such that the even columns appear before the odd ones.

This implies that $F_{2p}.z$ can be computed directly from $F_{2p}.w_1$ and $F_{2p}.w_2$, with $w_1 = (z_1, z_3, \dots, z_{2p-1})^T$ and $w_2 = (z_2, z_4, \dots, z_{2p})^T$. z has to be defined for each matrix A that has to be multiplied by S . The relations 2.5 and 2.6 allow us to calculate the corresponding product $S_{2p}.A$ from $S_p.A_{\text{even}}$ and $S_p.A_{\text{odd}}$.

This recursive method is called Fast Fourier Transform (FFT) and is much quicker than standard Fourier Transform, as shown by the following complexity calculations: Let x_k be the complexity when $N = 2^k$ for square matrices. At the order N , we need two FFTs of order $N/2$ and a multiplication with the diagonal matrix $D_{N/2}$. So, $x_k = 2x_{k-1} + Cte.2^k$. Since $x_0 = 0$, the recurrence on k yields:

$$x_k = Cte.N.\log_2 N,$$

instead of $O(N^2)$ if direct multiplications are used to compute $F_N.z$.

Here is a summary of the different steps in the process:

- Compute B from F , which requires one multiplication by S and one by S^T , so $2p$ FFTs of order p (one for each column of S and one for each column of S^T).
- Compute W from B , by only p^2 multiplications.
- Compute V from W , which requires one multiplication by S and one by S^T , so $2p$ FFTs of order p (one for each column of S and one for each column of S^T).

When $p \neq q$, a total of $2p$ FFTs of order q and $2p$ FFTs of order q is required, yielding an overall complexity $O[n \log_2 n]$ instead of $O\left[n^{\frac{3}{2}}\right]$ when a simple Cholesky factorization is used, where $n = p \times q$ is the size of the linear system.

Of course, as may be clearly seen in this presentation, it makes it much more difficult and costly when the grid length and width are not powers of two or not uniform. Therefore, in order to be much faster, our Poisson Solver computes the electric potential on a uniform ($2^m \times 2^n$) grid with the FFT technique. It might seem restrictive to use a uniform grid, especially when grid refinement may be required in some regions of the domain, such as the tether vicinity. Some mappings actually allow to use FFT on a non-uniform grid. A cylindrical grid with smaller cells close to the tether (one singularity) would be possible to implement. Nonetheless, when several tethers are simulated, requiring several singularities in the grid, no mapping allowing FFT is available. We thus decided to keep the simplest uniform grid, which allows multi-tether simulations. Moreover, with a rectangular uniform grid, the electric field interpolation between the nodes of the grid is extremely simple to write.

Given the fact that most of the computation time in a PIC simulation is due to the Poisson solver, our Fast Poisson Solver is a great asset to reduce the total computation time of the simulations, and above all, to allow **much larger simulated domains**.

2.2.4 Particle motion

Each charged macro-particle is subjected to the electromagnetic Lorentz force:

$$\vec{F} = q \left(\vec{E} + \vec{v} \times \vec{B} \right) \quad (2.7)$$

where the electric field \vec{E} has just been computed in step 2. and \vec{B} is given initially everywhere in the domain and is steady (Earth's magnetic field and tether induced magnetic field). This yields the equation of motion:

$$m \frac{d\vec{v}}{dt} = q \left(\vec{E} + \vec{v} \times \vec{B} \right) \quad (2.8)$$

which must be discretized to compute the new positions of the particle at the end of the

time step. Within a time step, even if the local electromagnetic field might vary, because of time/spatial variations of \vec{E} and spatial variations of \vec{B} , the fields are assumed to be frozen. For a planar problem, $\vec{B} = B\vec{e}_z$ and $E_z = 0$, which yields:

$$\frac{dv_x}{dt} = \frac{q}{m}(E_x + v_y \times B_z), \quad (2.9)$$

$$\frac{dv_y}{dt} = \frac{q}{m}(E_y - v_x \times B_z), \quad (2.10)$$

which may be conveniently written:

$$\frac{d\underline{v}}{dt} = \frac{q}{m} [\underline{E} - \imath B_z \underline{v}], \quad (2.11)$$

where $\underline{E} = E_x + \imath E_y$ and $\underline{v} = v_x + \imath v_y$, yielding simply, for $B_z \neq 0$:

$$\underline{v} = \underline{v}(t=0) \exp[-\imath \omega_c t] - \imath \frac{\underline{E}}{B_z}, \quad (2.12)$$

or:

$$v_x = \frac{E_y}{B_z} + v_x(t=0) \cos(\omega_c t) - v_y(t=0) \sin(\omega_c t) \quad (2.13)$$

$$v_y = -\frac{E_x}{B_z} - v_x(t=0) \sin(\omega_c t) + v_y(t=0) \cos(\omega_c t) \quad (2.14)$$

The following numerical scheme has been chosen:

1. • $v_x^{n+\frac{1}{3}} = v_x^n + \frac{q}{m} E_x(x^n, y^n) \frac{dt}{2}$ and $v_y^{n+\frac{1}{3}} = v_y^n + \frac{q}{m} E_y(x^n, y^n) \frac{dt}{2}$, acceleration by the electric field during the first half of the time step.
- $v_{xL}^{n+\frac{2}{3}} = v_{xL}^{n+\frac{1}{3}} \cos(\omega_c \times dt) - v_{yL}^{n+\frac{1}{3}} \sin(\omega_c \times dt)$ and $v_{yL}^{n+\frac{2}{3}} = v_{yL}^{n+\frac{1}{3}} \cos(\omega_c \times dt) + v_{xL}^{n+\frac{1}{3}} \sin(\omega_c \times dt)$ with $\omega_c = \frac{qB_{zL}}{m}$, and $(\vec{x}_L, \vec{y}_L, \vec{z}_L)$ is a direct orthonormal basis defined by $\vec{B} = B_{zL} \vec{z}_L$, which is not in the z direction in the general (and most interesting) cases. This motion corresponds to the cyclotron rotation of the velocity vector due to the magnetic field through the time step and implies a change of basis from $(\vec{x}, \vec{y}, \vec{z})$ to $(\vec{x}_L, \vec{y}_L, \vec{z}_L)$.

- $v_x^{n+1} = v_x^{n+\frac{2}{3}} + \frac{q}{m} E_x(x^n, y^n) \frac{dt}{2}$ and $v_y^{n+1} = v_y^{n+\frac{2}{3}} + \frac{q}{m} E_y(x^n, y^n) \frac{dt}{2}$, acceleration by the electric field during the second half of the time step.

yielding:

$$\begin{aligned}
[v_x + v_y]^{n+1} &= \frac{q}{m} [E_x + iE_y] \frac{dt}{2} + \left[\begin{aligned} &\left(v_x^n + \frac{q}{m} E_x \frac{dt}{2} \right) \cos(\omega_c \times dt) \\ &- \left(v_y^n + \frac{q}{m} E_y \frac{dt}{2} \right) \sin(\omega_c \times dt) \end{aligned} \right] \\
&+ i \left(v_y^n + \frac{q}{m} E_y \frac{dt}{2} \right) \cos(\omega_c \times dt) + \left(v_x^n + \frac{q}{m} E_x \frac{dt}{2} \right) \sin(\omega_c \times dt)
\end{aligned} \quad (2.15)$$

or:

$$\underline{v}^{n+1} = \frac{q}{m} \frac{dt}{2} \underline{E} + \left(\underline{v}^n + \frac{q}{m} \frac{dt}{2} \underline{E} \right) \exp[i\omega_c dt]. \quad (2.17)$$

And finally, the new position is computed from:

$$x^{n+1} = x^n + v_x^{n+1} dt \quad (2.18)$$

$$y^{n+1} = y^n + v_y^{n+1} dt. \quad (2.19)$$

Unlike standard leapfrog methods, this scheme allows to compute accurately trajectories in magnetic field, thanks to the analytical rotation of the velocity. It has been extended to a 3V version.

2.2.5 Injectors: open, non neutral domain

The global neutrality of the domain is not artificially maintained in the code, as is often the case, for the two injector regions only simulate the background plasma infinitely far from the tether but no other source/sink has been built in order to maintain exact neutrality. The two injectors must be wide enough such that right at their boundary with the physical domain, the kinetic distribution is already as expected. Imagine for instance a line injector on the left of the domain. At the end of the particle motion (step 3), no particles very near the boundary would have a large v_x , for such particles necessarily come from the left injectors and then leave very quickly (within the first time step) the domain boundary. With an injector, which

width is at least $v_x^{\max} dt$, where v_x^{\max} is the velocity of the fastest particles, even the particles with the highest v_x can be found near the boundary, coming from the left part of the injector. This technique allows to get everywhere in the domain the kinetic distribution which has been chosen, without operating a spatial separation between slow and fast particles.

Note that this injection method provides fixed fluxes into the domain, without any warranty that the total charge is conserved. In order to compensate for the particle sink due to the capturing probe, we then had to refine this rough boundary conditions, as explained later on.

2.2.6 Kinetic modeling

In order to simulate the overall tether-ionosphere system, ions and electrons must be created everywhere in the domain initially and then injected into the domain when required. Without the probe, the background plasma should be perfectly Maxwellized by Coulomb collisions in the ionosphere. However, such collisional Maxwellization takes place on a very large spatial scale (several km), for the mean free path of Coulomb collisions is of the order of 1km, which makes it impossible to model in our PIC simulations. When the probe is introduced in the plasma, this Maxwellian distribution should not be disturbed far from it. In a given cell, the plasma is always created according to a discretized Maxwellian distribution. Therefore, at the start of the simulation, when the probe is turned on, we must artificially create a background Maxwellian plasma everywhere. Moreover, at the domain boundaries, which are supposed to lie far enough from the probe such that the perturbations due to the probe are there negligible, the plasma must remain Maxwellian at any time.

Because of the finite number of particles per cell, it is actually impossible to create locally a perfectly continuous Maxwellian plasma. A given range of velocities is chosen, of the order of the thermal velocity. The macroparticle velocities in each cell are uniformly distributed in this range, but the weight of each macroparticle, proportional to the number of actual particle it contains, is calculated in order to get a discretized Maxwellian distribution: the more energetic a particle is, the lower its weight. The same values for the macroparticle velocities are taken in every cell. Therefore, if $n_{part/cell} = 2n_{p/c}^x \times 2n_{p/c}^y$ is the number of macroparticles per cell, $n_{part/cell}$ monoenergetic beams, with various weights, are created for each particle throughout the creation zone. Keeping the same particle velocities in each cell when creating particles

allows us to have initially a perfectly uniform density throughout the creation zone. This kinetic discretization is called "quiet start", for it begins without any density and field fluctuations in the whole domain.

The symmetric uniformly distributed range of velocities is:

$$\left[-\alpha v_{th}, -\frac{n_{p/c}^x - 1}{n_{p/c}^x} \alpha v_{th}, \dots, -\frac{1}{n_{p/c}^x} \alpha v_{th}, \frac{1}{n_{p/c}^x} \alpha v_{th}, \dots, \frac{n_{p/c}^x - 1}{n_{p/c}^x} \alpha v_{th}, \alpha v_{th} \right] \text{ in the } v_x \text{ direction and:}$$

$\left[-\alpha v_{th}, -\frac{n_{p/c}^y - 1}{n_{p/c}^y} \alpha v_{th}, \dots, -\frac{1}{n_{p/c}^y} \alpha v_{th}, \frac{1}{n_{p/c}^y} \alpha v_{th}, \dots, \frac{n_{p/c}^y - 1}{n_{p/c}^y} \alpha v_{th}, \alpha v_{th} \right]$ in the v_y direction, which gives $2n_{p/c}^x \times 2n_{p/c}^y$ (v_x, v_y) velocity vectors attributed to $n_{part/cell} = 2n_{p/c}^x \times 2n_{p/c}^y$ particles. As mentioned later on, we used $\alpha = 2$ or $\alpha = 3$.

The weight of each macro-particle, attributed when the particle is created, is defined as:

$$w_k = \frac{n_\infty}{\pi \times 2v_{tk}^2} \exp \frac{-(v_x^2 + v_y^2)}{2v_{tk}^2}, \quad (2.20)$$

with $v_{tk}^2 = \frac{T_k}{m_k}$, for a 2V distribution. It is related to the density by:

$$\sum_{k=macro-e^-/macro-ions} w_k dv_x dv_y \simeq \iint \frac{n_\infty}{\pi \times 2v_{tk}^2} \exp \frac{-(v_x^2 + v_y^2)}{2v_{tk}^2} dv_x dv_y = n_\infty. \quad (2.21)$$

This discrete model of a Maxwellian plasma is schematically represented in velocity space in Figure 3-1 (next Chapter).

We show in the Chapter "Current collection: benchmarking with symmetric cases" that local density and field fluctuations allow to get a continuous time-averaged Maxwellian distribution from the original discretized Maxwellian.

2.2.7 Particle capture by a probe

Once the particle trajectory has been computed within the time step, defined by a straight segment, a function determines if this segment intersects the tether boundary, which is defined analytically, as a circle in our case. If it this is the case, the weighted charge of the particle is

taken into account towards the current collected by the probe. The weight of the particle is set to zero and the destruction of the particle follows.

An accurate computation of trajectories near the tether is required to simulate the capture and thus compute the collected current. For this purpose:

- the fields must be finely computed on the mesh, which implies a minimum refinement of the mesh near the probe or the implementation of analytical fields near the probe.
- the distance made by a particle within a time step must not be too long, such that the segment approximates well enough the exact trajectory. For this purpose, the time step is progressively reduced when a particle gets nearer from the probe, where the accelerations are much higher.

2.2.8 Boundary Conditions

An original feature of our code is the choice of periodic boundary conditions in the y direction. The periodicity holds for the particle trajectories. Indeed, a particle leaving the domain through $\{y = y_{\min}\}$ is re-injected into the domain through $\{y = y_{\max}\}$ (cf. Figure 2-3), with the same velocity, and vice-versa. Such a BC allows to simulate infinite periodic arrays of tether and induces a very good mixing along y . For instance, as shown in Figure 3-4, the electron v_y distribution gets almost perfectly Maxwellian in the domain after a few hundred time steps.

At the left and right boundaries of the domain, the Poisson solver allows to choose either Neumann: $\Phi = \Phi_{\text{boundary}} = 0$, either Dirichlet: $\vec{E} = \vec{E}_{\text{boundary}} = \vec{0}$.

2.2.9 Orbital velocity

Taking into account the orbital velocity of the satellite where the tether is assumed to be affixed is not exactly equivalent to a plasma flow on a steady probe, which only implies to add \vec{V}_{flow} to all velocities. Due to the change from terrestrial frame to a drifting frame, moving with the satellite, a uniform "motional" electric field must be indeed added to the electric field due to the probe bias and the plasma charge density:

$$\vec{E} = \vec{E}_{PoissonSolver} + \vec{E}_m; \quad (2.22)$$

$$\vec{E}_m = \vec{V}_{orb} \times \vec{B} \quad (2.23)$$

This motional electric field typically results in induced bias around $0.2V/m$. Since $T_e = 0.1eV$ in the ionosphere, a typical orbiting tether actually sustains a significant non-uniformity in bias. However, in the typical $\vec{V}_{orb} \perp \vec{B}$ configuration, \vec{E}_m points along the tether and thus does not influence the dynamics in the (x, y) plane.

2.2.10 Non-dimensional parameters

In the code, most equations are non-dimensional, using the following ratios:

$$\text{distance} : \frac{r}{\lambda_{De}} \quad (2.24)$$

$$\text{time} : \frac{t}{\omega_{pe}^{-1}} \quad (2.25)$$

$$\text{velocity} : \frac{v}{v_{te_0}} \quad (2.26)$$

$$\text{potential} : \frac{\Phi}{T_{e_0}}, \quad (2.27)$$

which is consistent, since the thermal velocity in the background plasma v_{te_0} can be written as well :

$$v_{te_0} = \frac{\lambda_{De}}{\omega_{pe}^{-1}} \quad (2.28)$$

2.3 Tether bias modelling: Fast Poisson Solver benchmarking

2.3.1 Tether modeled by a fixed potential at a mesh node

The mesh we first used is uniform, which is much simpler for a Fast Poisson Solver. The electric field and potential are computed on each node of the mesh, that is why the simplest

idea to model a thin tether was to impose a fixed potential at a node. This would model an infinitely thin tether. Figure ?? shows that the discretization method on the mesh produces a non monotonic radial electric field. The electric field *computed by the Poisson Solver*, which is zero by symmetry at the tether position (whereas it theoretically diverges for an infinitely thin tether), increases up to the nearest nodes surrounding the tether and then decreases. If we assume the tether radius equals the size of one square cell of the mesh, this model could be a simple way to compute the electric field generated by a cylindrical wire at a fixed potential. To evaluate the validity of this simplified boundary condition for the tether section, we studied the electrostatic field produced in vacuum. Taking the particle charges $q_e = q_i = 0$, we obtained the electrostatic potential and field directly after one iteration. If the influence of the y periodic boundary condition is neglected, which is considered fair enough for a large enough domain in the y direction, an analytical solution is available: In vacuum, the potential satisfies Laplace equation (8.1), namely here:

$$r \frac{\partial \Phi}{\partial r} = cst, \quad (2.29)$$

with the approximate radial boundary conditions:

$$\Phi(R_\infty) = 0 \text{ and } \Phi(R) = \Phi_p. \quad (2.30)$$

The actual boundary conditions on the x boundaries can be approximated by these radial conditions if the domain is large enough: say with R_∞ the distance between the tether and the left/right boundary. Then, the potential can be written:

$$\Phi(r) = \Phi_p \frac{\ln(R_\infty) - \ln(r)}{\ln(R_\infty) - \ln(R)}, \quad (2.31)$$

and the electric field:

$$E(r) = -\frac{\Phi_p}{r \ln(R_\infty/R)}. \quad (2.32)$$

Let us note that assuming a vanishing electric field at the boundary instead of a vanishing potential would not be a proper definition of the Laplace problem. $\Phi_p = 0$ would be then

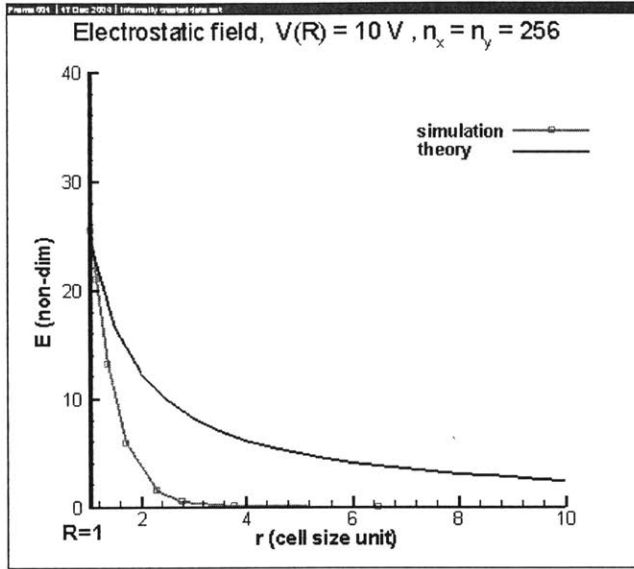


Figure 2-5:

required by Equation 2.32. Figures (2-5),(2-6) and (2-7) show the simulated field and potential for a large mesh size (256×256). The global behavior of the fields turns out to depend on the mesh size. Surprisingly, increasing the mesh size does not yield a better global behavior of the electric field and potential. Instead of having the electric field decreasing like $\frac{1}{r}$, it decreases like $\exp(-r/r_0)$ when the mesh is large enough. As a consequence, the modeling of the thin wire by a node at fixed potential turns out to be invalid. If we only consider electrostatic effects, a small wire where a current flows can be seen as an infinitely small line charge. In this case, the potential is supposed to diverge when r vanishes. Thus, our finite potential boundary condition at a node does not correspond to this limit case. Defining the tether as a singular potential perturbation is not equivalent to the line charge problem, which explains why our Poisson solver returns absurd results.

Two main ideas arise then to improve the modeling of the probe:

- tether section modeling by several adjacent nodes where the potential is fixed;
- infinitely thin tether modeled by a fixed point charge.

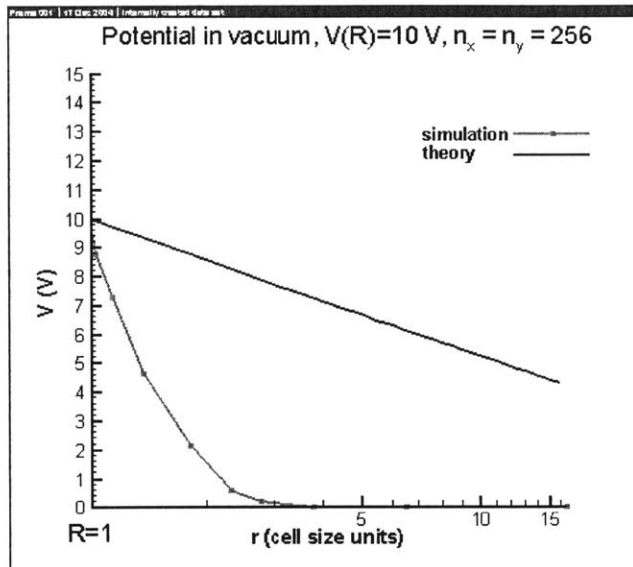


Figure 2-6:

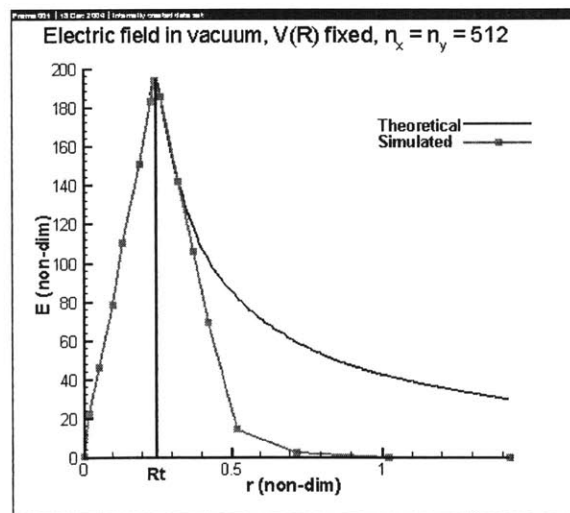


Figure 2-7: A zoom in the tether region for a very fine grid: the fixed potential condition at a point fails to simulate a tether in vacuum, even close to the probe.

In the first case, we would need at least four nodes to obtain through the extrapolation a non zero area at fixed potential, which would then be equivalent to a fixed charge problem, through the Gauss theorem. A first version of the code allowed us to impose a fixed potential at two nodes (which is not enough to get an area at fixed potential). The simulated field still did not behave properly, even in the direction of the two aligned nodes. Later versions allowed us to fix the potential at an arbitrary number of nodes. Because our mesh is uniform, some concerns remain with this method to model the wire section, to allow proper Fast Poisson solving. Indeed, if we want to model a very thin wire (up to $r \sim 0.1\lambda_{De}$), this method requires a very large mesh (512×512 cells at least) to simulate a large enough domain. The increase in computational time, and above all RAM memory required does not seem to be affordable yet on a personal computer.

2.3.2 Tether modeled by a point charge at a mesh node

As required, we changed the modelling of the tether. Instead of imposing a given potential at a node in the Poisson Solver, we modelled it as a line charge: a given fixed charge was attributed to a node representing the center of the tether cross section. Figures 2-8,2-9,2-10,2-11 show the computed potential and fields in vacuum around such a line charge. Except for local spatial and temporal fluctuations, mainly far (dozens of Debye lengths) from the tether, which also occur in a real finite temperature plasma like the ionosphere, these tests agreed with analytical results.

There is one noticeable constraint of our Poisson solver that showed up clearly in the benchmarking simulations. Figures 2-12 and 2-13, where the electric field is represented in a few cells around the tether, show that the electric field is linearly increasing from $r = 0$ to $r = \delta r$, where δr is the size of a square cell.

These variations do not correspond to the theoretical electric field, which is found from Gauss theorem around a point charge with boundary conditions $V(\infty) = 0$ (cgs units):

$$E(r) = 2q\frac{1}{r}, \quad (2.33)$$

$$\Phi(r) = \Phi(R) - 2q\ln\left(\frac{r}{R}\right), \forall r > 0. \quad (2.34)$$

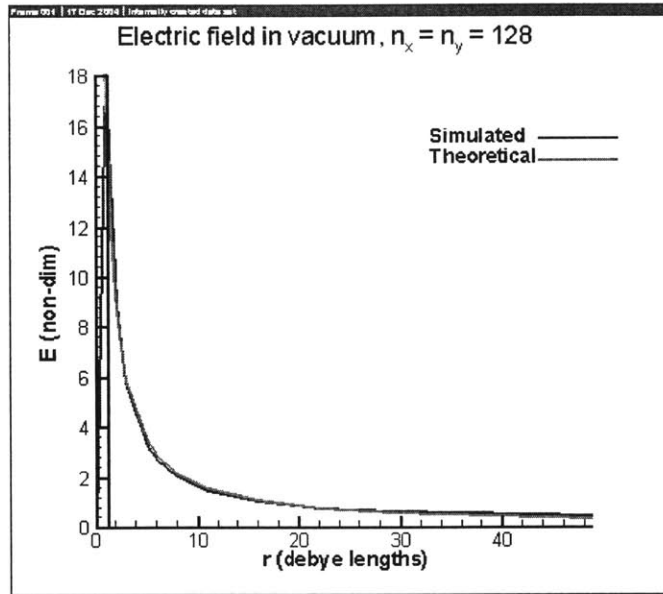


Figure 2-8:

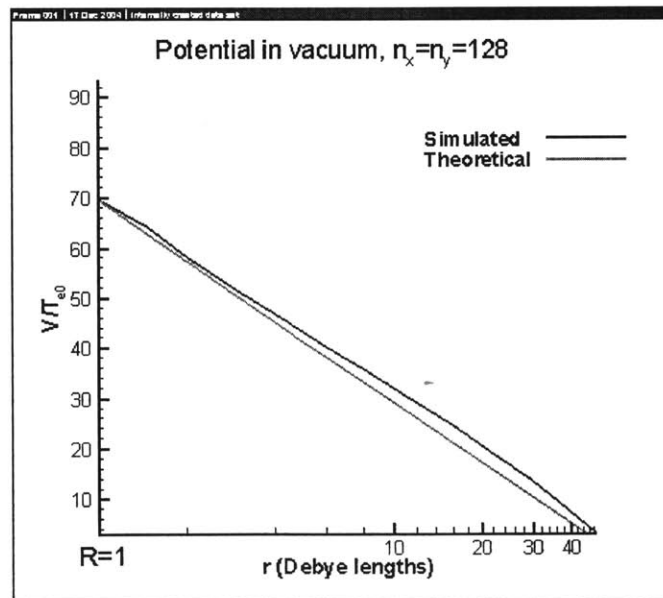


Figure 2-9:

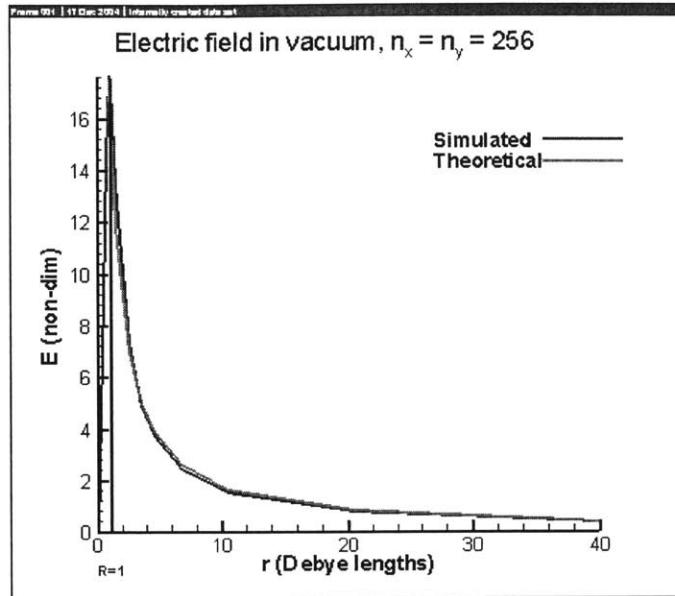


Figure 2-10:

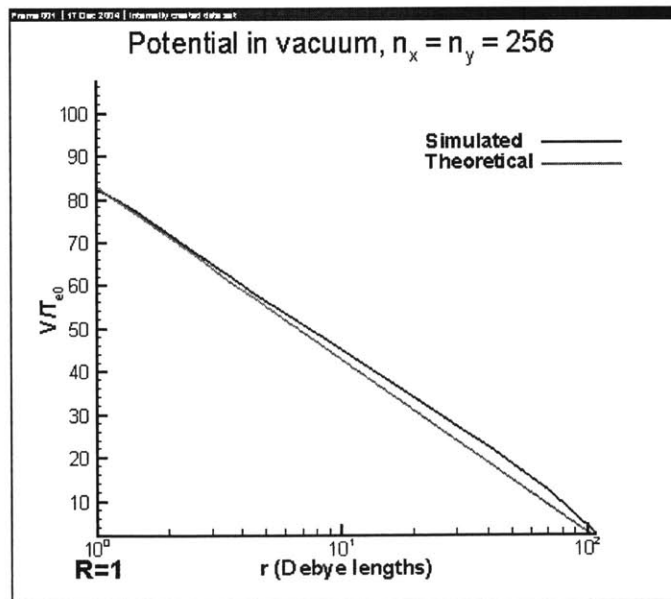


Figure 2-11: In all the above plots, a fixed charge has been put at the center of the tether and the tether surface is located at $R=1$.

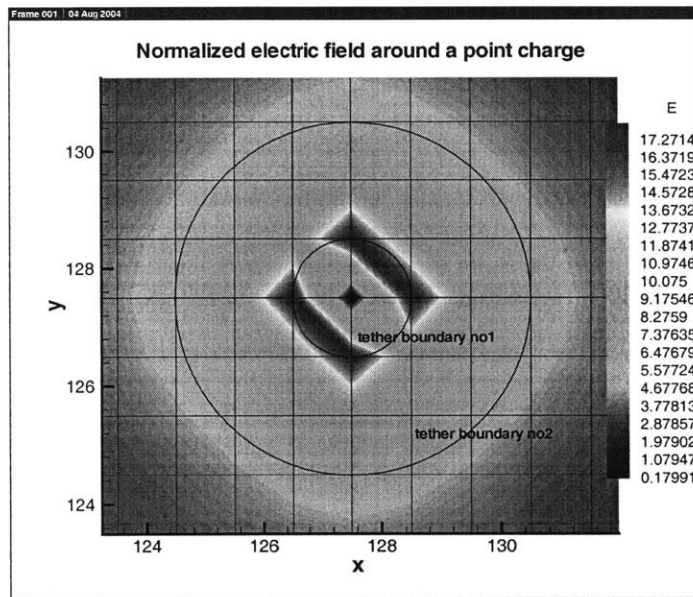


Figure 2-12: The apparent extreme asymmetry is only due to the plotter. Nonetheless, the E-level can be approximated by circles only far enough from the charge: the anisotropy might be too strong if the tether surface is set at position n^o1 , whereas it is negligible at position n^o2 .

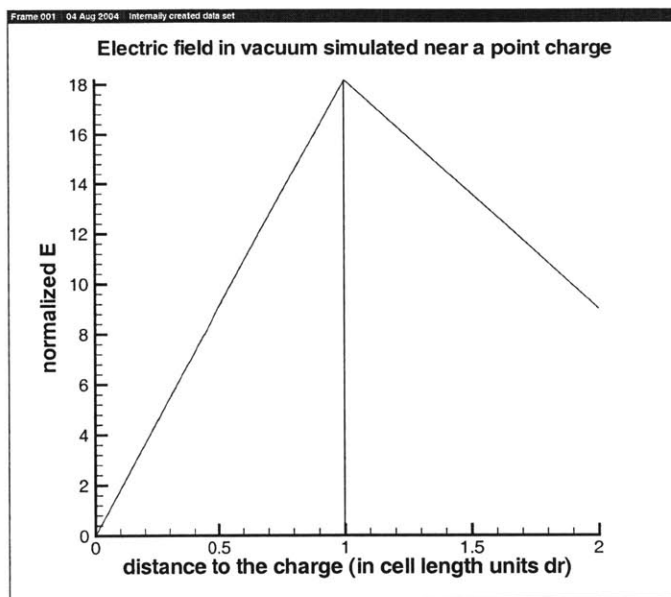


Figure 2-13: Even with a decreasing potential, the corresponding electric field increases linearly up to $r = dr$ (one cell) and then decreases. Thus, the analytical tether boundary can't be set nearer than a distance dr from the charge.

Nonetheless, for a homogeneous charge in a disk of radius R , the Gauss' theorem yields:

$$E(r) = \frac{2q}{R^2}r, \quad (2.35)$$

$$\Phi(r) = \Phi(R) - q \left(\frac{r^2}{R^2} - 1 \right), \forall r \leq R \quad (2.36)$$

and

$$E(r) = 2q \frac{1}{r}, \quad (2.37)$$

$$\Phi(r) = \Phi(R) - 2q \ln \left(\frac{r}{R} \right), \forall r \geq R \quad (2.38)$$

Given a domain boundary, say at $r = R_\infty$ to keep the axisymmetry, where the Dirichlet boundary holds: $\Phi(R_\infty) = 0$. We can find now the line charge q , which yields a specified potential $\Phi(R) = \Phi_p$ at the probe surface:

$$q = \frac{\Phi_p}{2 \ln \frac{R_\infty}{R}}. \quad (2.39)$$

Typically, we shall take R_∞ equal to the distance between the tether and the left/right boundary of the domain, where the Dirichlet condition holds. Note that the dependence of q on R_∞ is not negligible, so it seems more appropriate to evaluate from the code what Φ_p is associated with each choice of q . With this choice of q , the field and potential can be rewritten as a function of R_∞ and Φ_p :

$$E(r) = \frac{\Phi_p}{\ln \frac{R_\infty}{R}} \frac{r}{R^2}, \quad (2.40)$$

$$\Phi(r) = \Phi_p \left[1 - \frac{\frac{r^2}{R^2} - 1}{2 \ln \frac{R_\infty}{R}} \right], \forall r \leq R \quad (2.41)$$

and:

$$E(r) = \frac{\Phi_p}{\ln \frac{R_\infty}{R}} \frac{1}{r}, \quad (2.42)$$

$$\Phi(r) = \Phi_p \frac{\ln \frac{R_\infty}{r}}{\ln \frac{R_\infty}{R}}, \forall r \geq R \quad (2.43)$$

Thus, the electric field computed in the four cells around the tether corresponds to the field produced by a homogeneous charge in the disk $\{r \leq \delta r\}$, whereas the potential corresponds to a singular point charge at $r = 0$. Therefore, we shall not take into account the computed electric field and potential inside this disk. When we model the tether by a point charge at $r = 0$, we must actually consider that the tether cross section is wider than the disk $\{r \leq \delta r\}$. Figure 2-12 shows that the electric field is strongly anisotropic (by 30%) in the few cells around the charge, due to the anisotropy of our coarse uniform rectangular mesh around a point charge and the interpolation method. It turns out that \vec{E} level curves can't be approximated by circles at $r \lesssim 3\delta r$. As mentioned above, outside the tether boundary $\{r = k \times \delta r\}$, the Fast Poisson Solver yields excellent results, if $k \gtrsim 3$. We have investigated whether a better refinement is required to get accurate results for the collected current by comparing:

- computed particle trajectories near the tether with analytical solutions,
- the collected current computed by our code with analytical solutions and previous numerical results,

as presented in the next sections.

2.4 Multi-scale trajectory solver instead of analytical motion

A very standard way to compute accurate trajectories within a few Debye lengths from the tether is to:

- refine the mesh in a ring surrounding the tether (Figure 2-14).
- compute particle trajectories analytically in a smaller ring near the tether, where space charge effects are assumed to be negligible.

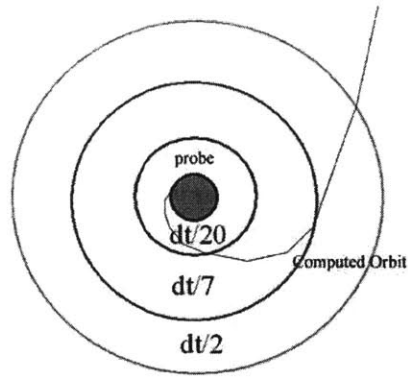


Figure 2-14: When a particle gets closer to the tether, several sub-cycles (with frozen field) are used to calculate more accurately the trajectory in the vicinity of the tether, where velocities are much higher.

Both were done by [1]Onishi, 2002 in order to avoid the effects both the Poisson and motion solvers inaccuracies when potential gradients get very high, as it is the case in the sheath around the tether. Such local refinements were possible with a standard Poisson solver, which allows adaptive meshes with several singularities. A Fast Poisson Solver, however, only allows meshes obtained through conformal mapping of a uniform $2^n \times 2^n$ mesh. Therefore, for the sake of simplicity, we checked if our uniform grid could be accurate enough to compute particle trajectories in the neighborhood of the tether, before attempting any refinement or analytical motion solving.

The benchmarking of our Fast Poisson Solver (Figures 2-8,??,2-9,2-11) seemed to indicate that the electric field was computed accurately up to a few percent even near the tether, which would indicate that even a uniform mesh with a cell size as big as the tether itself was sufficient to yield accurately the electric field everywhere through extrapolation. Because the computation of the collected current is directly depending on the fine shape of the electron trajectories very near the tether, the ultimate way to validate our model is to compare computed trajectories with analytical or accurate numerical solutions in the sheath surrounding the tether.

We decided to validate this part of our code, by comparing simulated trajectories of particles near a line charge q_t in vacuum with orbits calculated by a numerical solver of dynamic systems. This case corresponds to the motion of a particle in the non-magnetized sheath, when space

charge effects are neglected and therefore the Poisson equation simplifies into the simple Laplace equation.

The equations of motion then are written:

$$\frac{dv_x}{dt} = \frac{q}{m} E_x, \quad (2.44)$$

$$\frac{dv_y}{dt} = \frac{q}{m} E_y, \quad (2.45)$$

where q and m are the particle charge and mass respectively. \vec{E} is found easily from Gauss theorem (in *cgs* units), which yields eventually the following dynamic system:

$$\frac{dv_x}{dt} = \frac{2q}{m} \frac{qt}{x^2 + y^2} x, \quad (2.46)$$

$$\frac{dv_y}{dt} = \frac{2q}{m} \frac{qt}{x^2 + y^2} y. \quad (2.47)$$

Only the initial conditions x_0 , y_0 , v_{x0} and v_{y0} then have to be chosen. Numerical solutions with arbitrary accuracy were computed with Dynamics Solver (Figures (2-15) and (2-17)) and compared to a marked particle trajectory from the code (Figures (2-16) and (2-18)), where the electric field was computed by our Fast Poisson Solver on a uniform grid and the time step reduced when approaching the tether (cf. Figure 2-14). If the time step is small enough, trajectories fit up to a few percent even very near the tether. This means that the uniform mesh where the electric field is computed by our Fast Poisson Solver does not have to be refined near the tether and that analytical motion solving is not required in the sheath surrounding the tether. Note that we chose here a tether radius equal to δr , which still produces some anisotropies of the electric field very near the tether (up to $r \simeq 3\delta r$) as mentioned above. Nonetheless, these anisotropies do not seem to affect much trajectories, even when they pass in the region $\{r \leq 3\delta r\}$ (Figures 2-17 and 2-18).

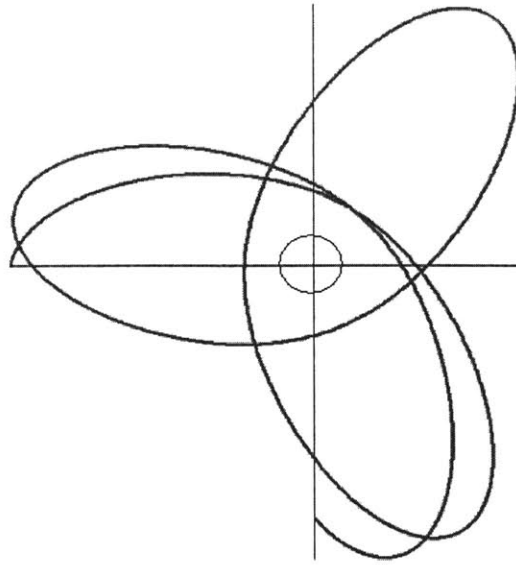


Figure 2-15: orbit in vacuum around a $10^9 e/\text{unit length}$ line charge, given by a numerical solver

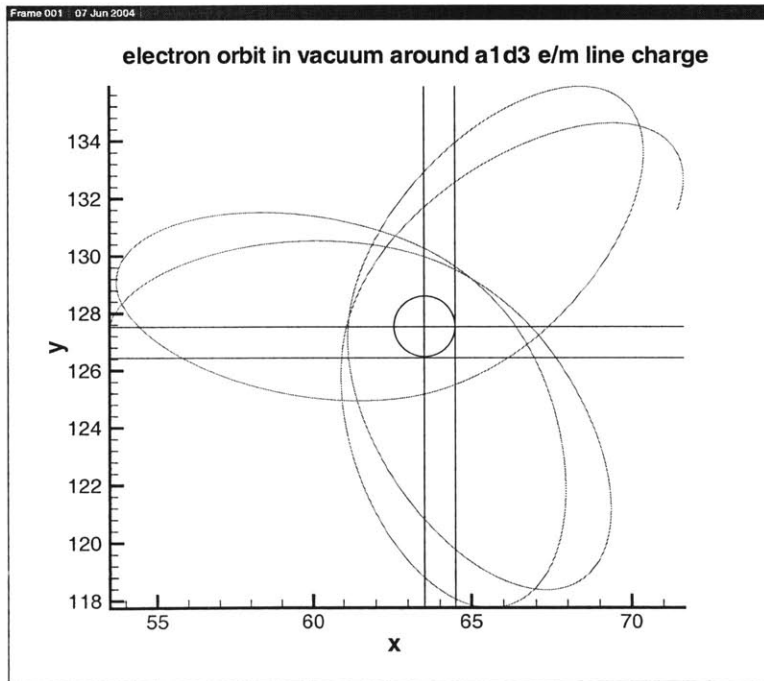


Figure 2-16: orbit in vacuum around a $10^3 e/\text{unit length}$ from the PIC simulation

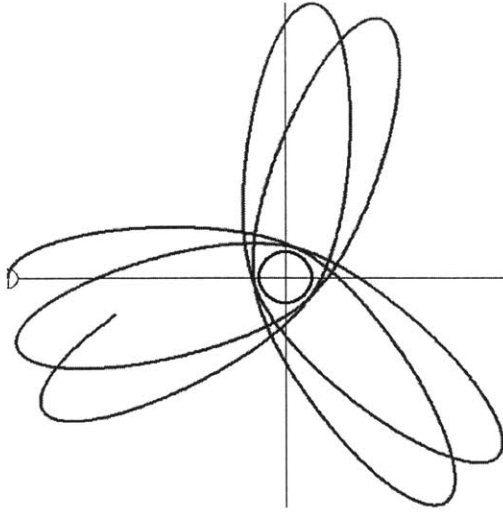


Figure 2-17: orbit in vacuum around a $10^9 e/\text{unit length}$ line charge, given by a numerical solver

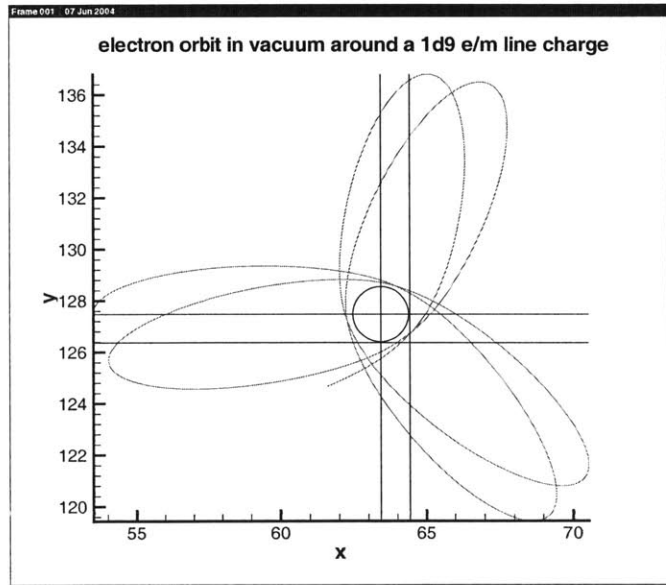


Figure 2-18: orbit in vacuum around a $10^9 e/\text{unit length}$ from the PIC simulation

In the close vicinity of the tether, the particle acceleration is very high, especially for electrons. Therefore, the maximum electron kinetic energy, which is reached on Figures 2-16,2-18 at the closest point to the tether is approximately given by the tether potential. The maximum time step required to compute accurate trajectories can be considered as inversely proportional to the maximum electron velocity, and thus inversely proportional to the square root of the tether potential:

$$dt_{\max} \propto \frac{1}{v_{e \max}} \propto \frac{1}{\sqrt{\chi_p}}, \quad (2.48)$$

where $\chi_p = \frac{e\Phi_p}{kT_{e0}}$.

We checked with several values of the tether potential (or line charge), that:

$$dt = 10^{-2} \sqrt{\frac{10^4}{\chi_p}} \omega_{pe}^{-1}, \quad (2.49)$$

always allowed to compute accurate trajectories in vacuum for any tether potential Φ_p . ω_{pe} is the electron plasma frequency, which is used to normalized the times in the code (when there is no plasma, it is calculated from the typical ionospheric density $n_0 = 10^5 \text{ cm}^{-3}$). For the most stringent high tether potentials, like $\chi_p = 1000$, this yields an upper value for the time step near the tether: $dt_{\max}^{\text{near}} = 3 \times 10^{-2} \omega_{pe}^{-1}$.

Therefore, we made sure to fulfill this requirement in all our simulations, such that all particle trajectories are computed accurately near the tether.

2.5 Plasma density control

The upstream/left and downstream/right injector boundaries provide the physical domain with a fixed neutral particle flux. Indeed, at every time steps, the same ion and electron beams are created and injected into the domain. In the right boundary, these beams correspond to the $v_x > 0$ part of the discretized Maxwellian distribution. In the left boundary, these beams correspond to the $v_x < 0$ part (cf. Figure 3-1). Since the density and the distribution shape are fixed in the boundaries, the incoming beams provide a fixed particle flux into the domain.

When there is no particle source/sink in the domain, only electric and density fluctuations occur in the domain. The plasma in the domain has the same distribution as the boundaries, except that it is partly continuous due to these fluctuations in the domain. Therefore, the beams provided by the boundaries compensate on the average the outgoing fluxes ($v_x < 0$ part of the partly continuous Maxwellian in the right and $v_x > 0$ in the left, with the same density as the boundaries). Indeed, both mean thermal velocity and density, which determine the thermal current, are constant throughout the domain and boundaries, except for local fluctuations. In this case, the quasi-neutrality everywhere in the domain is maintained.

Nonetheless, when particles are either created or destroyed inside the domain, as is the case when a particle is captured by the probe, the flux balance breaks down. If the injector flux is kept at the fixed level corresponding to the non-perturbed case, then the density in the domain will adjust to the sink/source effect and a different state is reached. In the positively attracting probe case, electrons are captured by the probe, and their density thus decreases progressively in the domain, for the incoming fluxes cannot balance the sink effect. While the electron density in the whole domain decreases (Figure 2-19), the electron flux into the probe and the outgoing electron fluxes (from the domain to the upstream/downstream boundaries), which vary in proportion with density, decrease as well. This temporary regime lasts until these outgoing and probe fluxes are low enough such that the incoming fluxes at the boundaries can balance them.

Our simulations with fixed incoming fluxes show indeed that a steady state is eventually reached, where the final density is of course smaller than the initial density, but still non-zero. For typical tether biases and reasonable domain sizes, this final density was significantly smaller than the initial density. So this sink-effect, due to the finite size of the domain, could not be neglected in our OML regime simulations. Some way of controlling the plasma density far from the probe had to be defined.

A criterion to verify that our plasma actually represents the space plasma at the density that is originally set in the simulation domain is to check that the actual plasma density "far enough" is still equal to the initially chosen density. "Far enough" means in our case: in two stripes of the physical domain, next to the boundaries and where we check that the perturbation created in the middle of the domain by the tether is completely shielded. The smoothness of

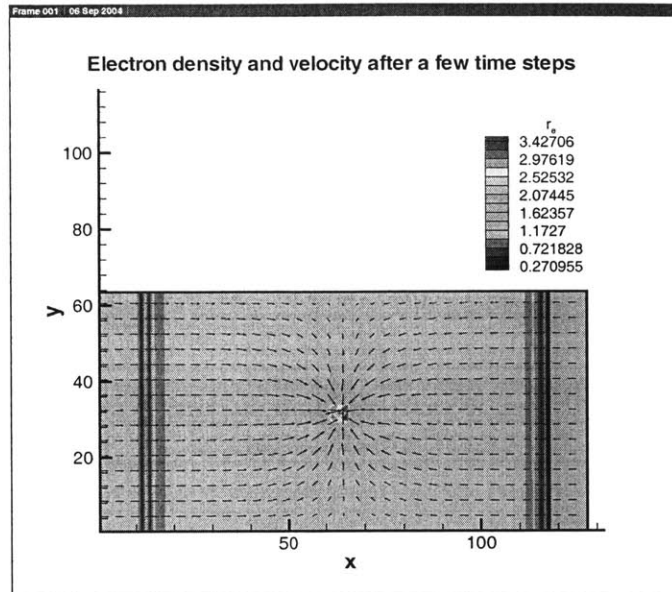


Figure 2-19: At the start of the simulation, the capturing biased probe acts an attractor for all electrons, inducing a density drop close to the boundaries. The arrows show the velocity field.

the particle densities, of the electric field and potential between these "stripes" and the vicinity of the tether have indeed to be checked to be sure that these density control stripes represent the background plasma.

Two different ways to modify these incoming fluxes from the boundaries in order to balance the capture by the probe were tested:

1. Feedback control

First, we made an attempt to implement a feedback control on the density. The density far from the probe was measured and compared to the expected value. Because of poor control laws, we did not get satisfactory results. These attempts are further explained in Appendix II, where a more proper way to define the control laws from the evaluated particle fluxes and densities is presented, in case this approach has to be implemented later on.

2. Fixed density by modifying macro-particle weights

At each time step, the density of each species is measured in each "density control stripe".

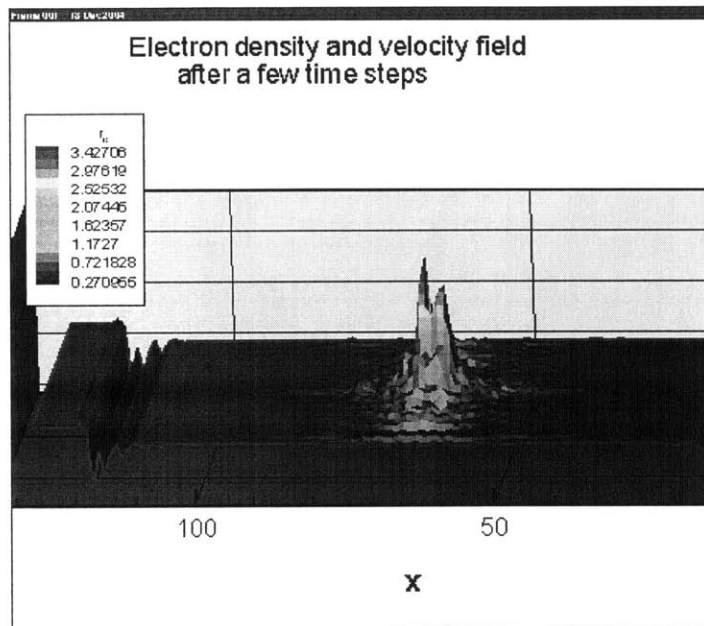


Figure 2-20: At the start, the probe acts suddenly as a particle sink, which makes the density drop everywhere in the domain. This drop is more obvious close to the boundaries, where electrons are suddenly accelerated towards the (still non-shielded) probe.

The weight of each particle is multiplied by the same amount, namely the ratio $\frac{n_{expected}}{n_{measured}} = \frac{n_0}{n_t}$, such that the density in the stripe is set to the expected density exactly at every time step.

This means that there is no mass conservation between the boundaries and these stripes. This method insures that we simulate a background plasma whose density is known and does not fluctuate globally, contrary to the feedback control method where the control density may fluctuate even at $t \rightarrow \infty$.

We have noticed in this case that some macro-particles could stay by chance for a very long time in the control stripes, and have their weight increased by a huge amount. Such particles become so important that they perturb a lot the local potential, creating shielding by the surrounding plasma, just like the fixed charge in the tether would do. In order to get smooth results, we had to get rid of these. A maximum allowed weight has thus been defined for electrons /ions, such that when a particle weight overtakes it, the corresponding particle is split into two smaller particles. We managed thus to avoid the creation of "super-heavy" particles. Figure 2-21 shows this simple process, which conserves exactly the kinetic momentum, and approximately the kinetic energy if the separation velocity between the two "sons" is small enough. We chose a separation velocity 0.1% of the thermal velocity, which induces only negligible non-conservative effects on the particle energy, given the fact that our PIC model is not energy conservative anyway.

The maximum particle weight first increases up to the set maximum allowed and is then maintained below this maximum level. Permanently increasing the number of particles by splitting them would slow down significantly the simulation and could eventually saturate the Page File Memory. But actually, in steady state, only a few particle splittings, negligible to the incoming and outgoing fluxes, are required per period in order to avoid the particle weights to become too high. As a consequence, the total number of particles stops growing quickly and naturally gets to a steady state which is still computationally affordable.

Figures 2-22 and 2-23 show the time evolution of density, actual maximum modified weights of particles and number of split particles per time step.

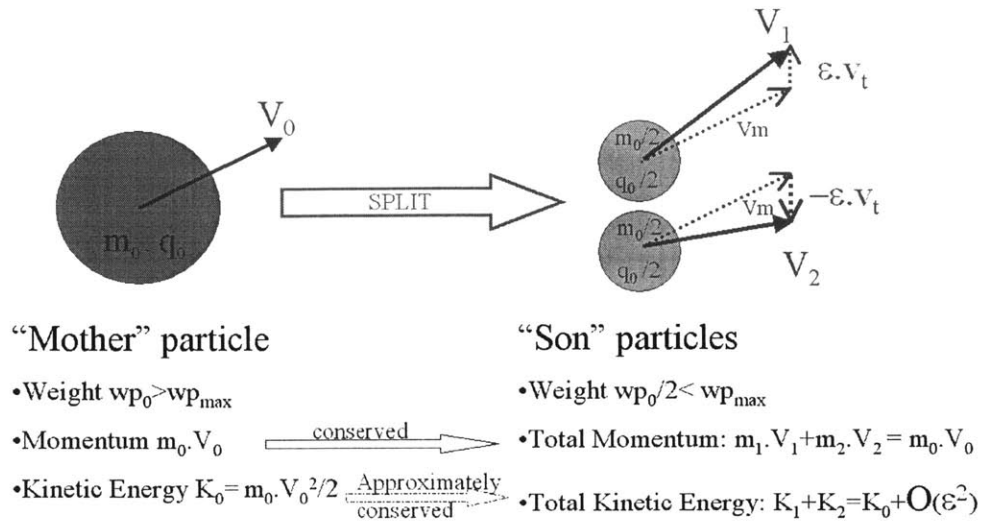


Figure 2-21: when the weight of particle becomes too high due to the "modify weights" method, it is split into two "son" particles, with slightly different velocities. The chosen process exactly conserves momentum, but only approximately the kinetic energy.

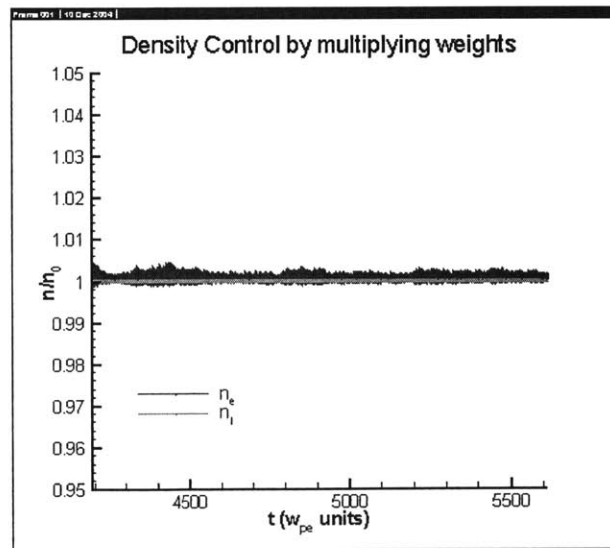


Figure 2-22: Adjusting the weights of particles close to the boundaries allows to fix the density at the expected background value n_0 for each species. This density control allows us to compensate the sink effect due to the absorbing probe.

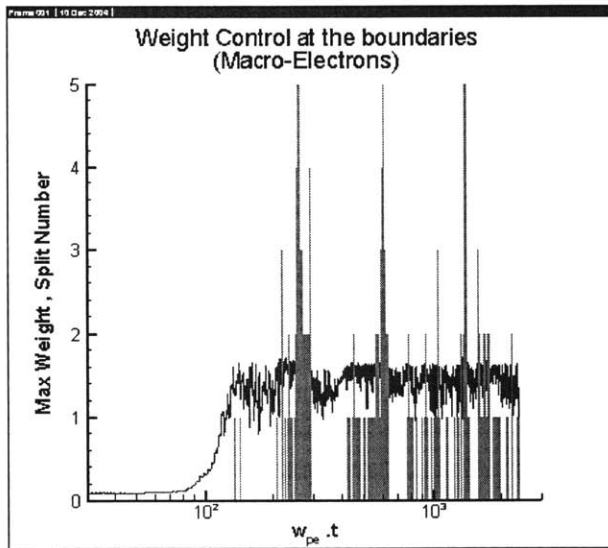


Figure 2-23: During a few hundred time steps, the incoming particle weights are increased to compensate the probe "sink effect" (red line). Then, when the weight of some particles, which have had a long stay in the control zone, becomes too high, such that it may perturb the ambient plasma, they are split into smaller ones. However, such splittings happen to very few particles at each time step (green bars).

2.6 Extension to 3V version

Tridimensional effects that could be relevant in the current collection. First, the tether is actually not an infinite straight wire but does have a finite length. At the end of the wire, electrons are emitted back to the ionosphere by a plasma contactor and make a loop in the ionosphere, back to some point of the tether. These effects should be negligible if the tether is extremely long, which is often the case (several hundreds of meters) and might be difficult to model, for we cannot handle a full 3D PIC simulation. Nonetheless, the particle motion along the tether direction z , should be taken into account, for the Earth's magnetic field, which is usually perpendicular to the wire, makes particles rotate across the $x - y$ plane. In order to handle the effects of the magnetic field B_x and B_y components on the current collection, particle motion along z must be allowed in our code, which could be done without increasing dramatically the computational time.

We used then a 3V Maxwellian distribution for velocities (Equation 1.1), which was discretized into 3V beams. Even if the particles are allowed to rotate perpendicularly to the $x - y$ plane through magnetic effects, they do not actually leave the plane and the simulation is still two-dimensional in position space.

The particle Larmor rotation is done by rotating the velocity vector according to the magnetic field value, and not by applying a leapfrog scheme, which does not conserve kinetic energy as it is the case for a particle in an homogeneous steady magnetic field.

Actual 3D trajectories, like helices, are restricted to their projection on the $x - y$ plane. Figures 2-24 and 2-25 show an helicoidal electron trajectory under a transverse magnetic field, in the position and velocity spaces.

Allowing the magnetic field to have a transverse component was necessary to study realistic and useful tether configurations. The boost or drag Lorentz force is indeed $I \cdot \vec{e}_z \times \vec{B}$ per unit length, which vanishes when \vec{B} is along \vec{e}_z . Moreover, this step was required to take into account the magnetic field created by the tether current, which is purely transverse to the tether.

2.7 Implementation of the self-induced magnetic field

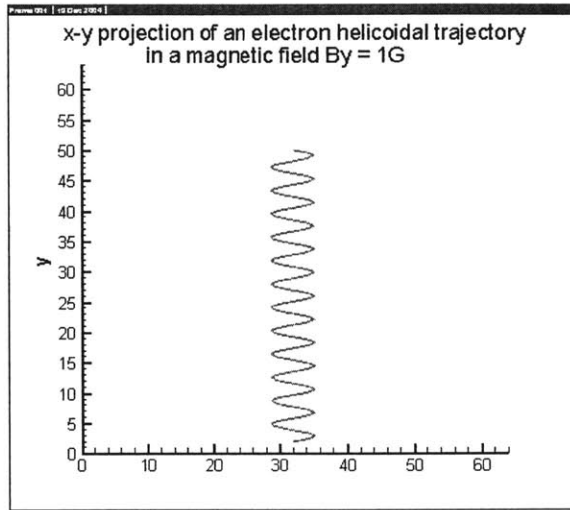


Figure 2-24:

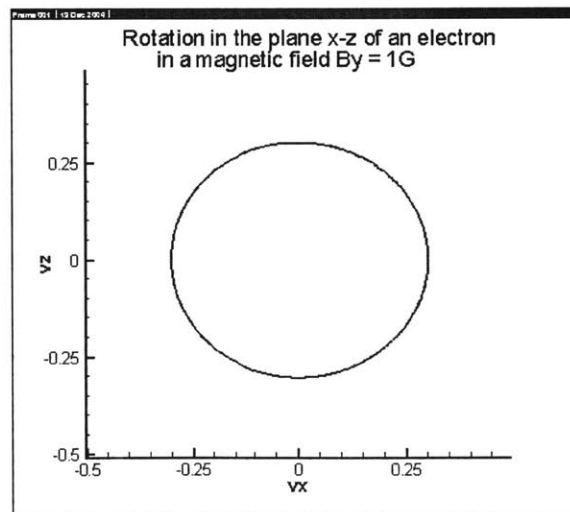


Figure 2-25:

As mentioned in Chapter "Theory of current collection by a probe in a plasma", the effects of the magnetic field induced by the tether current on the current collection could be relevant for ionospheric satellites. Very few authors have included in their computational work this self-field effect. Especially, all full PIC simulation of tether current collection were only able to support uniform magnetic field representing the Earth's magnetic field, but no space-dependent magnetic field.

We considered the tether current fixed by an external generator in the satellite, and thus implemented the self-induced field as an analytical function of the space coordinates, which can be added to an external uniform Earth's magnetic field.

The static magnetic field around a wire flown by a current I is merely given by Ampere's law in polar coordinates (r, θ) :

$$\vec{B}^s = B_\theta^s \vec{e}_\theta \quad (2.50)$$

$$\text{with } B_\theta^s = \frac{\mu_0 I}{2\pi r} \text{ (IS units),} \quad (2.51)$$

which we had to convert to Cartesian coordinates for the implementation:

$$B_x^s = -\frac{\mu_0 I}{2\pi r^2} [y - y_t], \quad (2.52)$$

$$B_y^s = \frac{\mu_0 I}{2\pi r^2} [x - x_t] \quad (2.53)$$

with (x_t, y_t) the wire position and $r = \sqrt{(x - x_t)^2 + (y - y_t)^2}$

In the previous calculation, we neglect the influence of local currents which may arise in the plasma, which means we actually use the analytical value of the magnetic field in vacuum.

A basic unit conversion yields the following form, as written in the code, where we use *cgs* units and a normalization by λ_{De} :

$$B_{\theta}^s(Gauss) = 0.2 \frac{I(A)}{r(\lambda_{De})\lambda_{De}(cm)}. \quad (2.54)$$

The total magnetic field is then:

$$\vec{B}(I, x, y) = \vec{B}^s(I, x, y) + \overrightarrow{B^{earth}}. \quad (2.55)$$

In Cartesian coordinates, all magnetic field lines $\xi(x, y) = cst$ are solutions of the partial differential equations:

$$\frac{\partial \xi}{\partial x} = B_y/B_0, \quad (2.56)$$

$$\frac{\partial \xi}{\partial y} = -B_x/B_0, \quad (2.57)$$

or, for $\overrightarrow{B^{earth}} = B_0 \vec{e}_y$:

$$\frac{\partial \xi}{\partial x} = 1 + \frac{\mu_0 I}{2\pi B_0 (x^2 + y^2)} [x - x_t], \quad (2.58)$$

$$\frac{\partial \xi}{\partial y} = \frac{\mu_0 I}{2\pi B_0 (x^2 + y^2)} [y - y_t], \quad (2.59)$$

which is straightforward to integrate:

$$\xi(x, y) = x - x_t + r^* \ln \frac{\sqrt{x^2 + y^2}}{r^*}, \quad (2.60)$$

with r^* given by formula (1.49).

This formula corresponds to the one given without details in [11]Khazanov et al. (2000) in cylindrical coordinates:

$$\xi = r^* \ln \left(\frac{r}{r^*} \right) + r \cos \alpha \cos \theta, \quad (2.61)$$

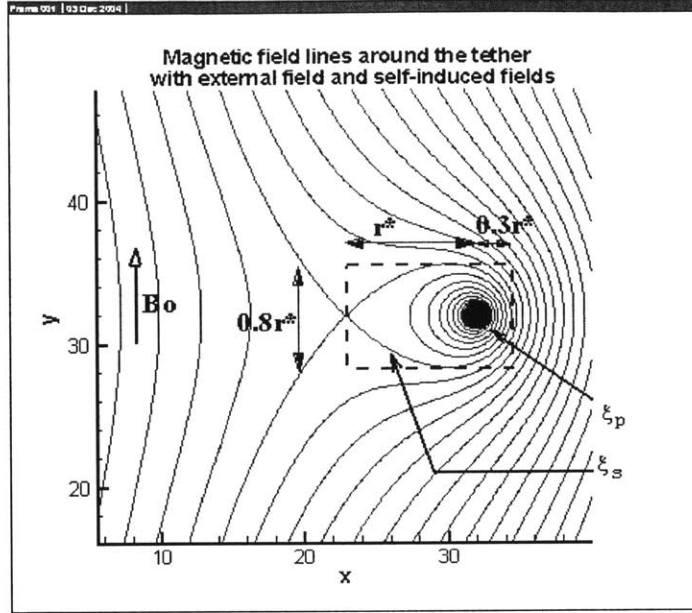


Figure 2-26: Magnetic field line topology near the tether, with the Earth's magnetic field B_0 along y and self-induced B_s . Distances are given in λ_{De} . The lines inside the separatrix are not connected to infinity and might thus trap electrons in the close vicinity of the probe. The dimensions of the separatrix are given with respect to r^* .

with $\alpha = 0$ in our case.

Figure 2-26 shows the field topology for $B_0 = 0.3G$ and $I = 10A$.

The characteristic size r^* of the separatrix defined by formula (1.49) reads numerically:

$$r^*/\lambda_{De} \simeq 0.2 \frac{I(A)}{\lambda_{De}(cm)B_0(G)}, \quad (2.62)$$

yielding in our reference case ($\lambda_{De} = 0.7cm$, $I = 10A$ and $B_0 = 0.3G$): $r^* \simeq 6.7cm$, or $\frac{r^*}{\lambda_{De}} \simeq 9$.

First, we studied the behavior of charged particles in such a field map. Figures 2-30 to 2-33 show various possible trajectories for an electron subjected to this field topology in vacuum (non-zero bias and magnetic fields, but no surrounding plasma). Figure 2-30 shows that the effective Larmor radius gets smaller close to the tether, where the induced field is high. There

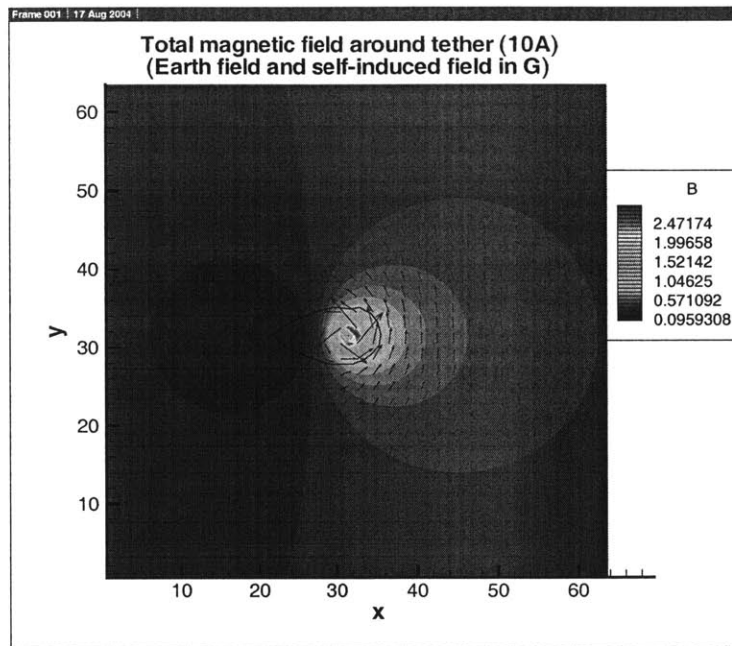


Figure 2-27: Magnetic field map, with the self-induced field. The background is the magnetic field intensity. Closed magnetic lines are created inside a magnetic envelope, which is drawn here around the tether

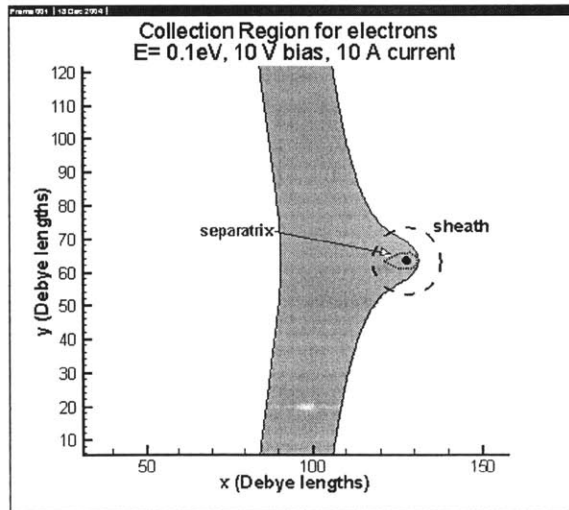


Figure 2-28:

(inside the separatrix), particles tend to be more bound to the magnetic lines, and can get trapped for a very long time in it, as shown by Figure 2-33. When the probe bias is low (Figure 2-32: 3V), electrons cannot cross the magnetic lines in order to get to the separatrix: the collection area is very thin (cf. Figure 2-28). When the tether bias is high enough, electrons can cross the magnetic lines and reach the probe, as illustrated by Figure 2-31, which shows an actual captured trajectory, for a 45 V bias.

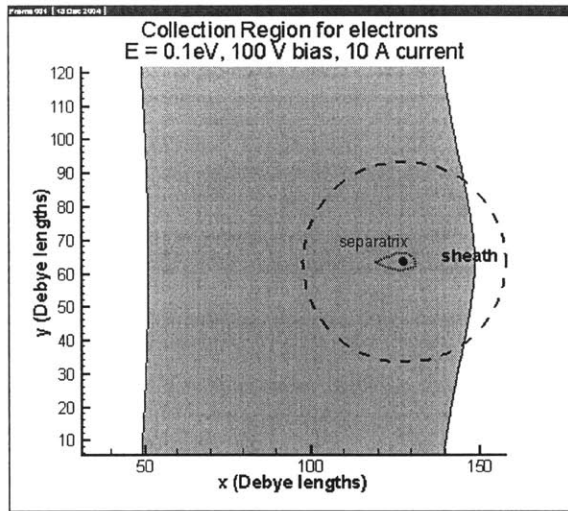


Figure 2-29:

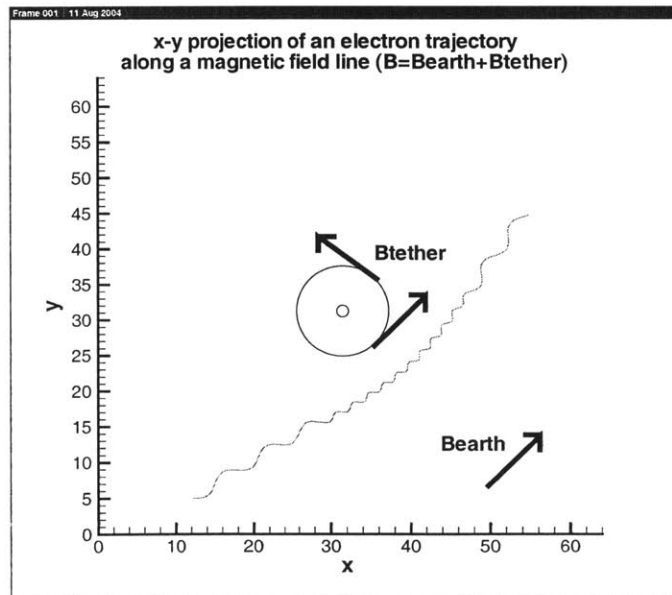


Figure 2-30:

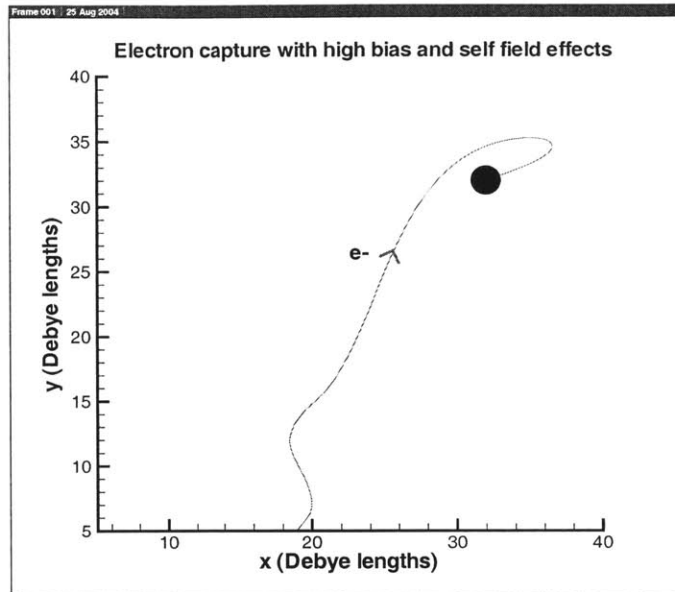


Figure 2-31:

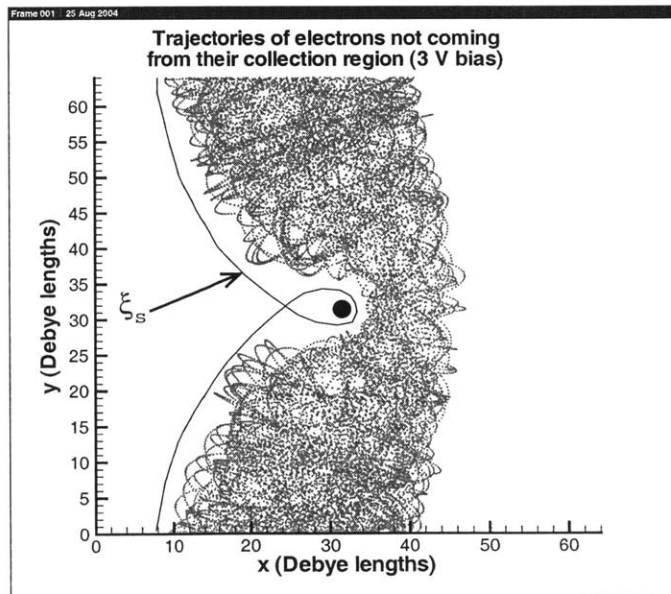


Figure 2-32:

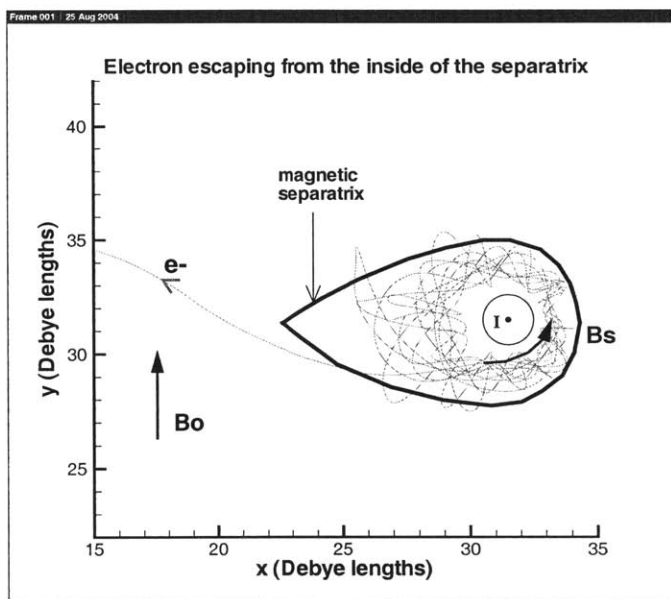


Figure 2-33:

Chapter 3

Current collection: benchmarking with symmetric cases

A first way to validate both the way particles are moved on the mesh and our boundary conditions is to test the statistical physics simulated by the code. Therefore, we computed the particle flux into the tether for several well-known cases, without looking at the microphysics of the collection, that is to say without considering the particle trajectories.

3.1 Thermal current in non-magnetized plasma

3.1.1 Beam current

Orbital velocity, magnetic field, and tether bias were set to zero, which means particle motion is merely thermal (reminder: collisions are neglected). The collected current into the tether is due to this thermal motion only.

The thermal current for a Maxwellian plasma (Equation 1.8 or 1.4) can be expressed from the code parameters. For $n_e = n_i = n_\infty$ and $T_e = T_i$:

$$J_{te}^{sim2V} = \frac{1}{\Delta t} \sum_k \frac{(-e \cdot w_k) dv_x dv_y}{2\pi R}, \quad (3.1)$$

$$J_{te}^{sim3V} = \frac{1}{\Delta t} \sum_k \frac{(-e \cdot w_k) dv_x dv_y dv_z}{2\pi R} \quad (3.2)$$

with k in the set of macro-electrons which have crossed the tether boundary during Δt . A similar expression holds for ions. w_k is the weight of a macro-particle, attributed when the particle was created, according a two-dimensional Maxwellian distribution. It is related to the density by:

$$\sum_{k=macroe^-/macroions} w_k dv_x dv_y \simeq \iint \frac{n_\infty}{\pi \times 2v_{tk}^2} \exp \frac{-(v_x^2 + v_y^2)}{2v_{tk}^2} dv_x dv_y = n_\infty, \quad (3.3)$$

in 2V, and:

$$\sum_{k=macroe^-/macroions} w_k dv_x dv_y dv_z \simeq \iiint \frac{n_\infty}{\pi \times 2v_{tk}^2} \exp \frac{-(v_x^2 + v_y^2 + v_z^2)}{2v_{tk}^2} dv_x dv_y dv_z = n_\infty, \quad (3.4)$$

in 3V, where:

$$v_{tk} = \sqrt{\frac{T_k}{m_k}}. \quad (3.5)$$

Note that with this definition, $T_k = m_k v_{tk}^2$ and NOT $\frac{1}{2} m_k v_{tk}^2$, as might be expected. This yields:

$$J_{te}^{sim} = -[e \times nb(e^-)]_{into\ tether} \times \frac{1}{2\pi R} \times \sqrt{2\pi} = \sqrt{2\pi} \times J_{te}^{th}, \quad (3.6)$$

$$J_{ti}^{sim} = [e \times nb(ions)]_{into\ tether} \times \frac{1}{2\pi R} \times \sqrt{2\pi} = \sqrt{2\pi} \times J_{ti}^{th} \quad (3.7)$$

for both 2V and 3V velocity distributions.

With the theoretical values given by Equation 1.8 or 1.4 for a Maxwellian distribution:

$$J_{te}^{th} = -\frac{1}{\sqrt{2\pi}} en_{\infty} v_{te}, \quad (3.8)$$

$$J_{ti}^{th} = \frac{1}{\sqrt{2\pi}} en_{\infty} v_{te} \sqrt{\frac{m_e}{m_i}}, \quad (3.9)$$

with $v_{te} = \sqrt{\frac{T_{e0}}{m_e}}$.

Therefore, after a normalization by $en_{\infty} v_{te}$, as operated in the code, we expect:

$$J_{te}^{sim} = -1, \quad (3.10)$$

$$J_{ti}^{sim} = \sqrt{\frac{1}{16 \times 1836}} = 5.8 \times 10^{-3} \quad (3.11)$$

For a discretized 2V Maxwellian distribution, as created in our code, we get $nv_x \times nv_y \times nv_z$ beams in the two creation zones ($n_x \leq 10$ and $n_x \geq n_x^{\max} - 10$), which different velocities and weights are attributed to, according to a 2V or 3V Maxwellian distribution. With such identical beams in each cell, we get no density or electric fluctuations without an external perturbation such as a non-uniform particle background or an initial electric perturbation ("quiet start").

The exact density and current flux through a surface $\{x = cst\}$ can then be written in these regions:

$$n = \sum_{i_{v_x}=-n_{v_x}/2}^{n_{v_x}/2} \frac{1}{\sqrt{2\pi}} \exp\left(-\frac{(v_x^i)^2}{2}\right) \times \sum_{i_{v_y}=-n_{v_y}/2}^{n_{v_y}/2} \frac{1}{\sqrt{2\pi}} \exp\left(-\frac{(v_y^i)^2}{2}\right) dv_y$$

$$n_{2V} = \sum_{i_{v_x}=-n_{v_x}/2}^{n_{v_x}/2} \frac{1}{\sqrt{2\pi}} \exp\left(-\frac{(v_x^i)^2}{2}\right) \times \sum_{i_{v_y}=-n_{v_y}/2}^{n_{v_y}/2} \frac{1}{\sqrt{2\pi}} \exp\left(-\frac{(v_y^i)^2}{2}\right) dv_y \quad (3.12)$$

$$J_{t2V} = \sqrt{2\pi} \sum_{i_{v_x}=1}^{n_{v_x}/2} \frac{1}{\sqrt{2\pi}} v_x^i \times \exp\left(-\frac{(v_x^i)^2}{2}\right) \times \sum_{i_{v_y}=-n_{v_y}/2}^{n_{v_y}/2} \frac{1}{\sqrt{2\pi}} \exp\left(-\frac{(v_y^i)^2}{2}\right) dv_y, \quad (3.13)$$

for a 2V distribution and:

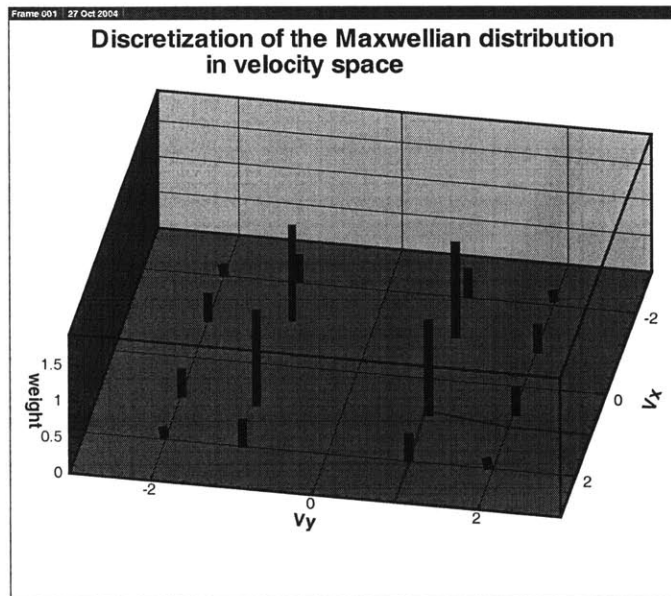


Figure 3-1: Discretization in velocity space. Each column represents a single macroparticle, whose weight is given by a Maxwellian velocity distribution. In this case, 16 particles by cell of each type are created.

$$n_{3V} = \sum_{i_{v_x}=-n_{v_x}/2}^{n_{v_x}/2} \frac{1}{\sqrt{2\pi}} \exp\left(-\frac{(v_x^i)^2}{2}\right) \times \sum_{i_{v_y}=-n_{v_y}/2}^{n_{v_y}/2} \frac{1}{\sqrt{2\pi}} \exp\left(-\frac{(v_y^i)^2}{2}\right) dv_y \times \sum_{i_{v_z}=-n_{v_z}/2}^{n_{v_z}/2} \frac{1}{\sqrt{2\pi}} \exp\left(-\frac{(v_z^i)^2}{2}\right) dv_z \quad (3.14)$$

$$J_{t3V} = \sqrt{2\pi} \sum_{i_{v_x}=1}^{n_{v_x}/2} \frac{1}{\sqrt{2\pi}} v_x^i \times \exp\left(-\frac{(v_x^i)^2}{2}\right) \times \sum_{i_{v_y}=-n_{v_y}/2}^{n_{v_y}/2} \frac{1}{\sqrt{2\pi}} \exp\left(-\frac{(v_y^i)^2}{2}\right) dv_y \times \sum_{i_{v_z}=-n_{v_z}/2}^{n_{v_z}/2} \frac{1}{\sqrt{2\pi}} \exp\left(-\frac{(v_z^i)^2}{2}\right) dv_z \quad (3.15)$$

for a 3V distribution., with $v_x^i = (i_{v_x} - n_{v_x}/2 - 0.5) \times dv_x$, $dv_x = \frac{v_x^{\max}}{n_{v_x}/2}$, $dv_y = \frac{v_y^{\max}}{n_{v_y}/2}$ and $dv_z = \frac{v_z^{\max}}{n_{v_z}/2}$. Velocities are in $v_{te} = \sqrt{\frac{T_{e0}}{m_e}}$ units, electric charges in e units and we also normalized by n_{∞} .

The tables presented below show, for several discretizations, the corresponding simulated unperturbed densities and thermal current fluxes. For rough discretization, the unperturbed density (in the creation zones) and the normalized thermal flux are quite far from n_{∞} and $J_{tk}^{norm} = \pm \sqrt{\frac{m_e}{m_k}}$, respectively. But they tend quickly to these values. The discretizations $v_{x,y,z}^{\max} = 3$ and $n_{v_{x,y,z}}/2 = 3$ in 2V and $v_{x,y,z}^{\max} = 2$ and $n_{v_{x,y,z}}/2 = 3$ in 3V, for instance, seem accurate enough and is usually still affordable given our computational restrictions. Moreover, far enough from the creation zones, the discretized Maxwellian plasma becomes almost perfectly Maxwellian if it remains undisturbed (cf. Chapter "Current collection: benchmarking in symmetric cases")

I_{th}^{2D}			
$n_v \setminus v_{\max}$	1	2	3
1	0.602	1.01	0.12
2	0.481	1.09	1.26
3	0.461	1.02	1.1
5	0.454	0.99	1.032

n_0^{2D}			
$n_v \setminus v_{\max}$	1	2	3
1	0.679	0.572	4.54e-2
2	0.617	0.993	0.927
3	0.607	0.99	1
5	0.601	0.988	1

I_{th}^{3D}			
$n_v \backslash v_{\max}$	2	3	5
1	1.17	1.14	0.963
2	0.894	1.12	1.31
3	0.854	1.04	1.16
5	0.836	1.003	1.05

n_0^{3D}			
$n_v \backslash v_{\max}$	2	3	5
1	0.933	0.604	0.307
2	0.926	0.997	0.837
3	0.918	0.996	0.997
5	0.917	0.995	1

These values were checked accurately up to the third digit by computing the particle flux in the $x \geq 0$ direction through a line $x = cst$ in the creation zone $\{0 \leq n_x \leq 10\}$.

3.1.2 Plasma Maxwellization and thermal current

The initial plasma in the whole domain is constituted of (typically 4×4 or 6×6) homogeneous beams, which constitutes the "quiet start" presented in the previous section. At every time step, similar beams are created in the boundaries and supply the domain with particles. So, without any perturbation, these beams propagate throughout the domain without fluctuations, supplied by each injector.

Nonetheless, if a small perturbation is introduced in the physical domain, such as, for instance :

- random density or electric fluctuations at $t = 0$.
- presence of a fixed charge in the domain, as it is the case, when a tether is modelled,

these beams become unstable by mutual interaction. This phenomenon is called "streaming instability" or "beam instability" (cf. [29]Swanson[1989], pp.112-117). The simplest case is the "two-stream instability", considering two interpenetrating beams. [29]Swanson predicts in this case an exponential growth of the electric fluctuations. The electric field energy density, proportional to E^2 should grow at a rate $\gamma = 2\omega_{pe}$, yielding:

$$E^2(t) \propto \exp[2\omega_{pe}t]. \quad (3.16)$$

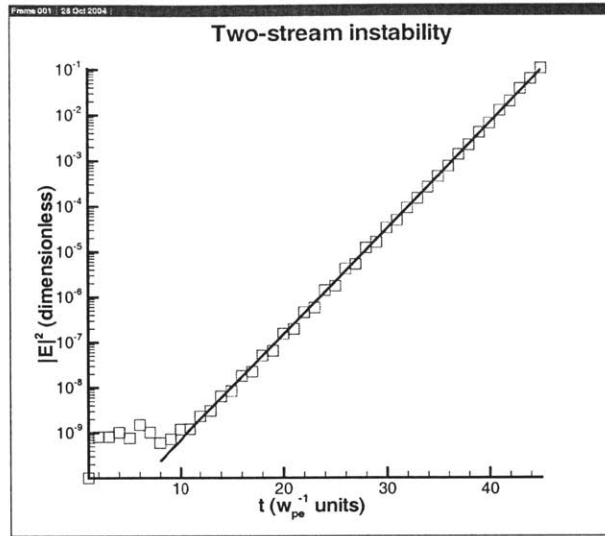


Figure 3-2: A simulation is run with beams in opposite directions throughout the domain. At the start, small random spatial electric fluctuations are artificially introduced. The plot shows the growth of mean normalized electric energy density in the domain, due to unstable interactions between the interpenetrating beams. We get a growth rate $\gamma_{sim} \simeq 2.2\omega_{pe}$, close to the expected rate $\gamma_{th} \simeq 2\omega_{pe}$.

Starting with small random spatial electric fluctuations everywhere in the domain, we observed such instabilities, growing exponentially at a rate close to ω_{pe} , as predicted, as shown by Figure 3-2.

These beam instabilities are the fundamental phenomenon allowing to get a continuously Maxwellian plasma from a given set of beams originating from every cell of the domain.

Computing the thermal current only allows to validate basic statistical properties of the simulated plasma, namely the mean or thermal particle velocity, which is the 1st order momentum of the velocity distribution. The amount of collected current through a given boundary by pure thermal motion is indeed not a function of the distribution shape but only of its mean value. Nonetheless, when the plasma flow and external magnetic field are taken into account, the amount of collected current depends on the whole shape of the particle velocity distribution. The OML current (Equation 1.23) itself is calculated by assuming a Maxwellian distribution for background electrons. Latest analytical developments by [17]Laframboise (1997) are also based on this assumption.

In our code, all particles are initially created in the domain according to a roughly discretized (shifted) Maxwellian distribution. Therefore, at $t = 0$, the particle distribution is everywhere a rough approximation of a Maxwellian function. We shall thus verify that after some acceptable computation time, the distribution becomes nearly Maxwellian. However, our system is open, for particles are created at the beginning of each iteration in two ten-cell wide stripes on the left and on the right of the domain, and all particles inside these stripes at the end of an iteration are immediately destroyed.

This means that the incoming particle flux into the domain, from $n_x \leq 10$ or from $n_x \geq n_{x \max} - 10$, are far from being Maxwellian distributed, even after many iterations.

As a consequence, in order to get nearly a (shifted) Maxwellian plasma flowing to the tether, there must be enough room between the left and right boundary of the domain to let the plasma spatially evolve from a roughly discretized Maxwellian into a nearly Maxwellian distribution, hoping that it actually occurs. Our model is collisionless, like the ionospheric plasma, so the evolution of the particle distribution is only due to electromagnetic interactions.

We built statistical diagnostics in our domains to be able to measure directly the particle distribution at each step of the simulation in a well-chosen sub-domain. In a given box inside the domain, electrons or ions in a given horizontal velocity range $[v_x, v_x + dv]$ are counted, where dv is the resolution of the counting process. For very small sub-domains (a few cells), the number of macro-particles in the box was insufficient to get satisfactory statistical results, such that we had to count over hundreds or thousands of time steps. The corresponding distribution is the easily given by plotting the number of particles in each $[v_x, v_x + dv]$, versus $v_x + \frac{dv}{2}$. Of course, a similar process is applied for v_y , and the temperature (cf. Equations 3.17) .

In each simulation, we checked that in a large enough domain, the plasma flowing to the tether was Maxwellian within a few percent. The domain has to be long enough along x , in order to allow the flowing plasma to evolve to a continuous Maxwellian distribution before it reaches the tether. Because of the huge real mass of the oxygen ions which give them inertia compared to the electrons, we don't expect the ion velocity distribution to evolve significantly from the original discretized distribution, even after several thousand of steps. Because the ions are not the collected species, this departure from a continuous distribution should only have

little indirect influence on the electron collection. Figures ?? and 3-4 show that a distance less than $\sim 10^2 \lambda_{De}$ between the left creation zone and the tether allows the electron gas to reach a continuous Maxwellian distribution in the tether vicinity with an orbital velocity $8 \times 10^5 \text{ cm.s}^{-1}$. Figure 3-4 show that the final simulated distribution fits perfectly a continuous 2V Maxwellian, with the given thermal velocity $v_{te} = \sqrt{\frac{T_{e0}}{m_e}}$. The slow ion dynamics does not allow relaxation of the discretized Maxwellian created in the boundaries to a continuous distribution, when there is an orbital velocity (8km/s flow). This probably does not change the electron collection, which depends on the ion density map, but not on the accurate shape of the ion energy distribution.

3.2 OML current

The next case of interest to provide with more advanced benchmarking of the code is the OML regime. We chose a one Debye length radius probe, corresponding to the limit of the OML regime. Simulations were run for varying positive bias and thus electron collection. The orbital velocity and magnetic field were still set to zero, corresponding to the axisymmetric OML regime case.

3.2.1 Potential topology characterization

Sanmartín [25] introduced a way of plotting the electric potential, based on the OML condition 1.26, which allows to check easily if a current collection regime (in cylindrical geometry) is Orbit Motion Limited. The potential $\Phi(r)$ is plotted versus $(R_p/r)^2 \Phi_p$. The OML condition 1.26 implies graphically that the half-space below the bisector line $\Phi(r) = (R_p/r)^2 \Phi_p$ is completely forbidden in the OML regime. Thus, a regime cannot be OML if some part of the plot lies below this bisector. Moreover, even if no specific potential function is required to be in the OML regime, the curve in this plot must have certain features, corresponding to the various concentric layers in the surrounding plasma (cf. Appendix III):

- as $(R_p/r)^2 \Phi_p \rightarrow 0$, $\Phi(r)$ tends to 0 with infinite slope, since $\Phi(r) \underset{r \rightarrow \infty}{\sim} \frac{1}{r}$, due to quasi-neutrality in the background plasma. In order to verify this asymptotic feature, a very

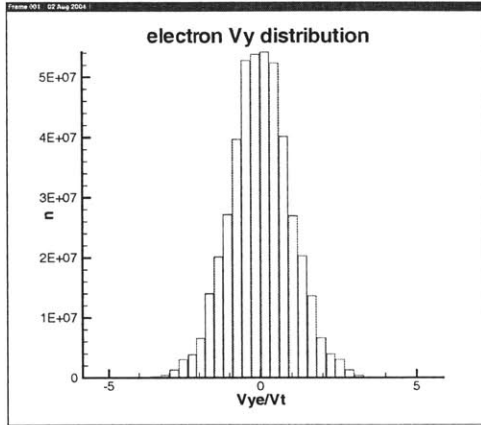


Figure 3-3: Electron V_y distribution $124 \lambda_{D_e} (\simeq 1m)$ after the creation zone at orbital velocity 8 km/s

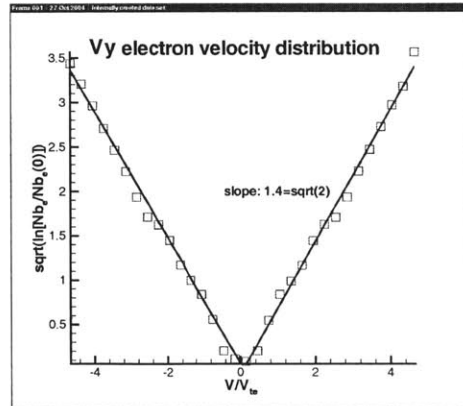


Figure 3-4: The actual distribution fits with a Maxwellian $\propto \exp \left[-\frac{v^2}{(\sqrt{2}v_{te})^2} \right]$

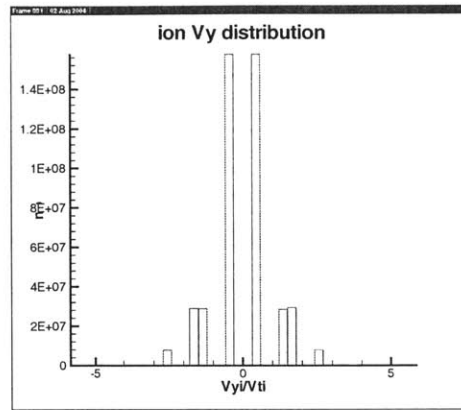


Figure 3-5: Ion V_y distribution $1m$ behind the creation zone at orbital velocity $8km/s$: Because of the ion inertia, the discretized Maxwellian does not completely relax to a continuous distribution

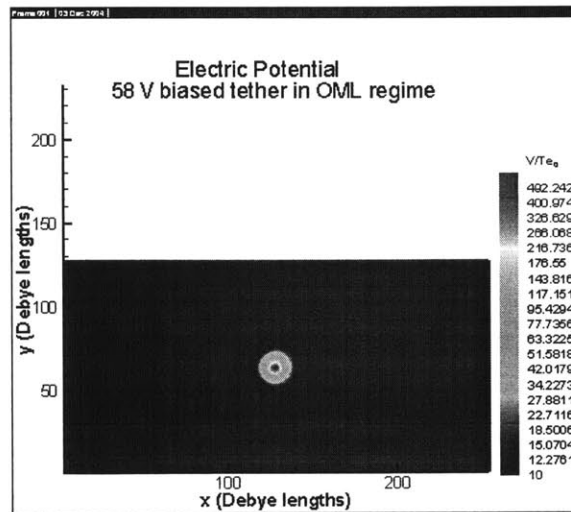


Figure 3-6: The potential map shows a strong shielding effect on the potential, on a typical distance around the sheath radius. The time-averaged potential outside the sheath equals the faraway boundary potential.

large domain must be simulated. No previous simulation was able to grasp this asymptotic behavior.

- $r^2\Phi(r)$ exhibits a minimum at point $r = r_0$, which lies typically far outside the sheath. This point 0 is the nearest point from the "forbidden domain" in the OML regime (and the farthest into the "forbidden domain" if the regime is non-OML).
- The sheath radius $r = R_s$ lies at point 1, where the slope is the highest on the plot. Although $\frac{\partial\Phi}{\partial r}$ theoretically diverges at point 1, which is the limit of the sheath, we get a finite slope here on our plots.
- Then, close to the probe, $r^2\Phi(r)$ exhibits a maximum at point 3, where the plot is the farthest from the "forbidden domain".
- Eventually, the plot reaches the bisector at (Φ_p, Φ_p) .

Figures 3-8 and 3-10 show such plots for two symmetric regimes. Figure 3-8 corresponds to a positively biased small probe: $R = \lambda_D$, whereas Figure 3-10 exhibits the same plot for a bigger probe: $R = 2\lambda_D$. The overall behaviour of this modified potential plots in cylindrical geometry corresponds to Sanmartín[25] expectations. The characteristic points 0, 1 (sheath radius), 3 and probe are represented. For $R = \lambda_D$ (Figure 3-8), the entire plot remains in the upper half-space, according to OML condition, which is verified for such a small probe. When the probe radius is larger ($R = 2\lambda_D$ in Figure 3-10), the plot enters the lower "forbidden" domain, violating thus the OML condition. This occurs indeed when the probe radius is larger than the Debye length, according to the Chapter "Theory of current collection by a probe in a plasma". Please note the use of log-log scales on the right to emphasize the potential behaviour outside the sheath. As expected, the regime is OML with the small probe, but beyond OML with the bigger one.

An important point is that on both plots, the entire potential topology described above is well represented, up to the asymptotic behavior at $r \rightarrow \infty$.

As mentioned in Chapter "Particle Trapping", the simulated potential is modified by an important trapped population living in the sheath, which should be taken into account in any self consistent analytical calculation.

3.2.2 Particle and charge densities

The average O^+ ion and electron density were computed in each cell of the mesh and normalized by the background space plasma density. The corresponding density plots are shown on Figures 3-11 to 3-12.

They show the typical known feature of the OML regime for electron collection: The cylindrical ion depleted area around the tether (Figure 3-12) is the sheath, which is the only non quasineutral region of the domain. Indeed, the ion density decrease at the sheath boundary is very sharp, which allows to go quickly from the quasineutral background plasma to the non-neutral sheath.

Outside the sheath, both particle densities fluctuate around the background space plasma density. These fluctuations are a well-known feature of all PIC simulations and are due to the particle discretization, namely the relatively small number of macro-particles per cell. These numerical fluctuations decrease when the number of macro-particles per cell is increased, but a compromised has to be found in order to keep affordable computation time. The following plots correspond to 16 and 36 particles of each species per cell.

Inside the sheath, the electron density decreases as well but does not vanish, for the electron flux into the sheath is strictly positive due to the positive tether bias. This induces a negative space charge inside the sheath, which acts as an effective Debye shielding of the positive bias. At high potential, the electron density builds up dramatically in a small cylinder around the tether, reaching a peak density which can be of the order of ten times the background density, at a few Debye length from the tether, and eventually decreasing sharply when reaching the probe.

The electron density in the OML regime had been calculated by Laframboise and computed by Choinière and Gilchrist (unpublished), who showed as well such a density build up very near the tether. However, much smaller peak and probe surface densities were calculated in their model (not a self-consistent PIC, unlike ours). Indeed, both Choinière and Gilchrist (unpublished) and Laframboise iterative calculations neglected the existence of trapped electrons in the sheath. Because of particle trapping near the tether, further studied in Chapter "Particle Trapping", dedicated to this phenomenon, most of this density build up is due to negative

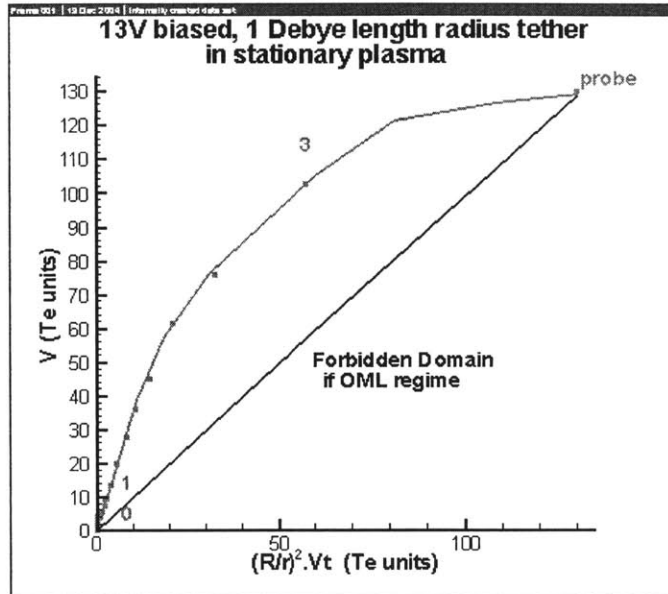


Figure 3-7:

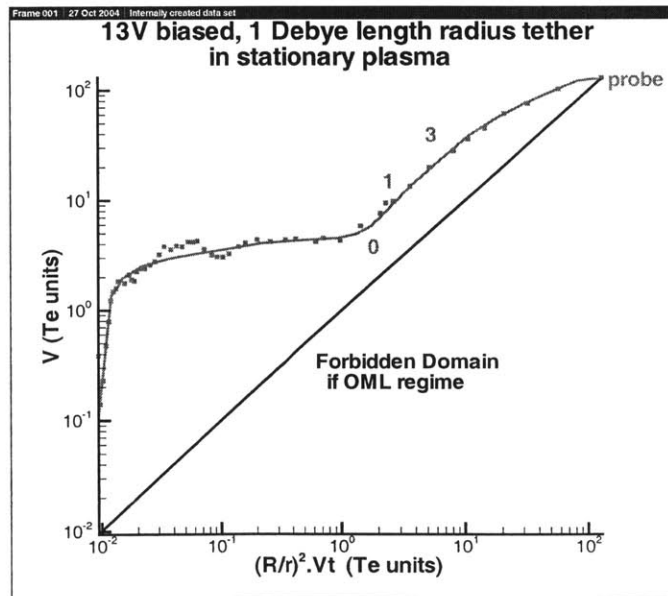


Figure 3-8:

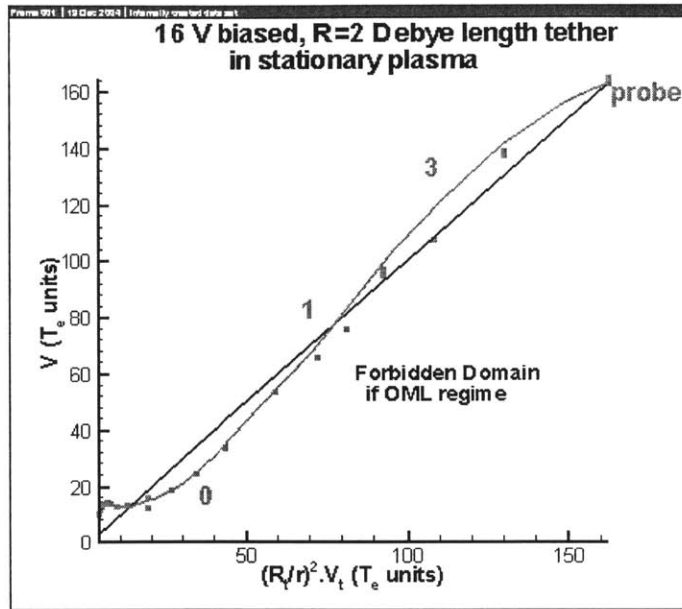


Figure 3-9:

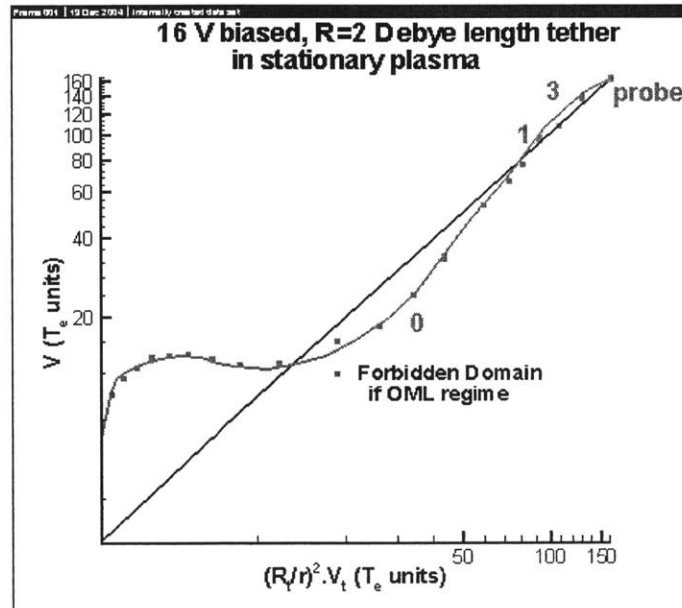


Figure 3-10:

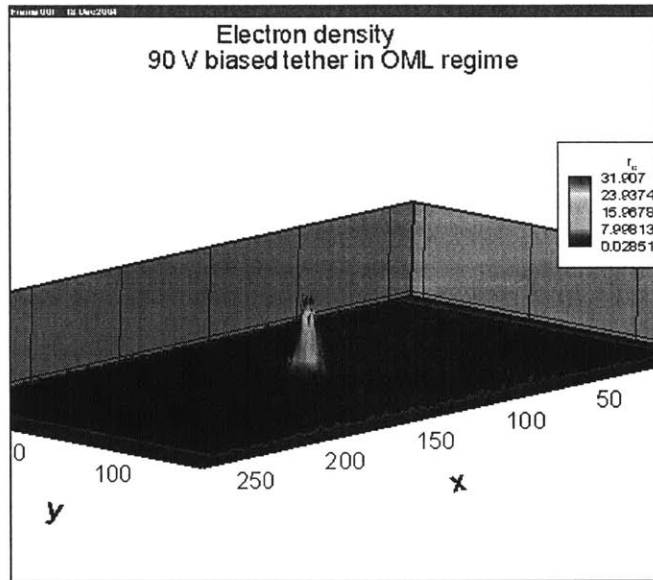


Figure 3-11: The most interesting feature of the electron density is the formation of a dense accretion disk around the tether, which is further studied in the Chapter "Particle trapping".

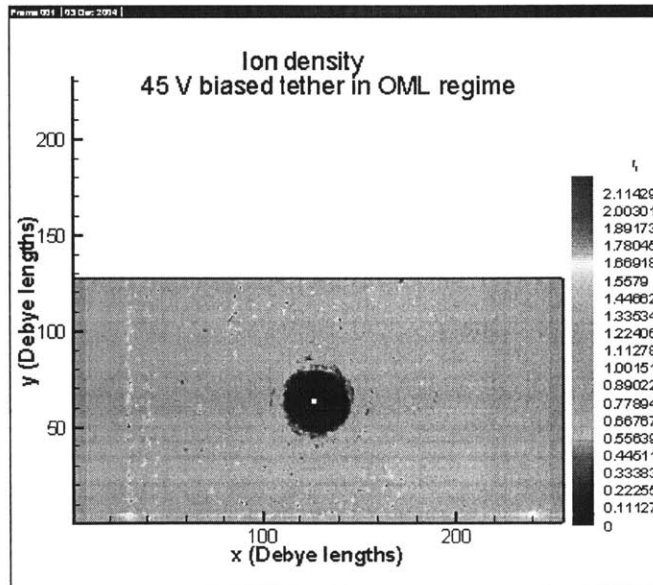


Figure 3-12: The ion density map exhibits clearly the presence of an ion depleted sheath. Outside the sheath, the ion density increases almost directly to the background density.

energy particles, orbiting indefinitely around the tether without being captured. No matter how important this effect is, it should be emphasized here, that even if this effect might affect the local potential, the current collection regime remains OML as long as no effective potential is built. The potential plot of the previous sub-section (Figure ??) illustrates that it is not the case in our simulations. Although particle trapping and density build up should be further understood, we can thus assess that current collection occurs in the OML regime for our axisymmetric cases. Note that no such reasoning can be held for non-symmetric cases, when the orbital velocity or the magnetic field are taken into account.

3.2.3 Sheath

The sheath radius was taken from our PIC simulations in a range of tether biases, as shown on Figure 3-13. The sheath size, which is independent of the particle mass ratio, grows with the tether bias, approximately $\propto \Phi^{\frac{3}{4}}$. These results can be compared with Sanmartín theory and the computational results provided recently by Choinière and Gilchrist (cf. Equation 1.11)

3.2.4 Complex dynamics

Outside the sheath, particle trajectories and streamlines confirm that the motion is basically thermal. As shown in the next sub-section, the plasma is Maxwellized in this background region, without any coherent motion. The average velocity is zero.

At the sheath boundary, where the probe potential starts acting on particles, the electrons are suddenly attracted towards the probe, as shown by the electron streamlines map (Figure 3-14). They seem approximately radial in the region inside the sheath and outside the smaller "accretion" disk surrounding the probe.

Nonetheless, the electron dynamics gets much more complicated in this "accretion" disk where the density suddenly builds up. The linear momentum of most electrons, which is high due to a strong acceleration from the sheath boundary, is mainly converted into angular momentum, as suggested by the rotating streamlines inside the "accretion" disk. Although the average electron velocity indicates an average radial motion into the probe, inducing current collection,

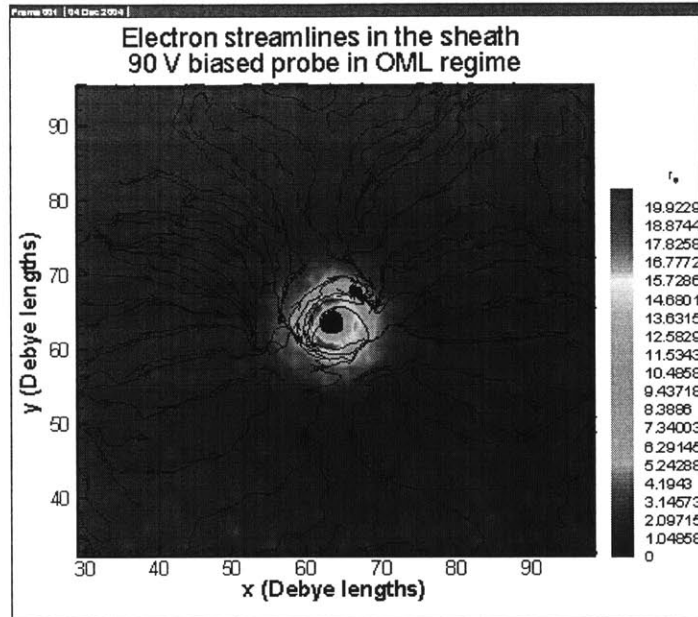


Figure 3-14: This accretion disk is embedded in the sheath. The electron dynamics shows global attraction to this dense disk, and then a complex dynamics inside this area, where most electrons seem to be orbiting around the tether and the flow is turbulent.

the streamlines topology in this small region is actually much more complex, and fluctuates with time, which suggests that the electron flow is turbulent there.

Since the flow is not steady there, the streamlines do not correspond to particle trajectories. It becomes clear in Chapter "Particle Trapping" that the global dynamics should be studied separately between free particles and particles which are going to be captured by the probe and orbiters, which are rotating around the probe for a very long time. The existence of many orbiters near the probe explains why the streamlines are not radial anymore in the "accretion" disk.

3.2.5 Temperature and velocity distribution

The time-averaged ion and electron temperatures are computed in every cell. They are computed as follows for each species and in every cell:

$$T_{x,y,z} = \frac{\sum_k w_k m \left(v_{x,y,z}^k - \langle v_{x,y,z}^k \rangle_k \right)^2}{\sum_k w_k} = m \left[\left\langle \left(v_{x,y,z}^k \right)^2 \right\rangle_k - \left\langle v_{x,y,z}^k \right\rangle_k^2 \right], \quad (3.17)$$

$$T = \frac{1}{n_{dv}} (T_x + T_y + T_z), \quad (3.18)$$

where $\{k\}$ is the set of macroparticles in the corresponding cell, w_k the numerical weight of each macroparticle, $v_{x,y}$ its velocity components, n_{dv} the velocity space dimension (2 or 3) and $\langle \dots \rangle_k = \frac{\sum_k (w_k \dots)}{\sum_k w_k}$ is the weighted average over the macroparticles in the cell. For the 2V version, T_z is set to zero. These definitions yield $T = T_x = T_y$ ($= T_z$ in 3V) uniformly in an unperturbed plasma (benchmarking shown in Figure 3-15).

When a steady state is obtained, the instantaneous temperature is the averaged over time in order to get rid of numerical spatial fluctuations.

The electron temperature maps with a collecting probe are plotted in Figures 3-16 and 3-17. The ion temperature equals the space plasma temperature throughout the domain, except the ion depleted sheath.

The electron temperature increases exponentially from the sheath boundary, where it is still close to the background temperature to the tether surface. This actually means that the probe bias does not induce only coherent motion for the electrons. Even in the outer part of the sheath (outside the "accretion" disk), thermal motion is created by the tether in addition to radial acceleration. Indeed, this can be easily understood if one takes into account that most electrons that are accelerated towards the probe actually miss it to the its small size and the non-zero azimuthal component of the particle velocity. These particles keep on living in the sheath without being captured, and have a very high velocity, due to the previous acceleration by the (missed) tether. Since this phenomenon occurs randomly in every direction, thermal motion is induced, yielding a temperature increase near the tether. This phenomenon is merely due to the potential bump in the sheath, so the temperature increase should follow the potential spatial variations.

Figure 3-18 shows the time averaged ratio $\frac{e\Phi}{kT_e}$ throughout the domain, which compares ther-

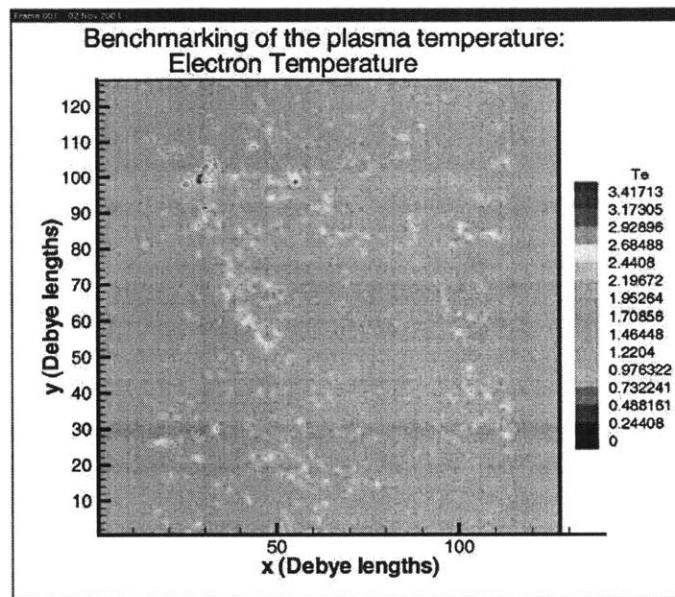


Figure 3-15: This instant shot of the electron temperature in an unperturbed plasma shows that the normalized temperature fluctuates around unity. The fluctuations are numerical artefacts, due to the finite number of particles per cell.

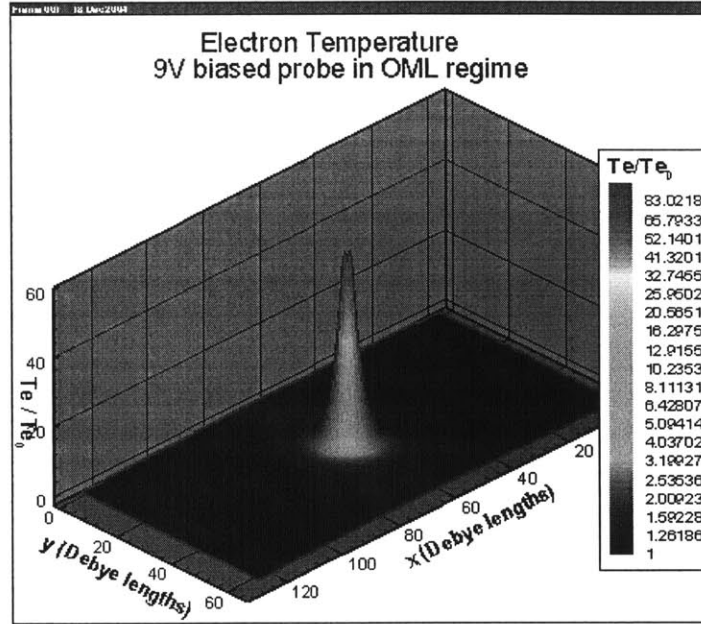


Figure 3-16: For a low bias (9V), the electron temperature remains at the background level T_{e0} outside the sheath.

mal and potential energy for electrons. Note that, even if the electron temperature is typically 5 times higher than the background temperature T_{e0} in the whole simulated domain for the 45V bias case, the potential-temperature ratio is very close to unity everywhere in the physical domain, except in the vicinity of the tether. This means that the whole $256 \times 128 \lambda_{De}^2$ domain lies in the presheath, where the potential is still significantly positive ($e\Phi \simeq 5kT_{e0}$). In the sheath, this ratio increases above unity, which means that the potential energy is not entirely converted macroscopically into thermal energy. Indeed, inside the sheath, the potential energy is also converted into macroscopic electron kinetic energy, electrons being accelerated towards the probe (there, the local mean velocity is significantly higher than the thermal velocity).

3.2.6 Current collection

The collected current in the OML regime was computed with respect to time for various biases. In order to avoid long transient times in each run, we started with the lowest potential of the chosen range (14V), waited for the steady state, and then increased the potential step by step,

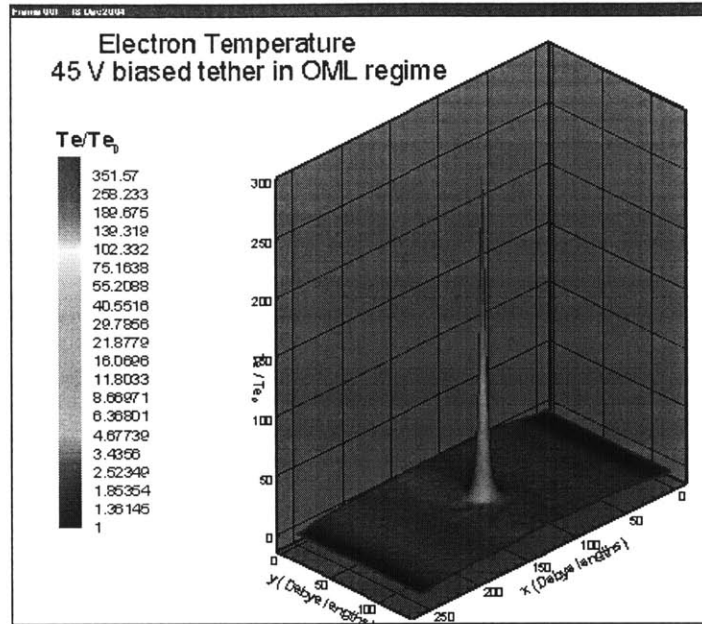


Figure 3-17: For higher biases (45V), the temperature in most of the domain is a few T_{e0} , due to the large extent of the presheath ($\frac{e\Phi}{kT_{e0}} > 1$ in the whole domain).

waiting for the new steady state at every step.

In all cases, the ion (repelled species) current was reduced to zero. So, the total current is the electron current only. The following plots (Figures 3-19,3-20,3-21,3-22) are time averages over 10 Langmuir plasma periods T_{pe} , which allow the suppression of the fast oscillations due to the particle discretization (the small number of particles per cell induces a discontinuous current). The collected current is normalized by the thermal current, which is the reference for a probe at floating potential. The horizontal lines correspond to the expected OML current given by Formula 1.23. In spite of a time average over $10T_{pe}$, fluctuations by more than 10% remain, but the mean value stabilizes towards a steady state, which seems to be attained in all cases.

Note that the transient time from a uniform density state is not apparent on these plots, since we started each run from a previous state, close to the expected final steady state.

The average value of the collected current in each steady state is close to the theoretical OML current, though always a few percent higher.

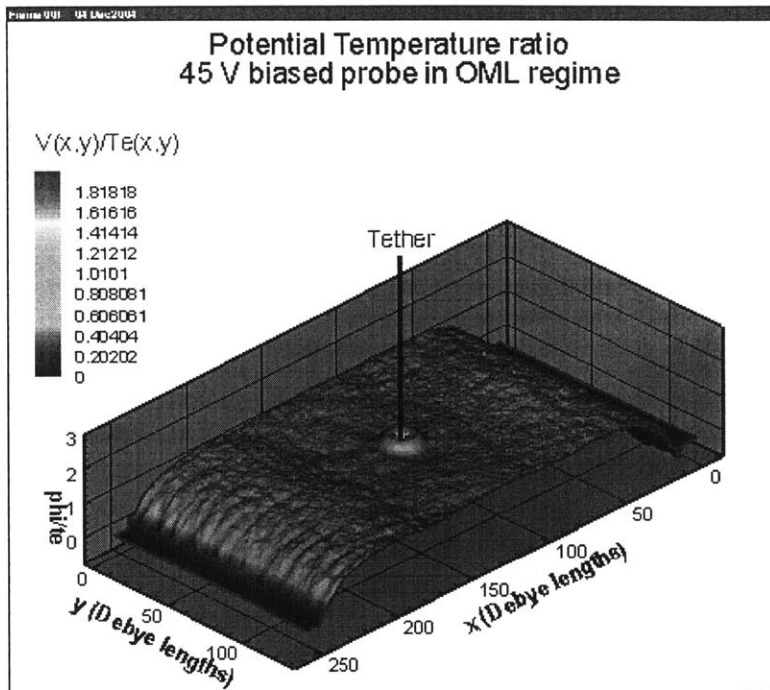


Figure 3-18:

Figure 3-23 summarizes the results, showing the average collected current as a function of the tether bias. The power-fit curve lies very close to the theoretical OML current curve, given the uncertainty due to the fluctuations. Nonetheless, a slight overshoot in current collection can be seen on every plot, which is further explained in Chapter "Particle trapping".

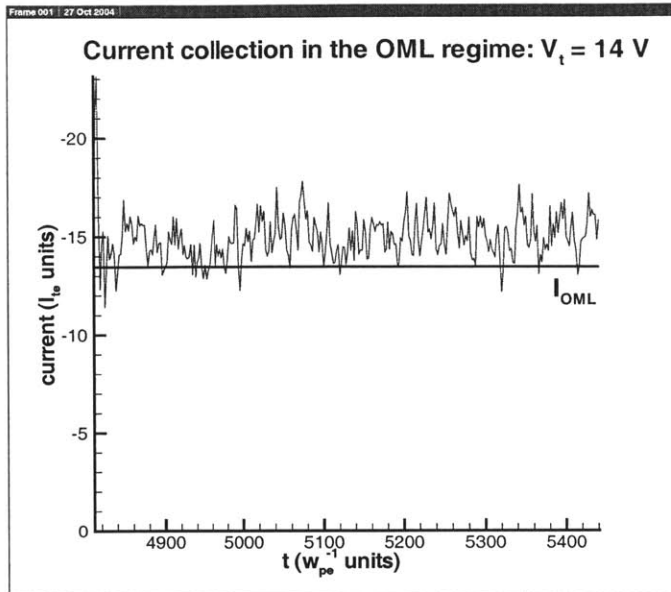


Figure 3-19:

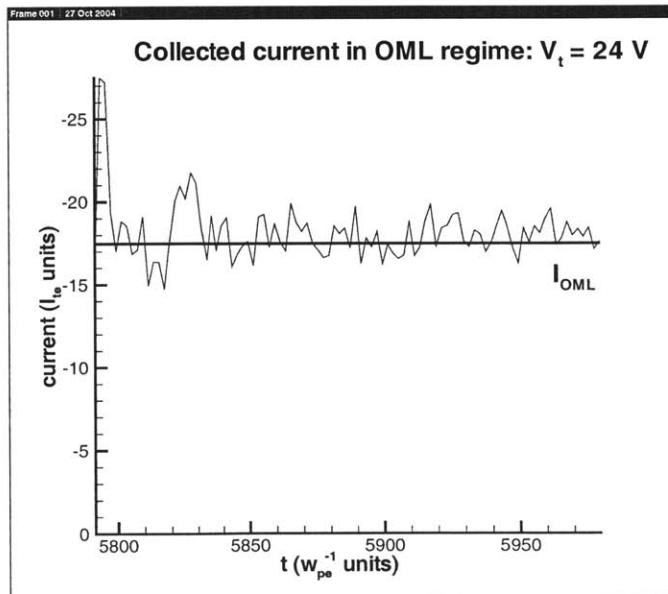


Figure 3-20:

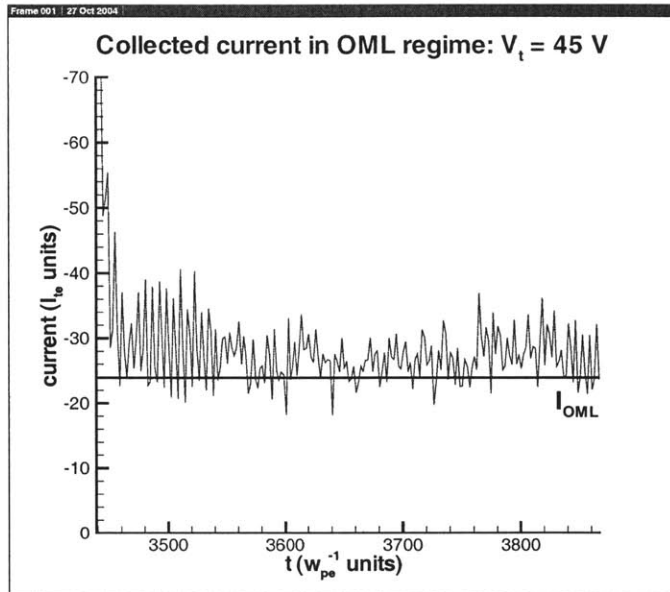


Figure 3-21:

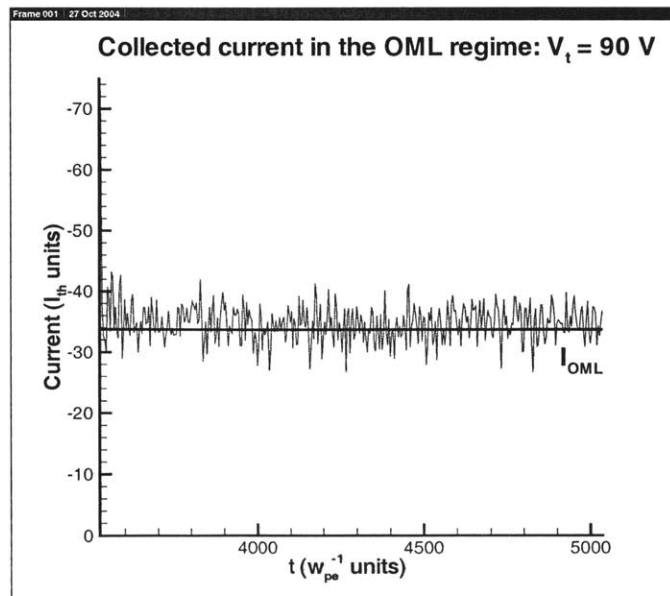


Figure 3-22:

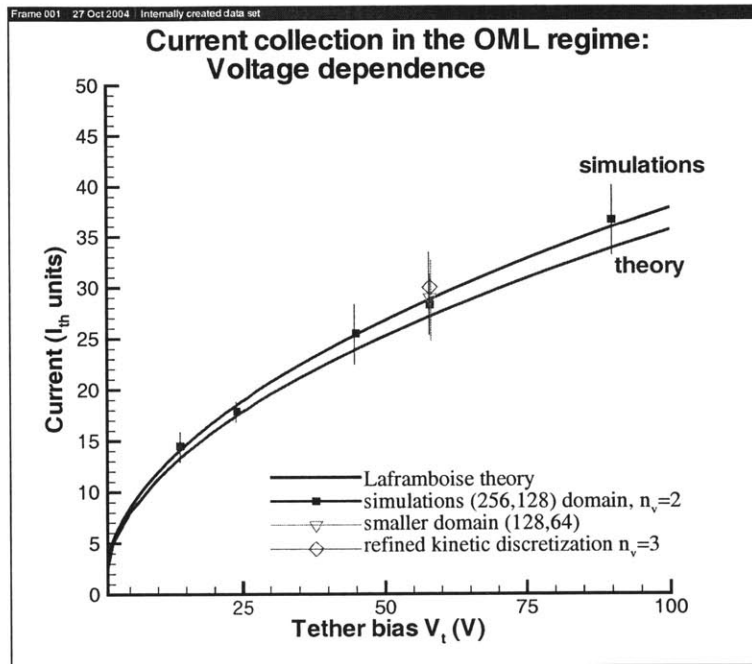


Figure 3-23: The collected current computed from our PIC simulation is very close to the OML upper bound, predicted for this case (no flow and tether radius below 1 Debye length). However, one can see a slight enhancement of the OML current, which is explained by numerical collision effects (cf. Chapter on "trapping")

Chapter 4

Current collection results for asymmetric cases

Of course, accurate theories could already predict current collection in symmetric cases, even if the whole structure of the plasma is not fully understood yet. On the contrary, no theory can accurately predict the amount of collected current for asymmetric, and thus more realistic cases, when the satellite orbital velocity, the Earth's magnetic field and also the self-induced magnetic field are introduced in the physical model. Simulation results for these cases are therefore of great interest in order to predict current collection by ionospheric tethers in future space missions.

4.1 Orbital velocity effects

As explained previously, we simulate the orbital velocity by creating a flowing plasma in the boundaries. First, the magnetic field was neglected in order to focus on the effects of the mesosonic flow specifically, so the motional electric field E_m vanishes as well.

The same step by step procedure as in the OML regime was followed, from low to high bias, in order to get the plasma properties and collected current at various relevant tether bias, the orbital velocity being fixed at $8km/s$, typical for ionospheric satellites.

4.1.1 Potential

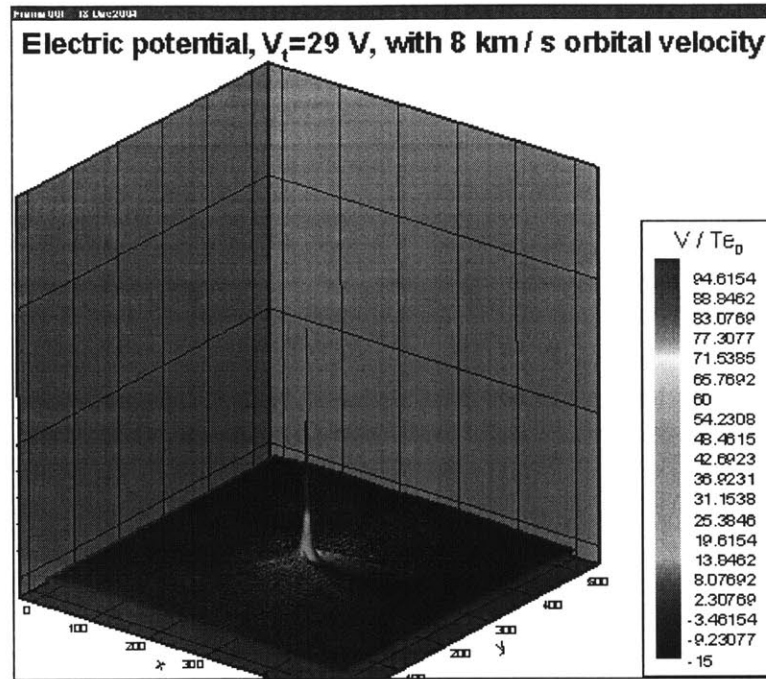


Figure 4-1:

Figures 4-1 and 4-2 show maps of the electric potential in steady state. Compared to the OML regime, the potential map is not axisymmetric. Indeed, a wake is created, where the potential is lower than the background potential (negative values). Also, slight wing-shaped potential bumps build up on each lower/upper side, which may act as potential barrier separating the inside and the outside of the wake. The extent of the wake is very large compared to the tether cross-section, but this is better evaluated on the density maps.

4.1.2 Particle and charge densities

Figures 4-5 and 4-5 show the electron and ion densities throughout the domain. The ion density map is typical for a hypersonic flow, as expected by using real mass ratio and a realistic orbital velocity. A "shock-like" density build up can be seen in front and on each side of the flow downstream the tether, separating the background plasma from the wake. The corresponding ion optics has been studied by T.Onishi and M. Martínez-Sanchez. One should note here,

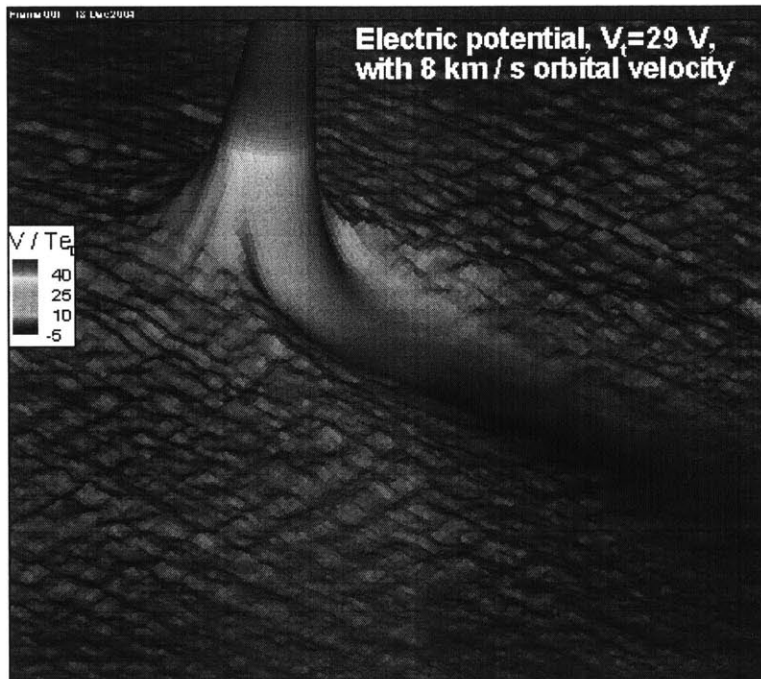


Figure 4-2:

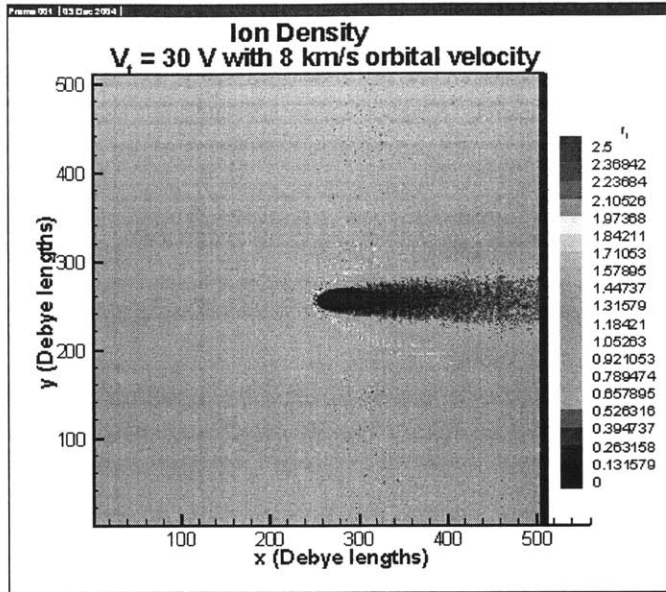


Figure 4-3:

that the extent of the density and potential perturbation due to the mesosonic flow onto the probe is very large, of the order of hundreds of Debye lengths. For the first time in tether PIC simulations, most of the wake could be simulated inside the domain, thanks to our Fast Poisson Solver, which allows us to simulate very large domains (up to $10^6 \lambda_{De}^2$ with a standard PC).

4.1.3 Current collection

The collected current was computed in the same bias range as the axisymmetric case (Figures 4-7, 4-8 and 4-9). The results are summarized and compared with the OML regime in Figure 4-10. The orbital velocity turns out to have a great enhancement effect on current collection. The current collection is about twice higher as the OML limit in the whole bias range, much higher than the 10% enhancement observed by [27]Choinière and Gilchrist, as a result of two counterbalancing effect. First, they observed indeed an electron density overshoot in the presheath, upstream to the probe, which is assumed to yield collection enhancement. Second,

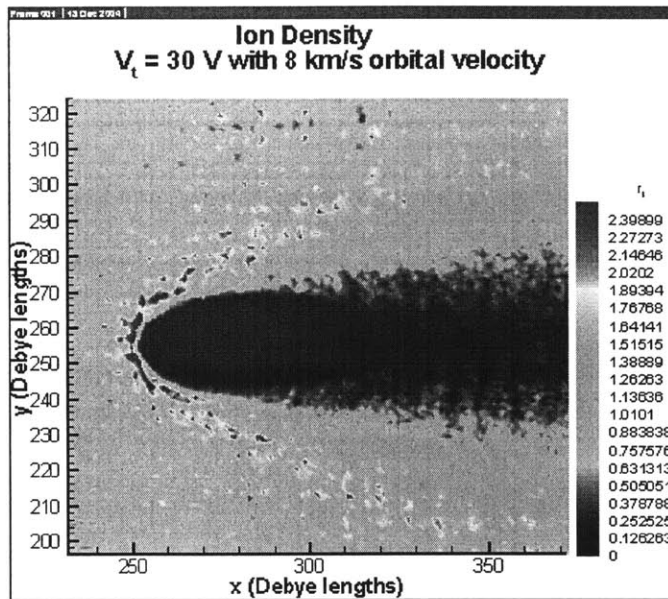


Figure 4-4:

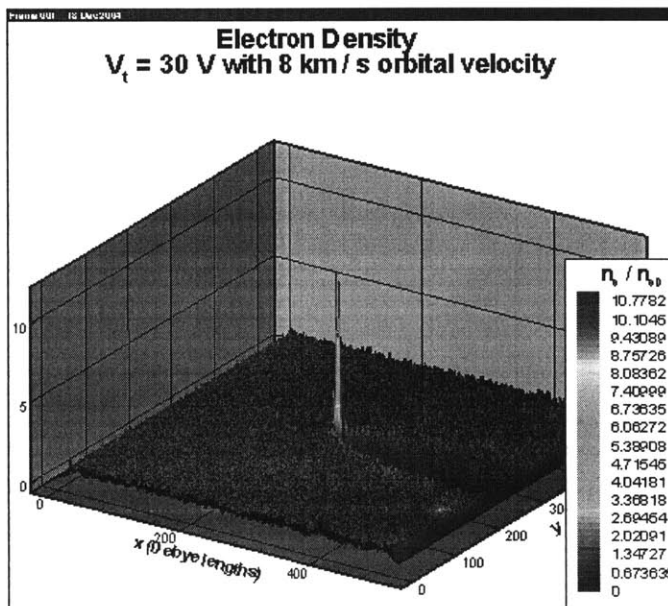


Figure 4-5:

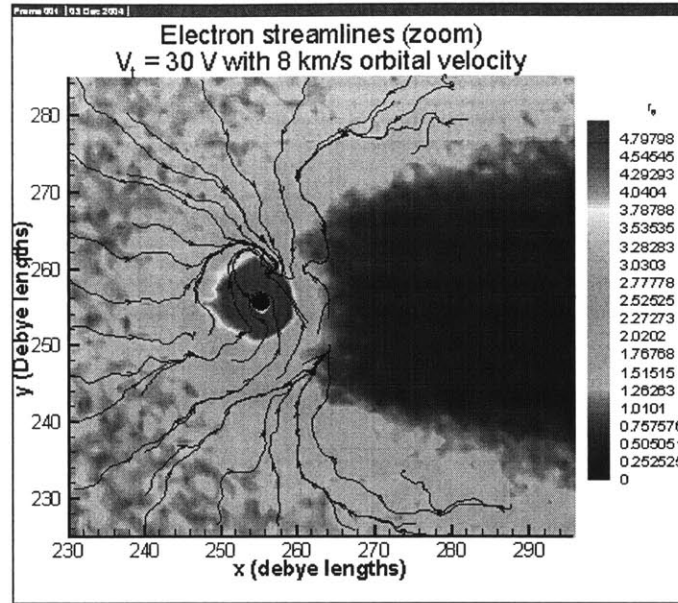


Figure 4-6: close-up: electron density (background) and streamlines

they suggested that the potential wing-shape bumps on the sides of the wake would act as a barrier for electron collection on the wake side, which would reduce then current collection on this side, compared to the OML regime. The balance of these two opposite effects turned out to be a 10% enhancement only. Our results seem more consistent with the previous PIC simulations by [1]Onishi. He observed with a different numerical model an enhancement by a factor 2.4 to 2.6 for biases below 25V (the magnetic field did not seem influential on the collection level). Then, he found surprisingly no enhancement for a higher voltage (100V). This dramatic enhancement breakdown from 25V to 100V might have some numerical reasons. Indeed, for high voltages, the wake near the tether gets wider. Unlike our present model, Onishi could not model large domains and the physics might have been poorly modeled for high voltages, such as 100V, where the characteristic length (width of the wake) is higher.

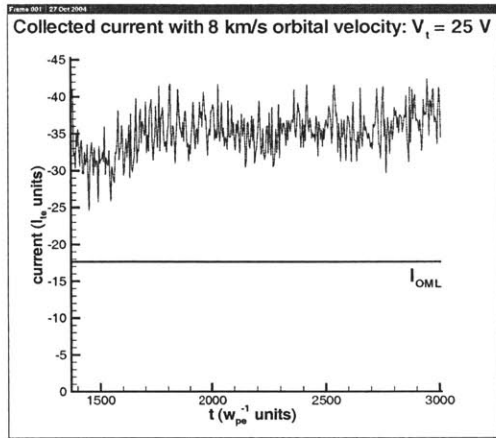


Figure 4-7:

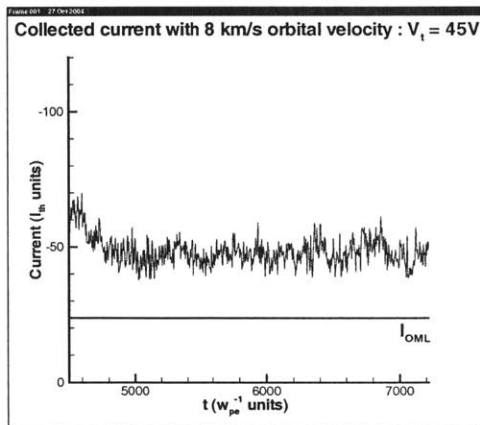


Figure 4-8:

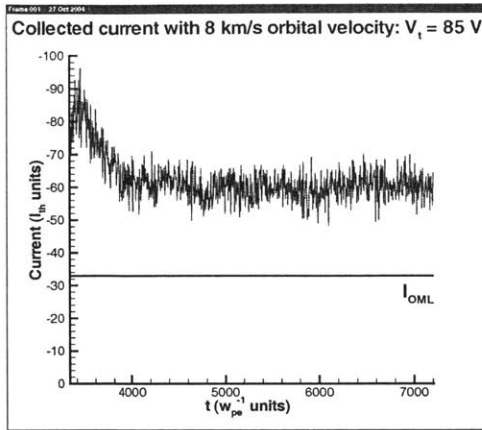


Figure 4-9:

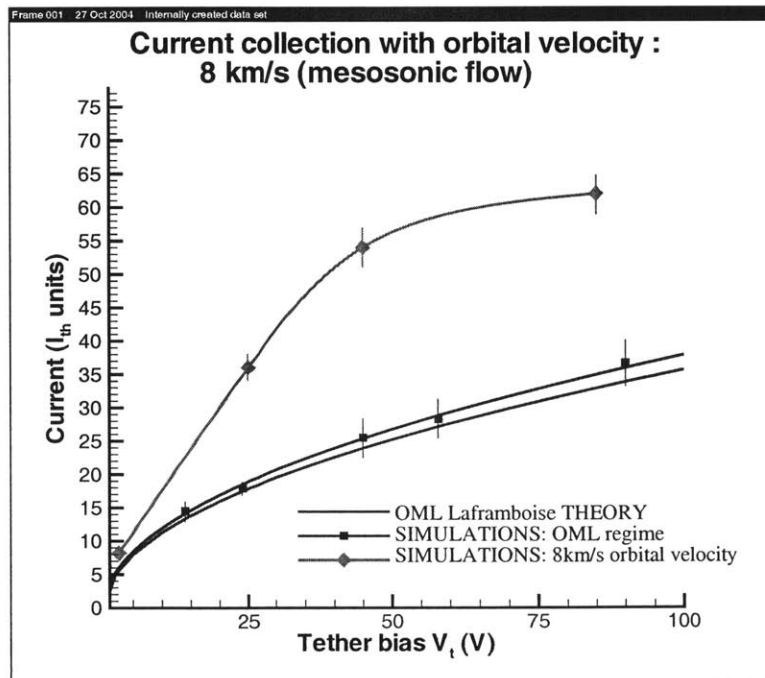


Figure 4-10: The collected current in flow condition (8 km/s) exceeds the OML limit by a factor 2 in the whole relevant bias range. This flow regime (green \diamond) might get closer to the OML (red) for higher biases (around 1000V). The same behaviour at low potential (up to 25V) has been obtained by [1]Onishi (2002).

4.2 Earth's and Self induced magnetic field effects

Our code offers the opportunity to include the uniform Earth's magnetic field and the non-uniform magnetic field induced by a given current flowing in the tether. Such analysis require to run the 3V version of the code, to allow the Larmor motion for particles outside the plane perpendicular to the tether. We ran several cases, but more simulations would be required to handle a parametric study with the following parameters: tether current, Earth's magnetic field, and combined effect with the orbital velocity.

Figures 4-11, 4-12, 4-13, show the plots of particle densities and temperatures in a realistic case, which includes: orbital velocity 8 km/s, tether bias 14V or 45 V, Earth's magnetic field 0.3G, fixed tether current 10A. We chose on purpose a high tether current, in order to emphasize the effects of the self-induced magnetic field, which has been so far neglected in all tether simulations.

First, note that the wake is not symmetric anymore, due to the asymmetry in the magnetic field. We observed some strange behaviours of the wake, which sometimes collapses after hundreds of time steps. Simultaneously, the collected current, which is not zero at the beginning of the run, vanishes. This phenomenon should be further studied, but here is a plausible explanation of what may happen in this configuration: As supported by the observed very high electron density close to the tether (much higher than without self magnetic field), many electrons may get trapped in the separatrix (a few Debye lengths from the probe surface). Figure 2-33 shows indeed how an electron can orbit for a long time inside the separatrix, following the closed magnetic lines. If many electrons actually enter the separatrix but then get tight to the closed magnetic lines, which happens mainly for low potential (with a higher bias, crossing magnetic lines gets easier), a dense confined electron population forms near the probe, as observed in the simulation. These accumulating electrons progressively shield the potential created by the probe. Since the sheath size depends on the shielded potential, the sheath might collapse if the shielding due to the confined electron is too high. In this case, the strong shielding prevents free electrons from reaching the probe, which could explain why the collected current vanishes in the simulation. Moreover, the induced electron confinement and increased density might be reinforced by non-magnetic trapping, as explained in Chapter

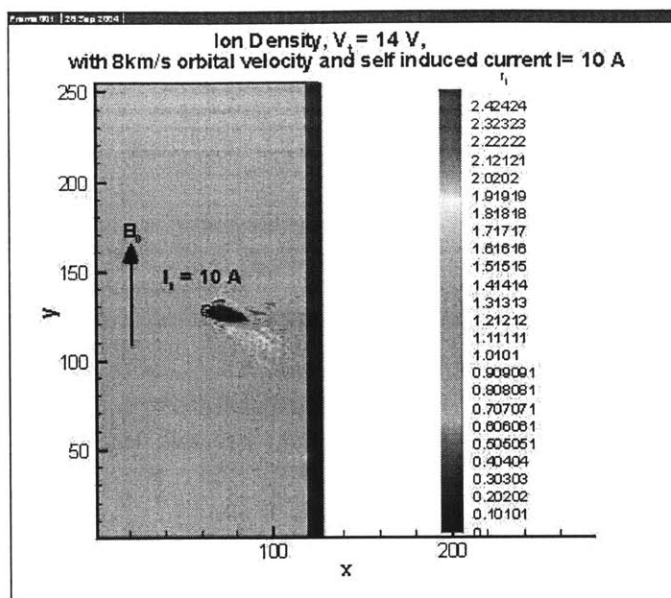


Figure 4-11:

"Particle Trapping".

More simulations should be ran at various potentials to define if this collapsing is actually a physical phenomenon and under which bias and magnetic conditions this regime occurs.

4.3 Tether arrays: interference

Tether array configuration are already of some interest for in-space applications, such as Van-Allen belts remediation. For instance, Choinière and Gilchrist (unpublished) are investigating a circular multiwire configuration to increase the effective sheath size, in order to improve the remediation efficiency. C. Zeihneh and M. Martínez-Sanchez are currently studying a double tether configuration for this problem.

O. Batishchev built a very flexible code, which makes it possible to model several tethers in the domain, and might be used later on to study other tether missions than current collection.

When biased tethers are set close enough one from another, their sheaths may merge, which induces strong interferences between the two probes. Figures 4-15 and 4-16 show some simulation results with two close tether. We chose them close enough such that their sheaths

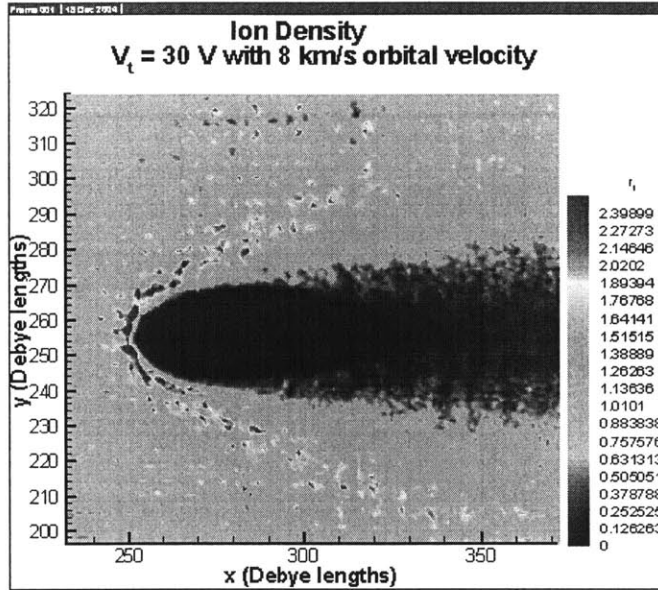


Figure 4-12:

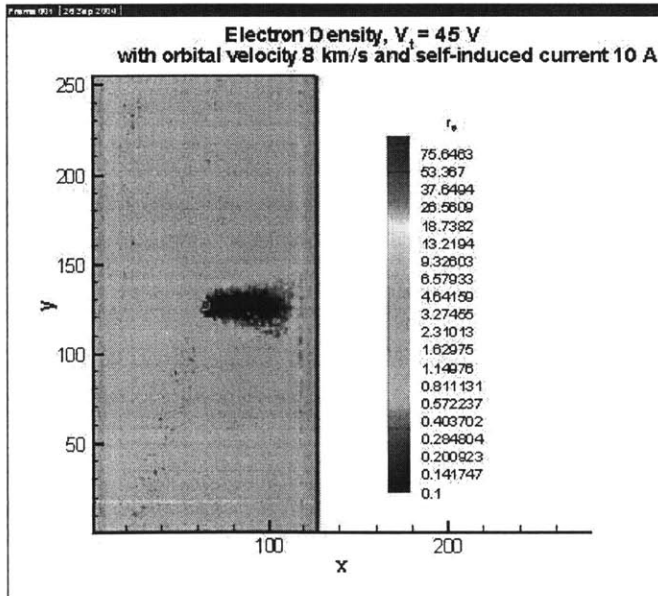


Figure 4-13:

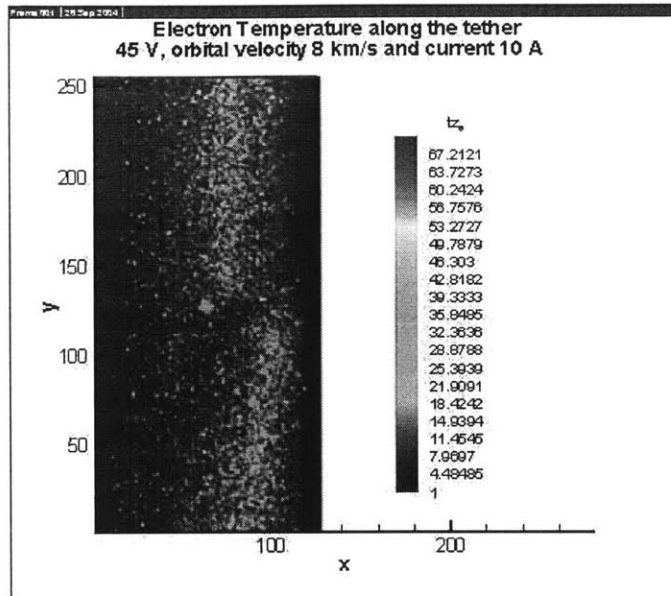


Figure 4-14: Due to the periodic boundary conditions along y , the temperature (here T_z only) increases along the magnetic lines passing close to the tether.

merge. Figure 4-16 shows that both probes collect the same current on the average, but at a lower level than the expected OML limit for a single tether (by 30%, which is already of the order of the predicted current reduction in an extreme interference case according to [22]Sanmartín and Estes(2001).

Unfortunately, we did not focus on this multitether ability of the code. First, it could be useful to study configurations with tethers in contact and compare with the analytical results provided by [22]Sanmartín and Estes(2001). Then, the sheaths properties and collected currents could be studied for any interesting configuration.

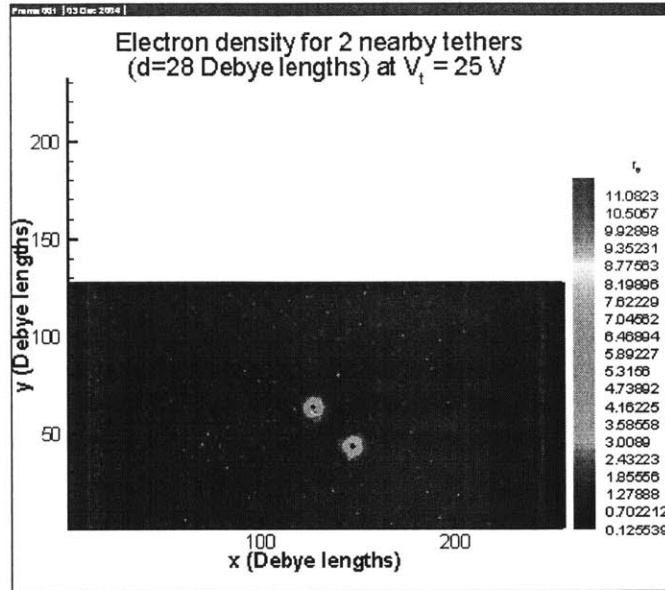


Figure 4-15:

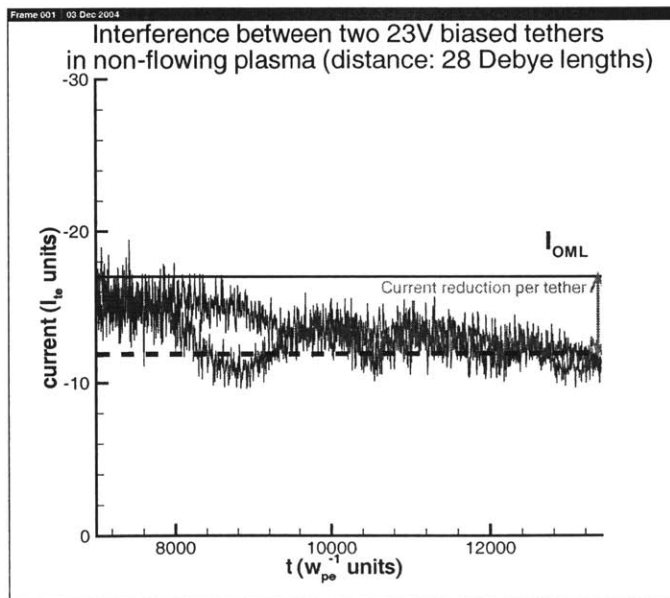


Figure 4-16:

Chapter 5

Particle Trapping

5.1 Definition

In a given potential field, a particle is said to be trapped if its trajectory is bounded.

First, consider the simple case, where a single particle is moving in the field created by a biased probe in vacuum (no plasma, no space charge). For such a Laplacian potential *in the whole space*, created by a charged point or line in vacuum, the trapped population corresponds to *negative energy particles*, which are orbiting around the biased probe. Indeed, in the well known spherical case, corresponding to the Keplerian motion, positive energy trajectories are (unbounded) hyperbolae, whereas negative energy trajectories are ellipses. In the cylindrical case, there is no analytical solution, and negative energy trajectories are not closed anymore. However, they remain bounded, as shown by Figures 2-15 and 2-17.

Therefore, in order for a charged particle to get trapped in such a potential, its total energy, sum of potential and kinetic energy, must be negative. Without a process which would provide this trapped particle with energy, it cannot escape the potential energy well and will never go to infinity. The positively biased tether creates locally a steep potential energy well for electrons. So, if an electron loses energy by any mean, while it wanders in the vicinity of the tether, it will get caught in this well. Then, either the probe captures it, or it follows a bounded orbit around it.

Please note that when the space charge effects due to the plasma are taken into account,

the critical trapping energy might not be zero anymore, as shown in the next sections.

Before the start of the simulation, all particles, organized in beams as explained previously (Figure 3-1), have non-zero positive energy, for their potential energy is still zero, while their kinetic energy is positive. A charged particle in vacuum has constant total energy, but this is not the case anymore in a plasma. In this case, individual particles are not isolated, for they interact with each other by mean of collisions and the time-dependent local space charge which may build up. In our PIC model, all physical collisions (including Coulomb collisions) are neglected, given the size of our simulated domain.

Nonetheless, particle-field interactions might occur if the local electric field fluctuates. Although the energy of the total (isolated) system $\{plasma + field\}$, particles can exchange energy through the unsteady interaction with the local field, creating macroscopic energy exchange.

5.2 Numerical trapping

First, several numerical artifacts of our PIC model systematically trap electrons in the domain:

1. Time resolution

The most important feature to verify is the approximate energy conservation in vacuum. Figures 5-2 and 5-3 show that if the time resolution is poor, the total energy of a particle in vacuum decreases artificially due to our numerical scheme. Choosing a poor time resolution to reduce the computation time might thus create artificially trapped particles. This numerical trapping process could not be disposed of, for it would occur at any time of the simulation. Nonetheless, by choosing a proper multi-scale scheme for particle motion, which allows to adapt the time resolution to the local average speed of the particles), the total energy in vacuum is approximately conserved. With our typical multi-scale scheme, less than 1% variation during the residence time in the sheath was observed for most typical trajectories. This benchmarking prevents us from attributing any higher energy variation to lack of accuracy in particle motion.

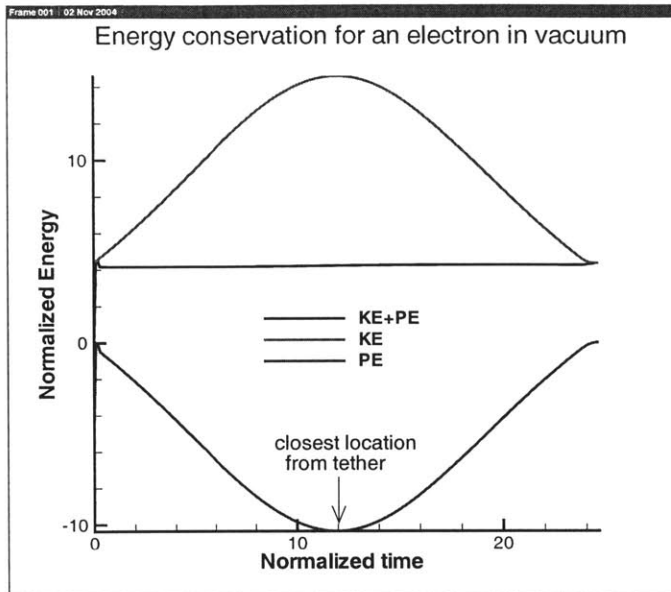


Figure 5-1: Total energy KE+PE is well conserved along a particle trajectory in vacuum under the tether bias influence.

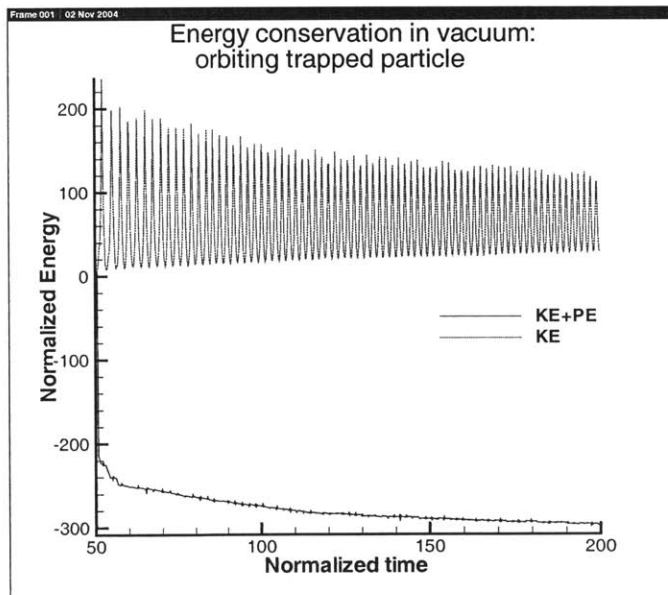


Figure 5-2: For an electron, which is orbiting around a fixed charge in vacuum, our numerical schemes slowly decreases its total energy. Here, $dt=10^{-3}\omega_{pe}^{-1}$ near the tether.

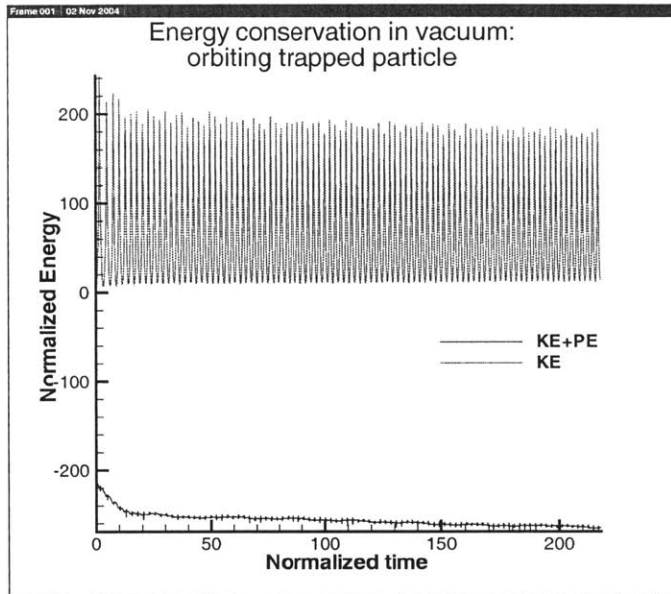


Figure 5-3: When the time resolution is increased, especially close to the tether ($dt=10^{-3}\omega_{pe}^{-1}$), the total energy loss is much slower. The small periodic fluctuations do not depend on the time resolution. They are most probably due to the roughness of the grid near the tether, which does not allow to compute the potential accurately.

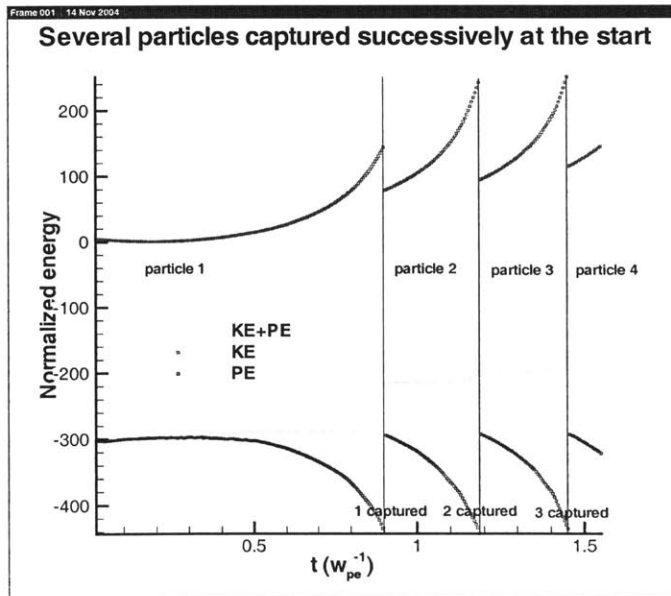


Figure 5-4:

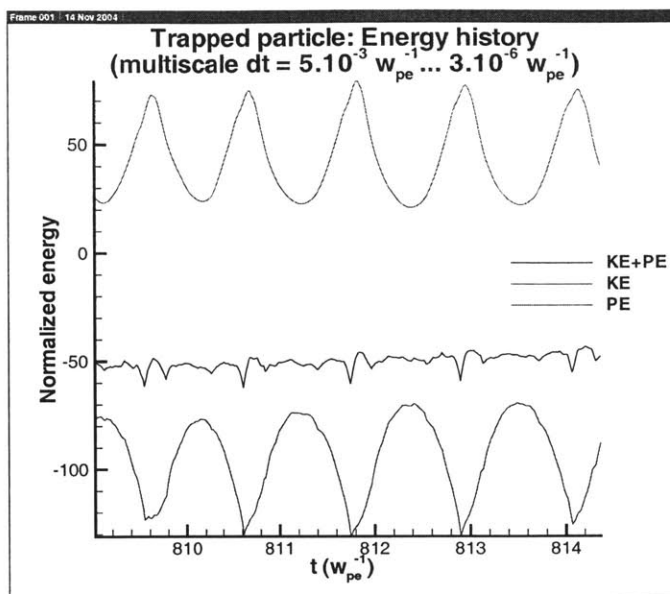


Figure 5-5: For a very high resolution, the energy of any orbiter in the plasma is well conserved over several period. The periodic fluctuations are due to the coarse mesh close to the tether. For particles that are either quickly captured or "passing by" the probe, the energy is conserved to within 1% along their trajectory.

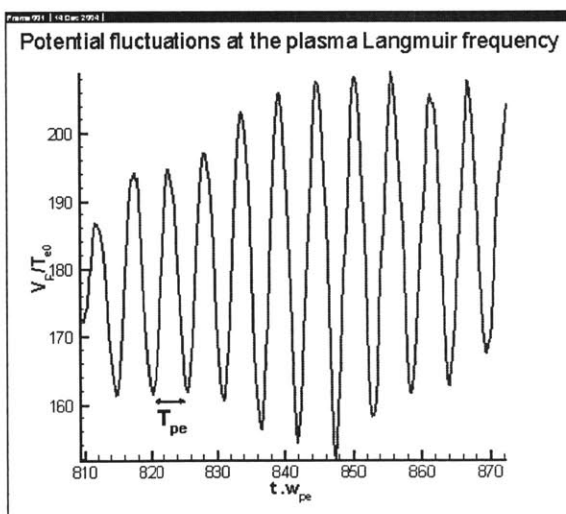


Figure 5-6: Due to the modelling of the tether by a fixed line charge, the tether bias shown above exhibits $\sim 1\%$ oscillations at the electron plasma frequency. This is numerical artefacts due to the finite number of particle per cell.

2. Instant trapping at the start

When the simulation starts, the tether potential is suddenly turned on in a region, where electrons have not been accelerated yet. The sudden potential well which is then created traps right from the start a great part of the electrons in the vicinity of the probe. Since the tether potential has not been shielded yet when the simulation starts, the extent of the initial potential well can be large, trapping particles in a wide zone surrounding the tether. Such a process has already been shown by Ferry[3], with another PIC code. The same phenomenon occurs near the upstream and downstream boundaries, where a similar steep potential may be created at the beginning (Figure 5-11). It would seem natural that all these initially trapped electrons near the probe eventually get captured. However, the trapped population density near the tether remains high in the long term, which suggests another physical process occurring throughout the simulation, which maintains the trapped population in the vicinity of the probe.

In order to test the hypothesis of a trapping due mainly to the initial conditions when the tether potential is turned on, we tried to simulate a quasi-static potential switch on the probe. Instead of setting the line charge in the tether directly at its final value, the line charge amount at the tether was slowly increased from zero to the final expected level. Although the trapping during the switch time decreases when the potential switch gets slower, the trapped population in the vicinity of the tether eventually builds up to the same amount. Also, the same fluctuations of the trapped population with time throughout the domain occur in all cases. After the transient time, particles still lose energy when approaching the tether, maintaining the trapped population permanently near the probe, even if negative energy particles often get captured.

The fluctuating extent of the trapped population in the domain, from a few Debye lengths to the tether to the entire domain (cf. Figures 5-7 to 5-10, at the successive times t_1 to t_4) can be explained by two phenomena :

- These negative energy particles might sometimes get out of close vicinity of the tether, due to electric and density fluctuations, and thus spread the trapped population farther from the probe.

- But the main reason of these fluctuations seems to be direct local potential fluctuations, which can induce jumps of a particle potential energy $PE = q\Phi$, whereas the kinetic energy evolves smoothly. As a consequence, its total energy $KE + PE$ may jump back and forth from positive to negative value. Although such particles are plotted as trapped particles, because their energy is momentarily negative, they *cannot be considered as actually trapped* in the long term. This effect is a consequence of our boundary conditions, especially at the tether surface, where the potential is not rigorously constant (a fixed charge is set at the tether center). When averaging the trapped density over time, these fluctuations appear as a "noise" (time-averaged 15-30% of $E < 0$ particles in the whole domain, which are not really trapped).

5.3 Physical trapping processes

5.3.1 Collisional

Collisional trapping has been studied by [[35]][[36]][[37]]Lampe et al. in the case of ions in dusty plasmas. They analyzed how charge exchange collisions between slow neutrals and fast ions (accelerated by the negatively biased dust grain) may create ion trapping around a small grain at floating potential. Their interest might seem quite different from ours, since they concentrate on ion and not electron trapping, by low negatively biased (negative floating potential) spherical dust grains. Charge exchange (inelastic) collisions are a clear physical process which removes an energetic ion and creates a new ion, with low energy, which may be trapped by the grain. No similar phenomenon exists for ionospheric electrons, whose collisions with other electrons, neutrals and ions have frequencies in the same order of magnitude and *do not necessarily reduce* the electron energy.

[[35]][[36]][[37]]Lampe et al. obtain the following interesting result: The trapped population density around a small grain ($< \lambda_{D_e}$) is usually much higher than the background plasma

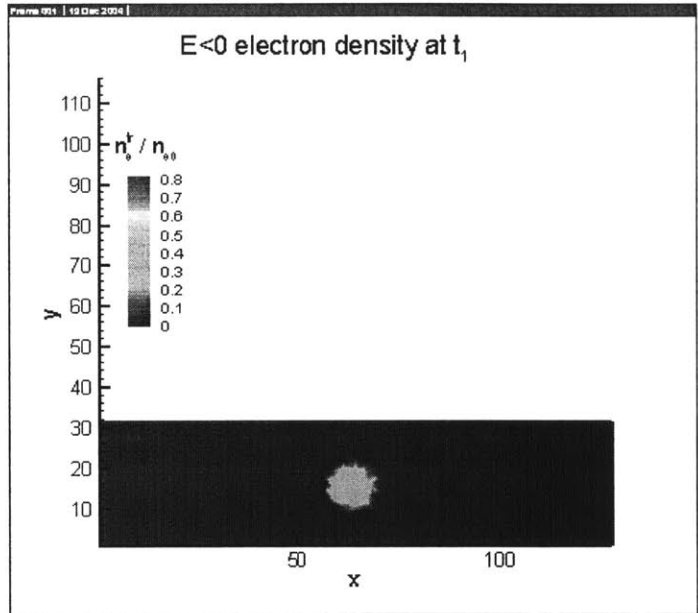


Figure 5-7:

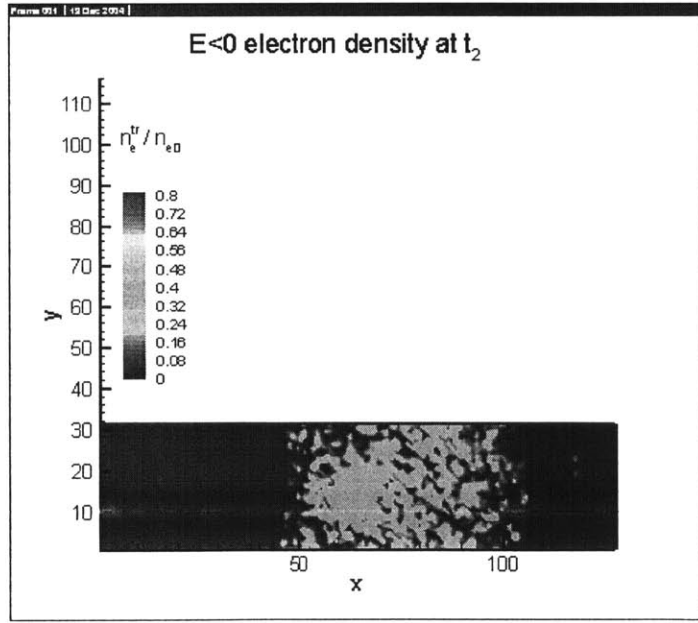


Figure 5-8:

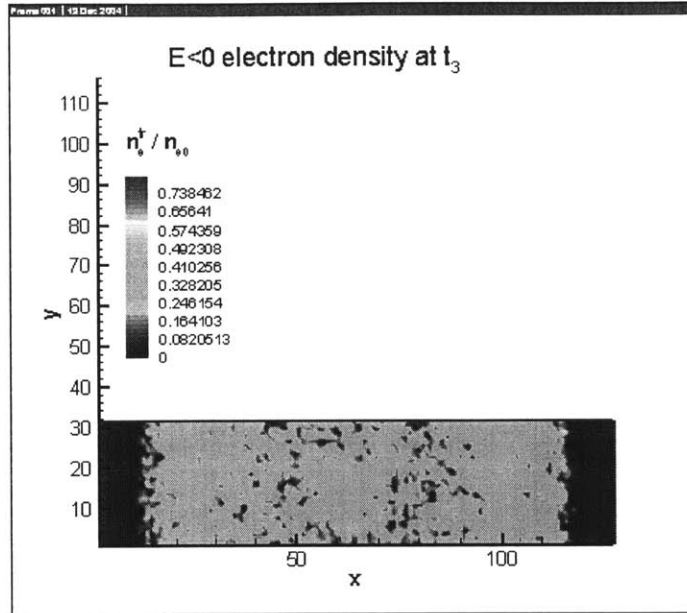


Figure 5-9:

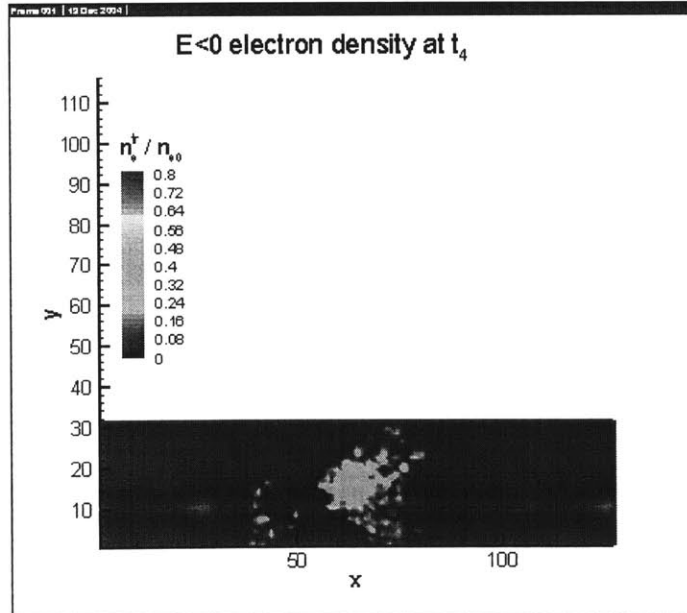


Figure 5-10:

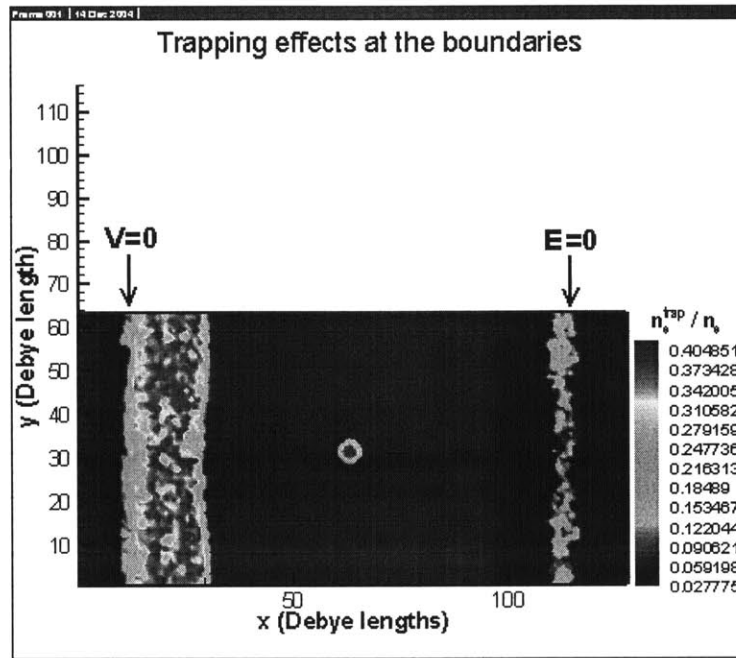


Figure 5-11: Boundary conditions may affect electron trapping. Although the Dirichlet boundary condition $V = 0$ is more natural for the no-flow case, it induces a fluctuating stiff potential slope, which periodically decreases the energy below 0 for some slow electrons at the boundaries.

density, and does not depend on the collision frequency (providing it is independent of the particle energies). This means that even for extremely rare collisions, a trapped population builds up around the grain. Of course, the trapped particle flux into the grain is proportional to the collision frequency.

Actually, an extrapolation of their work, relevant to our topic, would be the following: if there is a non-conservative physical phenomenon which drives both trapping (energy drop near the grain/probe) and detrapping (energy increase or scattering of orbiters into the object) in proportion, as it is the case for charge exchange collisions, then non-negligible trapping may occur around the object, even if the corresponding phenomenon is very slow.

5.3.2 Collisionless adiabatic

In quasi-collisionless plasmas, like the ionosphere, a relevant non-conservative effect which would induce particle energy variations, could be the existence of non-stationary electric fields, rather than inelastic collisions.

In non-stationary fields, the particle energy is no conserved, such that free electrons can be trapped into bounded orbits. The effect of a slowly varying potential hump on electrons has been investigated by [[34]]Gurevich(1968), in order to model non-linear plasma-waves interactions at the early stages of Landau damping understanding. When a potential hump, such as the one created by a positively biased tether, is slightly non-stationary with respect to the electrons, varying much more slowly than their thermal motion, electrons can be captured without any collisions. This collisionless trapping has been called adiabatic trapping and yields the following result for the trapped population density in the 1D-case:

$$\frac{n_{etr}(r)}{n_{e0}} = \sqrt{\frac{2}{m_e}} \int_{-e\Phi(r)}^{-e\Phi_{\min}} \frac{f_{tr}(E) dE}{\sqrt{E + e\Phi(r)}}; \quad (5.1)$$

The adiabatic condition implies that the field varies only slightly during the period of finite motion (bounded orbit $[x_1; x_2]$) for a trapped particle. Under these conditions, the integral:

$$I(t, E) = \frac{1}{2\pi} \times 2 \int_{x_1}^{x_2} \sqrt{2m_e(E - e\Phi(x))} \quad (5.2)$$

is conserved along the orbit. Gurevich calls it thus the adiabatic invariant, or (following Landau and Lifshitz) "action integral", which is as an integral of motion. The trapped particle distribution, solution of the time-averaged Vlasov equation for these electrons (cf. complete derivation in the next subsection for the 2D case), which cannot be described by a Maxwellian (unlike the untrapped particle distribution), may be conveniently expressed as a function of I :

$$f_{tr}(t, E) = f_{tr}(I(t, E)). \quad (5.3)$$

Assuming that the distribution function for the entire (trapped and untrapped population) must be continuous at all E (which is the case if the field has been applied slowly), we can conclude that the trapped electron distribution everywhere in the potential hump is determined by the value of the non-trapped electron distribution at the edge of the hump:

$$f_{tr}(t, E) = f_{ntr}(e\Phi_{\min}). \quad (5.4)$$

where $f_{ntr}(E) = \sqrt{\frac{m_e}{2\pi T_{e0}}} \exp\left(-\frac{E}{kT_{e0}}\right)$ is the non-trapped population (Maxwellian) energy distribution and Φ_{\min} is the potential value at the edge of the hump, separating untrapped and trapped electrons (Figure 5-12). $e\Phi_p - e\Phi_{\min}$ is then the depth of the potential energy well. This case would apply for instance for the trapped electron population in the sheath created by a positively biased wall at fixed potential Φ_p . If the potential profile is monotonic as it is usually the case for a sheath, $\Phi_{\min} = \Phi(\text{sheath edge}) \ll \Phi_p$ for high bias $\frac{e\Phi_p}{kT_{e0}} \gg 1$. We can then take $\Phi_{\min} = 0$, which means that only negative energy electrons are trapped. The trapping would occur then if the sheath expands, even if Φ_p remains constant.

Note that, unlike the untrapped population, the trapped electrons distribution is not Maxwellian at all, but uniformly distributed in energy space. The amount of trapped electrons in steady state does not depend on the actual potential variation history, as long as it is slow enough. Indeed, the trapped population is determined by the untrapped population at the edge of the potential hump and by the local potential. The dependence of Ne_{tr} on $\Phi(r)$ shows that the concentration of trapped particles increases with the height of the potential hump, but no more than $\propto \sqrt{\frac{e\Phi_p}{kT_{e0}}}$. However, in the case of a high bias $\frac{e\Phi_p}{kT_{e0}} \gg 1$, the trapped population can be greater than the untrapped one by orders of magnitude. The slow adiabatic variation of the

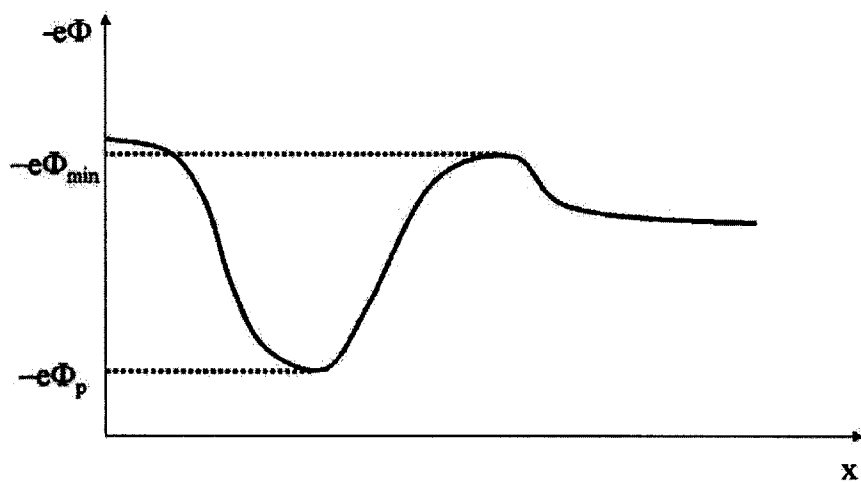


Figure 5-12: When a 1D potential hump forms (potential energy well for electrons), particles with an energy lower than the lowest edge of the well cannot escape

potential with respect to the plasma occurs of course when the plasma is flowing subsonically for electrons, as it is the case for an orbiting tether. It may also occur when the potential is turned on, for the sheath expansion corresponds to the ion motion, which is much slower than the electron thermal velocity.

Therefore, these qualitative results regarding the trapped population in the sheath are very similar for both collisional and collisionless adiabatic trapping. Indeed, although the physical trapping process is different in each case, both result in a steady state which does not depend on the characteristic time scale of the trapping mechanism: the collision period $\frac{1}{\nu}$ or the potential motion time scale $\left| \frac{\Phi_p}{d\Phi/dt} \right|$. In both cases, the trapped population concentration increases with the bias Φ_p creating the sheath, and is typically much higher than the background density for untrapped electrons. Regardless of the physical trapping mechanism, electron trapping in sheath seems almost never negligible, and should be taken into account in order to improve sheath physics understanding. In the case of electrodynamic tethers, the accumulation of trapped electrons in the sheath and presheath may change the current collection by two mechanisms:

- Capture of trapped particles by the probe surface, resulting in collection overshoot.
- Additional shielding of the potential created by the probe, resulting in collection reduction, for example if the potential topology does not satisfy the OML condition (Equation 1.26) anymore.

How these two countervailing effects balance each other might depend on the external background conditions: Tether bias Φ_p , orbital velocity V_{orb} or RAM energy, Earth's magnetic field \vec{B}_0 and self-induced magnetic field \vec{B}_s .

5.4 Do all trapped particles have negative energy?

In the two-dimensional case, such as a positively biased wire, creating a cylindrical potential hump, the azimuthal motion brings some complexity in the analysis. In the 1D-case, the equation of motion has only one time-independent integral (when the potential is constant), the

electron energy E . In the 2D-axisymmetric case, both the energy E and the angular momentum J are conserved along particle trajectories for a constant potential. Instead of the mere potential energy, the effective energy of Equation 1.28, including angular momentum effects, must be used to study potential barriers effects on electron trapping. The rotational kinetic energy plays the role of an effective potential energy, which may act as a potential barrier for the radial motion. Electrons with a high angular momentum feel a strong centrifugal force, which can help them climb out of the potential energy well created by the probe. High rotational energy can prevent an electron from getting trapped in the sheath by the positively biased tether.

For the sake of simplicity, we shall neglect space charge shielding in the sheath and assume a Laplacian potential in the sheath, and assume quasineutrality outside, which yields $\Phi(r) \propto \frac{1}{r}$ outside the sheath.

$$\Phi(r) = \Phi_p \frac{\ln R_s - \ln r}{\ln R_s - \ln R} + \Phi(R_s), \forall r \leq R_s \quad (5.5)$$

$$\Phi(r) = \Phi(R_s) \frac{R_s}{r}, \forall r > R_s \quad (5.6)$$

For high biases, $\frac{\Phi_p}{\Phi(R_s)} \gg 1$, we can take $\Phi(R_s) = 0$. Remember that the accurate dependence of R_s on Φ_p is given by Equation 1.11.

The effective potential can then be written:

$$U_{eff}^J(r) = -\Phi_p \frac{\ln R_s - \ln r}{\ln R_s - \ln R} + \frac{J^2}{2em_e r^2}. \quad (5.7)$$

We find easily:

$$\frac{dU_{eff}^J(r)}{dr} = \frac{\Phi_p}{\ln R_s - \ln R} \frac{1}{r} - \frac{J^2}{em_e r^3}. \quad (5.8)$$

So, U_{eff} has a minimum at $r_{min}^J = \sqrt{\frac{J^2}{em_e \Phi_p} \ln \frac{R_s}{R}}$. Values at $r = R$, r_{min} and R_s can be easily calculated as well:

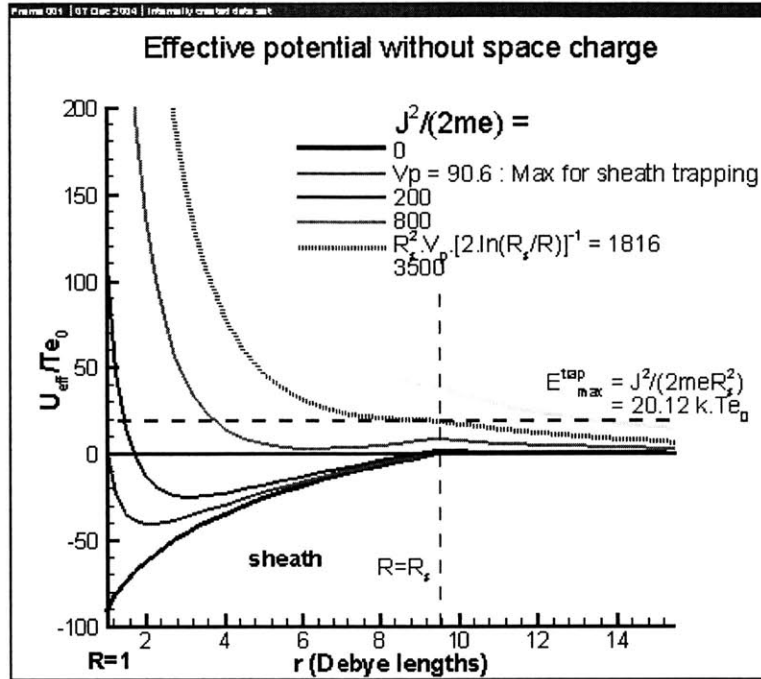


Figure 5-13: Effective potential with a bias $\frac{e\Phi_p}{kT_{e0}} = 90.6$ and $\frac{R}{\lambda_{De}} = 1$, for several angular momenta J . A Laplacian model of $\Phi(r)$ is used in the sheath, by neglecting the space charge.

$$U_{eff}^J(R) = -\Phi_p + \frac{J^2}{2em_e R^2}, \quad (5.9)$$

$$U_{eff}^J(r_{min}^J) = \Phi_p \left[\frac{1}{2 \ln \frac{R_s}{R}} - \frac{\ln R_s - \ln \sqrt{\frac{J^2}{em_e \Phi_p} \ln \frac{R_s}{R}}}{\ln R_s - \ln R} \right] \quad (5.10)$$

$$U_{eff}^J(R_s) = \frac{J^2}{2em_e R_s^2} \quad (5.11)$$

Figure 5-13 shows a plot of $U_{eff}^J(r)$ gathering all this information. In order to figure out how this effective potential acts on an electron with energy E , one should draw the horizontal line $U_{eff} = \frac{E}{e}$ on this graph. The smallest radius at which the line crosses the curve U_{eff}^J , where J is the angular momentum of this electron gives the smallest radius the electron can reach. Once a E, J electron gets to this point, its rotational energy is too high to allow it to get any closer

to the probe and it necessarily "bounces back" (r increases), up to the higher radius where the line crosses the U_{eff}^J curve. This second intersection exists if and only if $r_{\min}^J < R_s$. In this case, the electron feels a potential barrier there, preventing it from leaving the sheath, because its centrifugal energy cannot balance the attracting tether bias. the electron then "bounces back" towards the probe, etc. Therefore, the effective potential acts as a well for electrons if $r_{\min}^J < R_s$.

If $r_{\min}^J \geq R_s$, the effective potential is actually monotonically decreasing inside the sheath, and does not act as a well anymore [Note that there could still be a shallow well in the presheath, which can be studied by a more accurate potential modelling of this region (Sanmartín, unpublished)]. Once the E, J electron is repelled by the effective centrifugal barrier near the tether, nothing prevents it from going to infinity. This happens for:

$$J^2 \geq (J_{tr}^{\max})^2 = \frac{em_e R_s^2 \Phi_p}{\ln R_s - \ln R}, \quad (5.12)$$

which allows to calculate the maximum energy of any electron which would be trapped in the sheath:

$$E_{tr}^{\max} = eU_{eff}^{J_{tr}^{\max}}(R_s); \quad (5.13)$$

$$E_{tr}^{\max} = \frac{1}{2(\ln R_s - \ln R)} e\Phi_p > 0. \quad (5.14)$$

Unlike the 1D case, where $E_{tr}^{\max} = e\Phi(R_s) \simeq 0$, E_{tr}^{\max} is here strictly positive and is significantly higher than the thermal energy for a high bias. This means that not only negative, but positive energy electrons as well, can get trapped in the sheath surrounding a positively biased cylindrical tether.

We can now push further these calculations in order to get the trapped population concentration in the sheath. Sanmartín (unpublished) rewrote Gurevich's study of adiabatic trapping in the 2D axisymmetric case:

Considering a time dependent potential, the Vlasov equation for the trapped population distribution is:

$$\frac{\partial f_{tr}}{\partial t} dt + \frac{\partial f_{tr}}{\partial E} dE + \frac{\partial f_{tr}}{\partial J} dJ = 0, \quad (5.15)$$

where:

$$dE = \left[\frac{\partial E}{\partial t} + v_r \frac{\partial E}{\partial r} + \left(\frac{v_\theta^2}{r} + \frac{e}{m_e} \frac{\partial \Phi}{\partial t} \right) \frac{\partial E}{\partial v_r} - \frac{v_r v_\theta}{r} \frac{\partial E}{\partial v_\theta} \right] dt = \frac{\partial E}{\partial t} dt; \quad (5.16)$$

$$dJ = \left(v_r \frac{\partial J}{\partial r} - \frac{v_r v_\theta}{r} \frac{\partial J}{\partial v_\theta} \right) dt = 0, \quad (5.17)$$

for E only depends on the potential time dependence, with $\frac{\partial E}{\partial t} = -e \frac{\partial \Phi}{\partial t}$ and J is conserved.

The Vlasov equation is then simply:

$$\frac{\partial f_{tr}}{\partial t} - e \frac{\partial \Phi}{\partial t} \frac{\partial f_{tr}}{\partial E} = 0 \quad (5.18)$$

If the potential is changing slowly with respect to the electrons (adiabatic approximation), we can regard the potential as fixed during one oscillation period τ of a trapped electron . Then, f_{tr} varies very little over one period τ . Integrating over one period τ , along an orbit which oscillates between r_1 and r_2 , yields:

$$\frac{\partial f_{tr}}{\partial t} + \left\langle -e \frac{\partial \Phi}{\partial t} \right\rangle_\tau \frac{\partial f_{tr}}{\partial E} = 0. \quad (5.19)$$

We can write:

$$\left\langle -e \frac{\partial \Phi}{\partial t} \right\rangle_\tau = \frac{\int_0^\tau -e \frac{\partial \Phi}{\partial t} dt}{\int_0^\tau dt}, \quad (5.20)$$

$$\text{with } dt = \frac{dr}{v_r} = \frac{dr}{\sqrt{E + e\Phi(r) - \frac{J^2}{2em_e r^2}}} = \frac{dr}{\sqrt{E - U_{eff}^J(r)}}, \quad (5.21)$$

which allows us to find an adiabatic invariant for the motion, as [34]Gurevich(1968) did in the 1D case. Define the "action integral":

$$I(E, t, J) = \int_{r_1}^{r_2} v_r dr \quad (5.22)$$

$$I(E, t, J) = \int_{r_1}^{r_2} \sqrt{E + e\Phi(r) - \frac{J^2}{2em_e r^2}} dr. \quad (5.23)$$

We have then:

$$dI = \frac{\partial I}{\partial t} dt + \frac{\partial I}{\partial E} dE + \frac{\partial I}{\partial J} dJ + \frac{\partial I}{\partial r_1} dr_1 + \frac{\partial I}{\partial r_2} dr_2, \quad (5.24)$$

where $dJ = 0$, $\frac{\partial I}{\partial r_1} = -v_r(r_1) = 0$ and $\frac{\partial I}{\partial r_2} = v_r(r_2) = 0$.

Therefore, we get the time evolution of I :

$$\frac{dI}{dt} = \int_{r_1}^{r_2} \frac{\frac{dE}{dt} - e \left(\frac{\partial \Phi}{\partial t} \right)_r dr}{2\sqrt{E + e\Phi - \frac{J^2}{2em_e r^2}}}. \quad (5.25)$$

Since $\frac{dE}{dt} - e \left(\frac{\partial \Phi}{\partial t} \right)_r = 0$ along each particle's trajectory, this yields eventually:

$$\frac{dI}{dt} = 0. \quad (5.26)$$

Thus, the solution of the trapped population Vlasov equation 5.19 is:

$$f_{tr}(t, E, J) = f_{tr}(I(t, E, J)) \quad (5.27)$$

For an electron of angular momentum J , the limiting energy between an unbounded and a bounded orbit actually depends on J , as may be seen from Figure 5-13. Within our simplified potential model, the maximum energy of an electron which is trapped in the sheath with an angular momentum J is indeed :

$$E_{tr}^{\max, J} = eU_{eff}^J(R_s) = \frac{J^2}{2m_e R_s^2}, \quad (5.28)$$

If we follow here Gurevich and assume that the distribution function is continuous at $E = E_{tr}^{\max, J}$ for all angular momenta J , we can conclude that :

$$f_{tr}(t, E, J) = f_{ntr}\left(E_{tr}^{\max, J}\right). \quad (5.29)$$

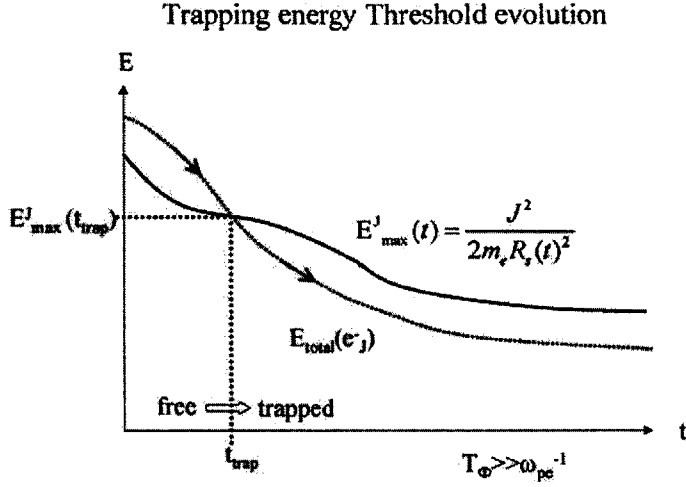


Figure 5-14: During the initial transient, the sheath expands, so the maximum energy of trapped J electrons decreases. The continuity of the trapped distribution with the untrapped one should be taken at the separating value at the trapping time: $E_{tr}^{\max,J}(t_{trap})$.

Note that rigorously $E_{tr}^{\max,J}$ depends on t because R_s^2 increases slowly during the transient time, when the tether power is switched on. More accurately, the boundary condition:

$$f_{tr}(t, E, J) = f_{ntr}\left(E_{tr}^{\max,J}(t_{trap})\right). \quad (5.30)$$

should be used, where $E_{tr}^{\max,J}(t_{trap})$ is the separating energy at the time t_{trap} when the electrons with energy E now (at infinite time) got trapped. Unlike the particle energy, the angular momentum is conserved throughout the adiabatic potential motion. Figure 5-14 shows how the energy boundary between trapped and untrapped might evolve with time, and when an electron gets captured in the sheath.

Appendix IV shows how the sheath radius $R_s(t_{trap})$ can be obtained, at the time t_{trap} , when a given electron (of energy E and angular momentum J at the present time) got trapped. The dependence of $R_s(t_{trap})$ on E and J , which vary within the electron population, yields a

complicated result for $E_{tr}^{\max,J}(t_{trap}) = \frac{J^2}{2m_e R_s(t_{trap})^2}$. If the variations of $R_s(t)$ during the adiabatic change of the potential are taken into account, it becomes impossible to get a simple integral formula for the trapped density. So, in order to keep most calculations analytical, we made the assumption:

$$R_s(t_{trap}) \simeq R_s(t = \infty), \forall (E, J), \quad (5.31)$$

which means that we consider that the limiting energy for trapping is the same for all electrons of angular momentum J , which is actually false, since these electrons were trapped at different times t_{trap} , depending on their present energy E . This strong assumption allows us to pursue the analysis, without solving a complex integral, with implicit boundaries. Appendix IV suggests why this assumption may not change much the numerical results.

This equality holds right at the sheath boundary with a Laplacian model in the sheath, where all electrons had a Maxwellian distribution before the potential was turned on. This initial condition is:

$$f_{ntr}(E_{tr}^{\max,J}) = f^\infty(E_{tr}^{\max,J}) \quad (5.32)$$

and eventually, under the approximation 5.31:

$$f_{tr}(t, E, J) = f^\infty(E_{tr}^{\max,J}) = \sqrt{\frac{m_e}{2\pi T_{e0}}} \exp\left(-\frac{J^2}{2m_e R_s^2 k T_{e0}}\right). \quad (5.33)$$

Unlike the non-trapped population, the trapped electron distribution in the sheath does not depend on the particle energy, but on their angular momentum J . Following Sanmartín's calculations for the non-trapped population (Equation 1.20), the trapped population density can be written as an integral in (E, J) space, with the following form:

$$\frac{n_{e_{tr}}(r)}{n_\infty} = \iint \frac{\exp\left(-\frac{J^2}{2m_e R_s^2 k T_{e0}}\right) dE dJ}{2\pi k T_{e0} \sqrt{J_r^2(E) - J^2}}. \quad (5.34)$$

In order to compute this integral, the integration boundaries have to be defined properly in (E, J) space. First, we can reduce the integration domain to $J \geq 0$, by substituting J by dJ :

$$\frac{n_{etr}(r)}{n_\infty} = \int_E \int_{J \geq 0} \frac{\exp\left(-\frac{J^2}{2m_e R_s^2 k T_{e0}}\right) dE dJ}{\pi k T_{e0} \sqrt{J_r^2(E) - J^2}}. \quad (5.35)$$

As discussed above, any (E, J) electron can exist and be trapped if and only if:

1. $E - \frac{J^2}{2m_e r^2} + e\Phi(r) = \frac{1}{2}m_e v_r^2 \geq 0$. This condition imposes that the radial kinetic energy must be positive. In this case, $J_r^2(E) - J^2 \geq 0$ and the integral is well-defined;
 2. $E < E_{tr}^{\max, J} = \frac{J^2}{2m_e R_s^2}$, which is the limiting energy between bounded and unbounded orbits. Note that here, $R_s(t_\infty)$ indeed must be used and not $R_s(t_{trap})$, unlike the exponential factor in Equation 5.35.
 3. $J < J_{tr}^{\max} = \sqrt{\frac{em_e R_s^2 \Phi_p}{\ln R_s - \ln R}}$, because at higher angular momentum, the repelling centrifugal force is always stronger than the attracting potential;
 4. $J > J_R^*(E)$, because electrons in the range: $0 \leq J \leq J_R^*(E)$ will be captured by the probe (cf. Figure 5-15, so they cannot be considered as permanently trapped "orbiters".
- In the OML regime, this condition yields simply:

$$J > J_R(E) = \sqrt{2m_e R^2 (E + e\Phi_p)} \quad (5.36)$$

We could have mentioned another boundary, which states that the energy at a given J cannot be lower than $\min_{R < r < R_s} [U_{eff}^J(R_s)]$. However, this condition is always verified when condition 1 is. Indeed, if the radial energy vanishes (limit for condition 1), some rotational kinetic energy remains, and the total energy is therefore greater than its minimum for a give J (similar remarks are made later on for condition 3, which can be ignored as well).

Note that, with the simplified boundary condition $\Phi(R_s) = 0$, the regime is not exactly OML, since

$$J_R(E)^* = \sqrt{2m_e R_s^2 E} < J_R(E) = \sqrt{2m_e R^2 (E + e\Phi_p)}, \forall E < \frac{R^2}{R_s^2 - R^2} e\Phi_p \quad (5.37)$$

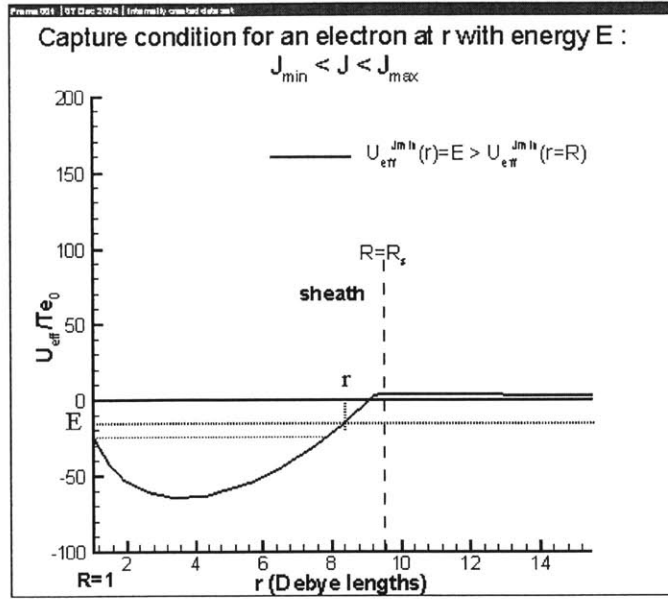


Figure 5-15: An electron at location r in the sheath and with energy E will be captured by the tether if the U_{eff}^J curve which crosses (r, E) goes below E at the probe surface $r = R$

This value typically is $\frac{R^2}{R_s^2 - R^2} \Phi_p \sim a \text{ few } kT_{e0}$. The error associated with the approximation of the potential by a Laplacian being at least of the same order, we still use the OML condition, which is actually verified by the actual potential, according to Figure 3-8.

These four conditions, with the additional constraint $J > 0$, define a bounded integration domain in (E, J) space, which is represented in Figure 5-17. Note that the integration is not straightforward, because three of the four boundaries are neither vertical nor horizontal lines in the integration space. Only the boundary $J < J_{tr}^{max} = \sqrt{\frac{em_e R_s^2 \Phi_p}{\ln R_s - \ln R}}$ is actually of this kind, but we show below that it lies outside the integration domain. The three remaining boundaries are obviously parabolas. If plotted in (J^2, E) coordinates, they become straight lines, as done by [25]Sanmartín. With J (or J^2) on the horizontal axis and E on the vertical, the curve 2 increases more slowly than the curve 1, which increases more slowly than the curve 4. Indeed, their coefficient verify :

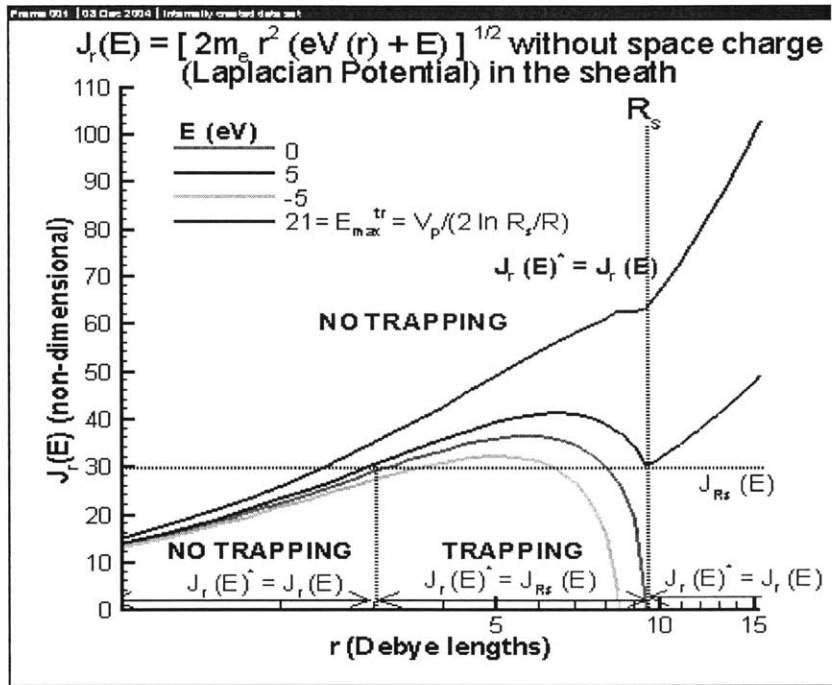


Figure 5-16: $J_r(E)$ plots for a Laplacian Potential ($\frac{e\Phi_p}{kT_{e0}} = 91$) in the sheath around a $1\lambda_{De}$ radius probe. Note that for the choice, $\Phi(R_s) = 0$, the OML conditions are not exactly verified, since $J_R(0)^* < J_R(0)$. Trapping occurs for some J if $J_r(E)^* < J_r(E)$, which never happens above some energy E_{\max}^{tr} . The trapping zone is represented for $E = 5eV$.

$$\frac{a_2}{a_1} = \frac{R^2}{r^2} < 1; \quad (5.38)$$

$$\frac{a_1}{a_4} = \frac{r^2}{R_s^2} < 1. \quad (5.39)$$

Since the curves 4 and 1 take respectively the value $E = -e\Phi_p$ and $E = -e\Phi(r)$ at $J = 0$, the curve 4 lies under the curve 1 at low J they lie under the curve 2 at low J and then cross it, since their growing coefficients are higher. The intersections occur respectively at:

$$J_{12}^2 = \frac{2em_e\Phi(r)}{1/r^2 - 1/R_s^2}; \quad (5.40)$$

$$J_{14}^2 = \frac{2em_e[\Phi_p - \Phi(r)]}{1/R^2 - 1/r^2}; \quad (5.41)$$

$$J_{24}^2 = \frac{2em_e\Phi_p}{1/R^2 - 1/R_s^2}. \quad (5.42)$$

They verify the following:

$$J_{12} = J_{tr}^{\max} \times \sqrt{\frac{2 \ln(R_s/r)}{(R_s/r)^2 - 1}} \leq J_{tr}^{\max} \quad (5.43)$$

$$J_{24} = J_{14} \times \sqrt{\frac{\Phi_p}{\Phi_p - \Phi(r)}} \times \sqrt{\frac{1 - R^2/r^2}{1 - R^2/R_s^2}} \geq J_{14}; \quad (5.44)$$

These order relations are valid for any parameters Φ_p and R_s . Given the fact that the curves are parabolas (or straight lines in the (J^2, E) plane), they imply: $J_{24} \leq J_{12}$ as well, which finally yields :

$$J_{14} \leq J_{24} \leq J_{12} \leq J_{tr}^{\max} \quad (5.45)$$

The integration domain is then the area delimited by the three curves 1, 2 and 4 (cf. Figure 5-17). The cut by the vertical line 3, which defines the maximum J allowed for a particle to be trapped, acts anyway out of this domain, just like the additional condition

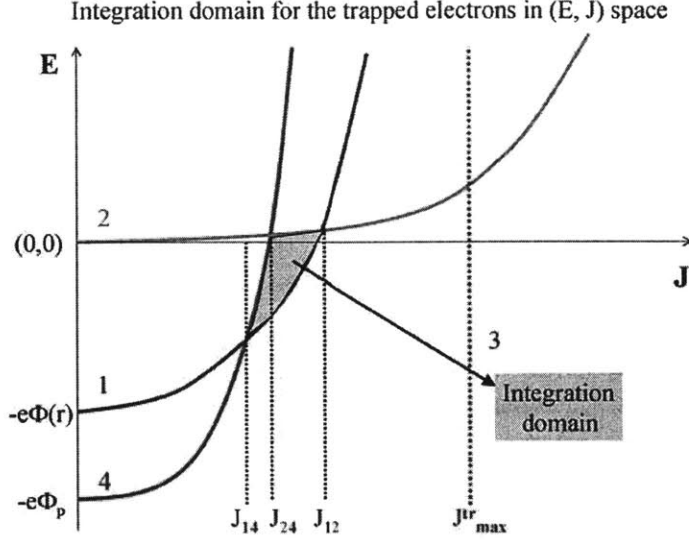


Figure 5-17: The integration domain could be plotted in (J^2, E) space, the parabolas becoming straight lines.

$E < \min_{R < r < R_s} [U_{eff}^J(R_s)]$ was obviously less stringent than condition 1. Indeed, this upper bound for the integration over J is redundant: it merely means that above a certain value J_{tr}^{\max} , the area of the integration domain vanishes at all radii.

The trapped electron density can now be written explicitly with the proper integration boundaries:

$$\frac{n_{etr}(r)}{n_\infty} = \int_{J_{14}}^{J_{12}} \int_{\frac{J^2}{2m_e r^2} - e\Phi(r)}^{\text{Min}\left(\frac{J^2}{2m_e R_s^2}, \frac{J^2}{2m_e R^2} - e\Phi_p\right)} \frac{\exp\left(-\frac{J^2}{2m_e R_s^2 k T_{e0}}\right) dE dJ}{\pi k T_{e0} \sqrt{J_r^2(E) - J^2}}, \quad (5.46)$$

where we operate the integration over J after the integration over E , since the latter actually depends on the variable J . Let us emphasize again here that $R_s(t_{trap})$ (cf. Appendix IV) should be used in the factor $\exp\left(-\frac{J^2}{2m_e R_s^2 k T_{e0}}\right)$, whereas $R_s(t_\infty)$ (after the transient) should be taken in the values of the boundaries (defined at the present time t_∞). Further analytical step cannot be performed without making the approximation (5.31). Without it, one cannot simplify the double integral, which must be then calculated fully numerically. Such a refinement could be

done easily, though, and compared to the following results. Hopefully, it will not exhibit too much discrepancy with our results.

Under the assumption 5.31, the inner E integration turns out to be analytically simple, with:

$$J_r(E) = 2m_e r^2 [E + e\Phi(r)], \quad (5.47)$$

yielding:

$$\int_{E_1^J}^{E_2^J} \frac{dE}{\sqrt{J_r^2(E) - J^2}} = \frac{1}{m_e r^2} \left(\sqrt{J_r^2(E_2^J) - J^2} - \sqrt{J_r^2(E_1^J) - J^2} \right), \forall (E_1^J, E_2^J) \quad (5.48)$$

Eventually, we get the following simple integral form for $n_{etr}(r)$:

$$\frac{n_{etr}(r)}{n_\infty} = \frac{1}{\pi k T_{e0} m_e r^2} \int_{J_{14}}^{J_{12}} \exp\left(-\frac{J^2}{2m_e R_s^2 k T_{e0}}\right) \sqrt{J_r^2(E_2^J) - J^2} dJ, \quad (5.49)$$

$$E_2^J = \text{Min} \left(\frac{J^2}{2m_e R_s^2}, \frac{J^2}{2m_e R^2} - e\Phi_p \right). \quad (5.50)$$

We can write it as two separate integrals:

$$\frac{n_{etr}(r)}{n_\infty} = \frac{1}{\pi k T_{e0} m_e r^2} \left[\int_{J_{14}}^{J_{24}} \exp\left(-\frac{J^2}{2m_e R_s^2 k T_{e0}}\right) \sqrt{\left(\frac{r^2}{R^2} - 1\right) J^2 - 2em_e r^2 (\Phi_p - \Phi(r))} dJ \right. \\ \left. + \int_{J_{24}}^{J_{12}} \exp\left(-\frac{J^2}{2m_e R_s^2 k T_{e0}}\right) \sqrt{2em_e r^2 \Phi(r) - \left(1 - \frac{r^2}{R_s^2}\right) J^2} dJ \right]. \quad (5.51)$$

As mentioned previously, some of the trapped particles actually have a positive energy. We are now able to separate the trapped population between positive and negative energy particles. The negative energy particle concentration in the sheath may be written from Equation 5.46, with the additional constraint $E < 0$ for the upper boundary of the inner integral. Note also, that the J interval must be restricted as well for negative energy particles: J_{12} must be reduced to $J = \sqrt{2em_e r^2 \Phi(r)} < J_{12}$, such that $J_r(0) > J$ for all J in the integration range.

Trapped Electron Density in the Sheath

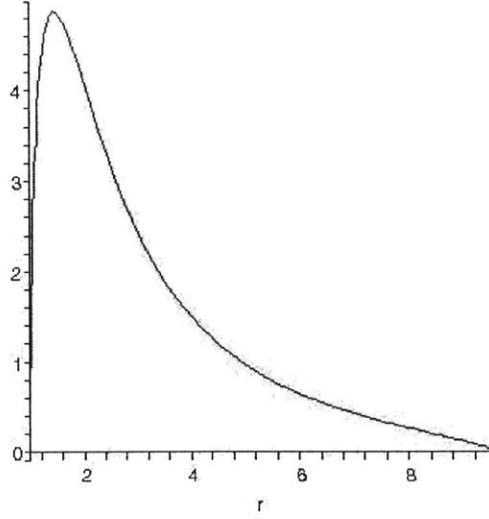


Figure 5-18: $\frac{e\Phi_p}{kT_{e0}} = 91; \frac{R}{\lambda_{De}}$ (and $\frac{R_s}{\lambda_{De}} = 9.5$). The total trapped population computed with negligible space charge in the sheath. (Equation 5.51). In the center of the sheath, the trapped density is much higher than the background density, even for a moderate bias, like here.

$$\frac{n_{etr}^-(r)}{n_\infty} = \int \int \frac{\text{Min}\left(0, \frac{J^2}{2m_e R^2} - e\Phi_p\right) \exp\left(-\frac{J^2}{2m_e R_s^2 kT_{e0}}\right) dE dJ}{\int \frac{J^2}{2m_e r^2} - e\Phi(r) \pi kT_{e0} \sqrt{J_r^2(E) - J^2}}, \quad (5.52)$$

which can be separated into two integrals over J , with the separating value $J_{sep} = \sqrt{2em_e R^2 \Phi_p}$

$$\frac{n_{etr}^-(r)}{n_\infty} = \frac{1}{\pi kT_{e0} m_e r^2} \left[\int_{J_{14}}^{J_{sep}} \exp\left(-\frac{J^2}{2m_e R_s^2 kT_{e0}}\right) \sqrt{\left(\frac{r^2}{R^2} - 1\right) J^2 - 2em_e r^2 (\Phi_p - \Phi(r))} dJ + \int_{J_{sep}}^{J_{12}} \exp\left(-\frac{J^2}{2m_e R_s^2 kT_{e0}}\right) \sqrt{2em_e r^2 \Phi(r) - J^2} dJ \right] \quad (5.53)$$

These integrals (Equations 5.51 and 5.53) for the trapped population are easy to evaluate numerically. They have been performed with Maple. Figures 5-18 to 5-20 show respectively the overall (regardless to the particle energy) trapped density, its negative energy component and its positive energy component.

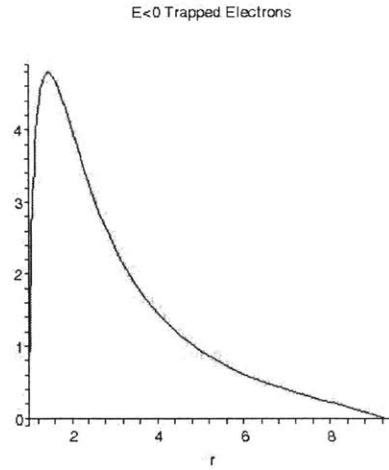


Figure 5-19: $\frac{e\Phi_p}{kT_{e0}} = 91; \frac{R}{\lambda_{De}}$ (and $\frac{R_s}{\lambda_{De}} = 9.5$). The $E < 0$ contribution represents most of the trapped population (computed from Equation 5.53). $E > 0$ electron trapping is then negligible.

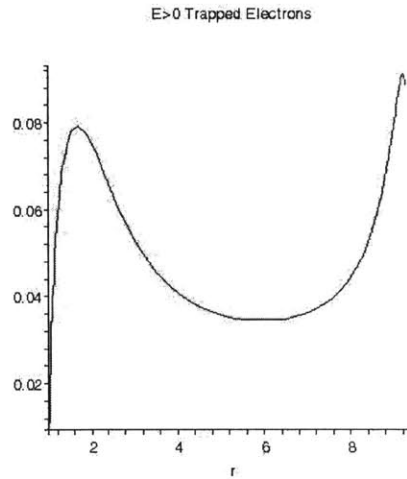


Figure 5-20: $\frac{e\Phi_p}{kT_{e0}} = 91; \frac{R}{\lambda_{De}}$ (and $\frac{R_s}{\lambda_{De}} = 9.5$). The $E > 0$ contribution is smaller than the $E < 0$ by two orders of magnitudes. It still exhibits a peak close to the tether surface. The increase towards the edge of the sheath (on the right) is probably due to the the inaccuracy of the Laplacian model for the potential.

Trapped Electron Density in the Sheath

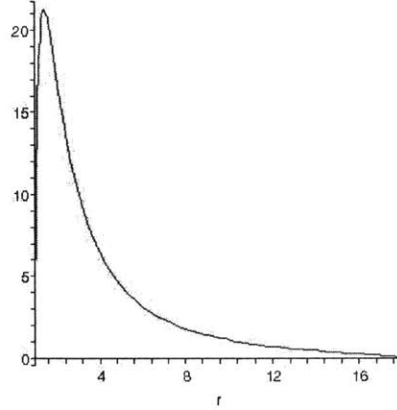


Figure 5-21: $\frac{e\Phi_p}{kT_{e0}} = 450$; $\frac{R}{\lambda_{De}} = 1$ (and $\frac{R_s}{\lambda_{De}} = 18$). When the bias gets higher (45V), the trapped density increases roughly in proportion.

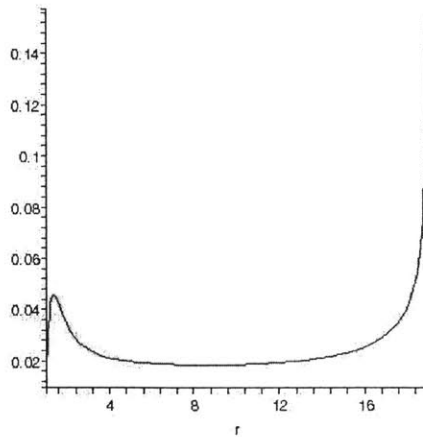


Figure 5-22: $\frac{e\Phi_p}{kT_{e0}} = 450$; $\frac{R}{\lambda_{De}} = 1$ (and $\frac{R_s}{\lambda_{De}} = 18$). However, $E > 0$ orbiters remain negligible for higher biases.

Remember that all these plots were obtained under the assumption that the space charge negative feedback effect on the potential was negligible, so we used a Laplacian potential approximation in the sheath to compute the density profiles. However, it turns out from Figures 5-18 and 5-21 that the ion depleted sheath contains a very high density of trapped electrons, larger than the background density by one order of magnitudes for high biases. This trapped space charge, which is much larger than the non-trapped one, might have a non-negligible shielding effect on the applied potential. Then, the local potential would be smaller than the Laplacian model we used, and less trapping would occur as a consequence. In order to find a much better approximation of the trapped population in the sheath than the previous plots, one should operate the following iterations:

1. Assume first a Laplacian potential in the sheath and compute the corresponding trapped population;
2. Calculate the first correction shielded potential, by solving Poisson's equation with RHS (source) equals to the trapped density found at step 1;
3. Take this first correction of the potential, to compute more accurately the trapped population;
4. Calculate a second correction of the shielded potential, etc.

This iterative process could be solved numerically, but solving Poisson's equation with more and more complex source terms and computing the density integrals with a complicated corrected potential could yield some numerical solving issues and be computationally costly.

In order to keep on developing this analytical model, we decided instead to deal with the first two steps only, and evaluate the first correction of the potential. Moreover, to allow a full analytical solution, we approximated the trapped density in the sheath by a simple fit. It turns out that a Gaussian function:

$$\frac{n_{etr}(r)}{n_{\infty}} \simeq \alpha \exp \left[-\frac{(r-R)^2}{\ell} \right] \quad (5.54)$$

can be used to fit the trapped density where its density is high and therefore exerts a stronger shielding on the potential. Of course, such an approximation *does not reproduce the overall behaviour of the trapped density profile*, which was found to vanish at the probe surface (this is obviously NOT the case for the Gaussian fit), but it turned out to be closer to the profile, than other fits, such as $\alpha(r - R) \exp\left[-\frac{(r-R)^2}{\ell}\right]$, and allows to solve analytically the 2D-axisymmetric Poisson's equation.

The best fit we found for the 9V biased tether is:

$$\alpha = 5 \quad (5.55)$$

$$\ell = 2.5 \quad (5.56)$$

Figure 5-23 shows how such an approximation fits the first approximation of the trapped density. The purpose of such a rough approximation is to yield an order of magnitude of the trapped space charge shielding effect on the potential. Using this Gaussian fit a the source term of the Poisson equation in the sheath, we get (non-dimensional)

$$\frac{1}{r} \frac{d}{dr} \left(r \frac{d\chi}{dr} \right) = -\alpha \exp \left[- \left(\frac{r - R}{\ell} \right)^2 \right], \quad (5.57)$$

where $\chi = \frac{\Phi}{T_{e0}}$, and the distances are non-dimensionalized by λ_{De} . We get then:

$$\frac{d}{dr} \left(r \frac{d\chi}{dr} \right) = -\alpha (r - R) \exp \left[- \left(\frac{r - R}{\ell} \right)^2 \right] - \alpha R \exp \left[- \left(\frac{r - R}{\ell} \right)^2 \right], \quad (5.58)$$

which can be integrated once directly between from R to r :

$$\frac{d\chi}{dr} = \frac{\alpha \ell}{2 r} \exp \left[- \left(\frac{r - R}{\ell} \right)^2 \right] - \alpha \frac{R}{r} \int_R^r \exp \left[- \left(\frac{u - R}{\ell} \right)^2 \right] du + \frac{Cte_1}{r}, \quad (5.59)$$

and a second time, given that $\int_R^r \exp \left[- \left(\frac{u - R}{\ell} \right)^2 \right] du = \ell \frac{\sqrt{\pi}}{2} \operatorname{erf} \left(\frac{r - R}{\ell} \right)$:

$$\chi(r) = \frac{\alpha}{2} \int_R^r \frac{\ell}{u} \exp \left[- \left(\frac{u-R}{\ell} \right)^2 \right] - \alpha \ell \frac{\sqrt{\pi}}{2} \int_R^r \frac{R}{u} \operatorname{erf} \left(\frac{u-R}{\ell} \right) du + Cte_1 \ln r + Cte_2, \quad (5.60)$$

Cte_1 and Cte_2 are easily determined by the boundary conditions:

$$\chi(R) = \chi_p; \quad (5.61)$$

$$\chi(R_s) = 0. \quad (5.62)$$

We get then:

$$Cte_2 = \chi_p \quad (5.63)$$

$$Cte_1 = \frac{\alpha \ell}{2 \ln R_s} \left[\sqrt{\pi} \int_R^{R_s} \frac{R}{u} \operatorname{erf} \left(\frac{u-R}{\ell} \right) - \int_R^{R_s} \frac{1}{u} \exp \left[- \left(\frac{u-R}{\ell} \right)^2 \right] du - \chi_p \right] \quad (5.64)$$

For the 9V bias ($\chi_p = 90$) and $R = 1$, we get numerically:

$$Cte_2 = 90 \quad (5.65)$$

$$Cte_1 = -41 \quad (5.66)$$

Figure 5-24 (green curve) shows a plot of $\chi(r)$ given from the first shielding correction (Equation 5.60). The result shows that the space charge shielding makes the potential drop below the Laplacian approximation. Iterating steps 2. and 3. is not worth the effort, for we got an upper bound of the actual shielding of the potential. Indeed, using a Laplacian model induces overestimation of the trapped space charge, and therefore an overestimation of the corresponding shielding. The actual potential, with full space charge accounting actually lies between a Laplacian model and the first approximation given above.

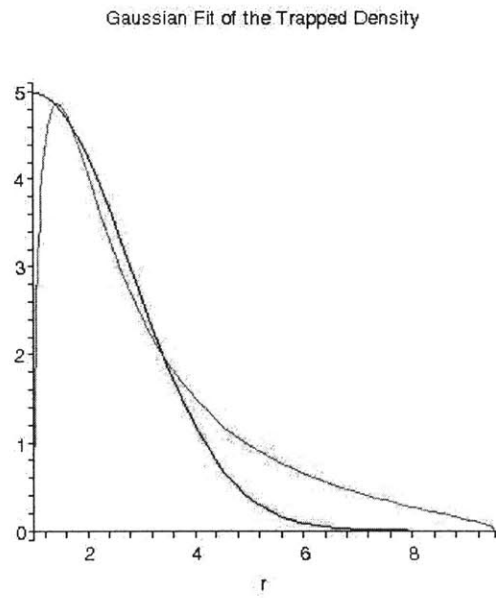


Figure 5-23: A Gaussian fit seems a sufficient approximation of the trapped density peak close to the probe. Since the actual density vanishes at the probe surface, this approximation should yield an upper bound of the space charge shielding effect.

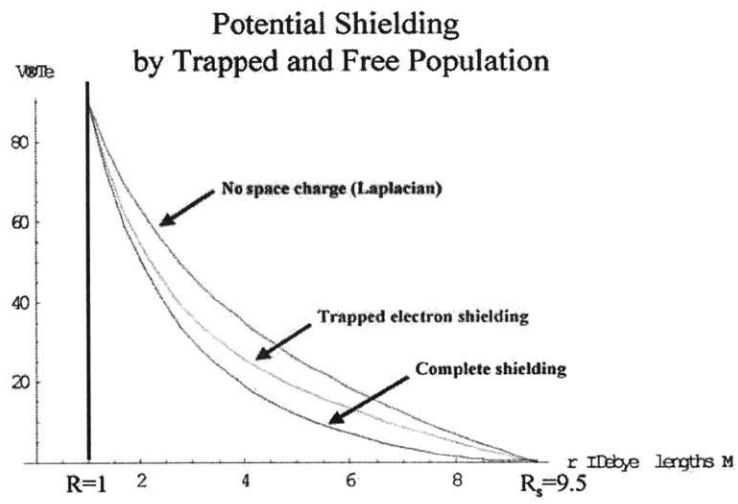


Figure 5-24: The shielding by the trapped population cannot be neglected, especially in the inner part of the sheath. However, this additional shielding maintains the potential in the OML condition (Equation 1.26), so it should not affect the current collection. Note that the shielding is here overestimated, for it is only a first correction of the potential (the actual trapped population density is smaller).

Note that the shielding due to non-trapped electrons in the outer part of the sheath should be evaluated as well. Indeed, the non-trapped density in the outer sheath is higher than the trapped density (much farther than the peak) and might be close to the background density. This effect acts in a large area, since it takes place at radii around $R \ll r \lesssim R_s$, which means that the effective shielding might be quite strong in the outer sheath. Figure 5-24 gives an evaluation of this effect, according to [19]Sanmartín approximation for the non-trapped density in the sheath:

$$\frac{n_e^{ntr}}{n_0} \simeq 1.08 \sqrt{\frac{R^2 \Phi_p}{r^2 \Phi(r)}} \quad (5.67)$$

Note that we could theoretically refine our Laplacian model and take a non-vanishing value of the potential at the sheath boundary (which is also more realistic, since $\Phi(r) = 0$ breaks the OML condition (1.23)) in order to maintain $\frac{n_e^{ntr}}{n_0} < 1$. Nonetheless, the numerical integration is still possible without such a refinement, which would anyway have an effect only close to the sheath limit.

These semi-analytical quantitative results have been supported by numerical measurements of the trapped population in our PIC simulations. It is computationally very costly to track all electrons in the sheath and determine from their trajectories which ones are actual orbiters, which ones are not. We took into account the facts that almost all orbiters have negative energy, as stated above, and that most $E < 0$ electrons are orbiters, since when the probe radius is small, only a tiny part of them is heading straight to the probe surface and will be captured. This was numerically verified by tracking many $E < 0$ particles and noticing that almost all of them were orbiting for many periods around the tether. Then, we measured at each time step the density of $E < 0$ electrons, which are much easier to define than actual orbiters (just compute their kinetic and potential energy...). We consider it to be a good approximation of the actual trapped population in the sheath in our "numerical experiments".

Figures 5-26, 5-27 and 5-28 show the results of simulation in OML conditions, for biases 9V and 45V respectively. These results correspond to time-averaged densities over thousands of time steps. Because of time fluctuations or the local potential, trapped electrons appear sporadically everywhere in the domain when the potential gets suddenly high in the whole

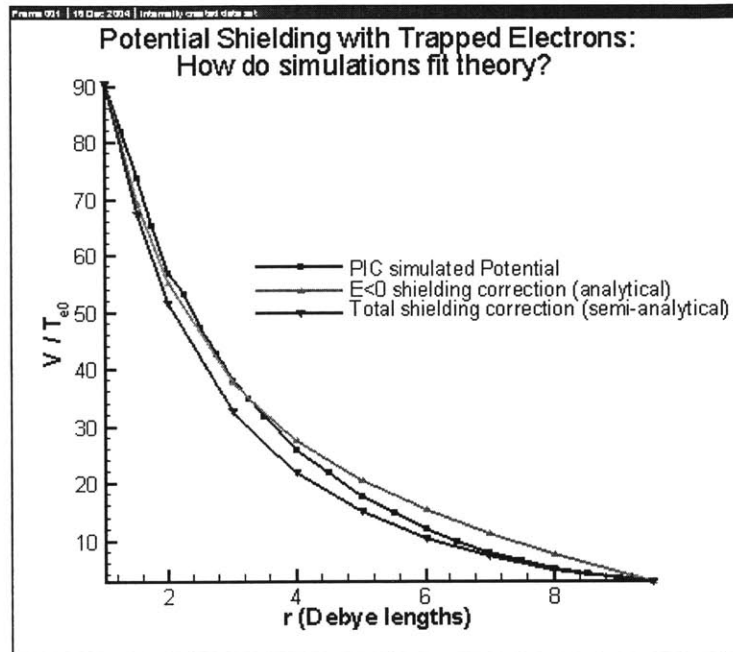


Figure 5-25: The semi-analytical shielded potential including trapping effects (blue curve) gives a good approximation of the potential measured from our PIC simulations (black curve). Since we overestimated the trapped population in our analysis, the actual (from simulations) shielding is lower than expected. Trapped electrons are instrumental in the inner sheath shielding and free electrons in the outer sheath shielding.

domain because of numerical fluctuations. This effect implies the time-averaged trapped density will never be zero, even very far from the tether or the boundaries. There is typically a noise level, which gets smooth by time-averaging: $\left\langle \frac{n_e^{trap}}{n_0} \right\rangle_t^{\min} \simeq 0.1 ; 0.3$. It was subtracted from plots 5-27 and . We observed a trapped density profile very similar to the semi-analytical results in Figures 5-27 and 5-28 : The trapped electron density vanishes at the absorbing probe surface, exhibits a sharp peak, much higher than the background density, close to the probe surface and then vanishes quickly, such that most of the trapped population lives in a few Debye length radius ring surrounding the probe.

However, the peak trapped density is much smaller than predicted by our semi-analytical results considering adiabatic trapping, by a factor 3 at least, in the studied cases. Plugging the actual potential to compute numerically the trapped population would yield lower densities. However, in the center of the sheath, where most trapping occurs, there is only a few percent difference between the Laplacian model and the actual potential. Such a slight difference would most probably not explain this factor 3 between simulation and semi-analytical results. We explain in the next section that depletion of the trapped population by numerical collisions occurs in our simulations, and lead to a steady trapped density profile which is not the one predicted by mere adiabatic trapping.

5.5 Detrapping and trapped population stability

5.5.1 Physical mechanisms

We have just shown that transient effects, occurring when the tether is switched on, trap many electrons which accumulate in the sheath. Their density may build up by orders of magnitude above the background density. Once a steady state has been reached, no more trapping should occur, since the potential hump motion has stopped. However rare they are, collisions on these trapped electrons should eventually perturb their trajectories, such that:

- either they get detrapped by taking some energy from another particle (they can then leave the sheath),

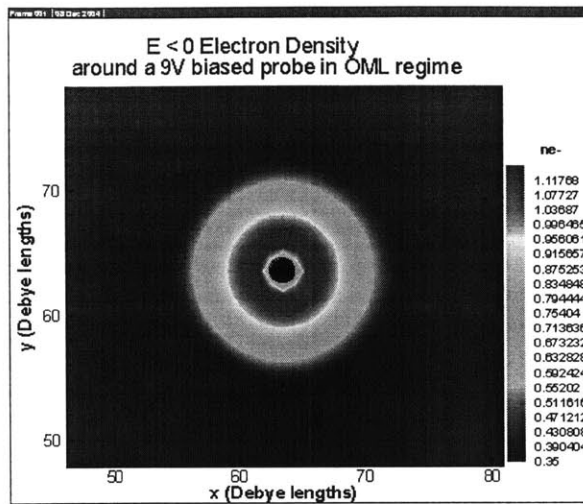


Figure 5-26:

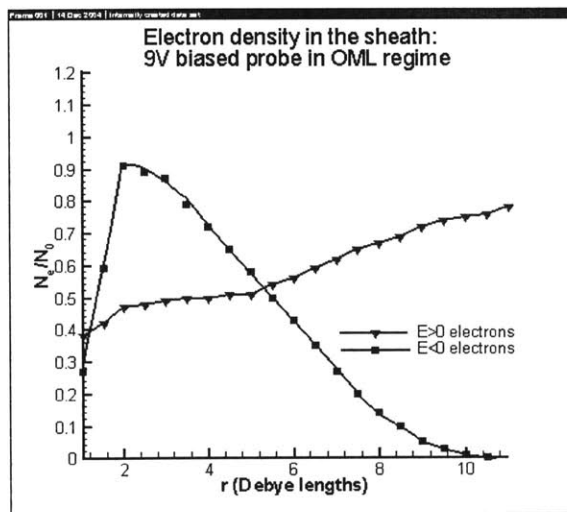


Figure 5-27: density profiles from our PIC simulations

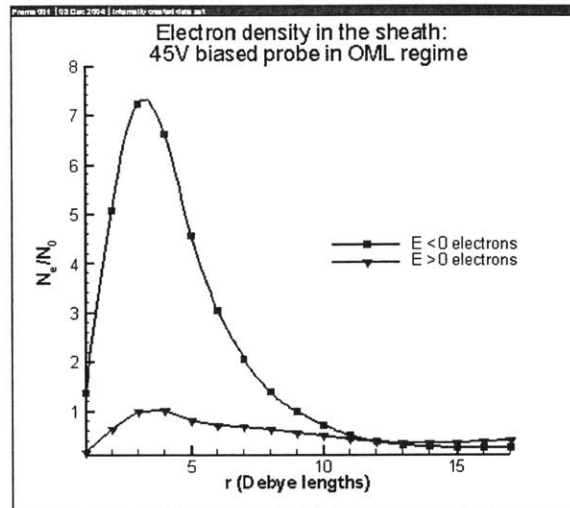


Figure 5-28: density profiles from our PIC simulations

- or they are scattered into the tether and captured, contributing then to current collection.

These two processes, whatever kind of collision produce them (with electrons, ions or neutrals; elastic or inelastic), would eventually completely deplete the electrons, which were trapped by adiabatic potential motion, if they were not be compensated by some new trapping.

Such physical collisional mechanisms have not been modeled in our PIC code, since their mean free path typically exceeds the domain size by orders of magnitude. Nonetheless, we were able to track some trapped electrons in the sheath, and found that their lifetime was not infinite. Actually, most trapped orbiters do not live more than a few hundreds of plasma periods in the sheath, and finally get captured are detrapped. Such a detrapping is due to the numerical artifacts in this case. Indeed, due to the finite number of particle per cell, the local potential is permanently oscillating at the plasma frequency, inducing numerical particle-field collisions, which have the same scattering effect as physical collisions. They might actually affect both momentum and energy of macroparticles, which means that they combine the effects of inelastic and elastic collisions. Moreover, the poor grid resolution compared to the tether radius produces some periodic energy oscillations for orbiters, as shown on Figures 5-2 and 5-3. This may considered as an effective numerical collisional effect as well.

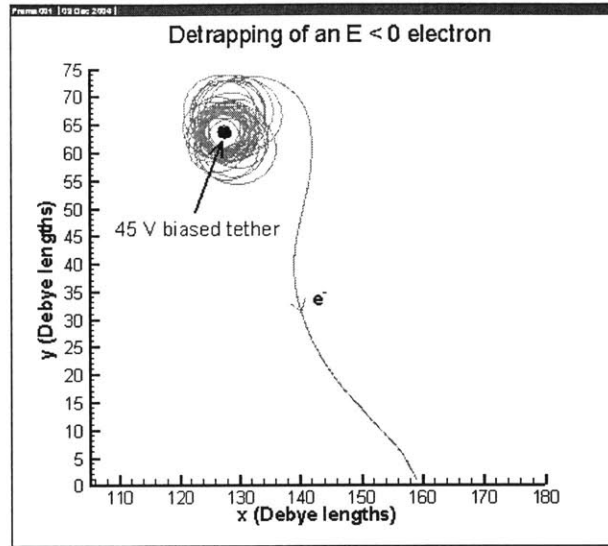


Figure 5-29: After orbiting many times around the tether, this trapped electron is scattered out of the sheath by numerical collisional effects.

Despite our relatively short-term simulation, compared with the time between any two physical collisions in the ionosphere, the trapped population lifetime cannot be considered infinite in our runs. The code turns out to be accurate enough to compute orbiters trajectories over hundreds of periods, but because their life is so long compared to the plasma period, numerical artifacts eventually act as effective collisions, which detrapp orbiters. These mechanisms would suggest that the trapped population would finally be cleaned out. Nonetheless, the trapped population density profile in the sheath, observed from the simulations seems really steady. So, electrons keep on being trapped after the initial transient, which compensates the loss due to collisional detrapping.

When a trapped electron is scattered into the probe, the shielding it was exerting on the tether potential vanishes. Then, the local potential $\Phi(r)$ everywhere (mainly in the sheath, though) *increases* by a small amount $\delta\Phi_{e^-detrapp}(r)$. This means that the potential energy of each electron in the domain *decreases* by $-e\delta\Phi_{e^-detrapp}(r)$. This feedback effect of detrapping on the potential occurs instantaneously when the trapped electron disappears, such that the

kinetic energy of each electron does not change in between Therefore, the total energy E of each electron at r decreases suddenly by $-e\delta\Phi_{e-detrapped}(r)$.

Electrons whose energy was close above the trapping energy (which as shown above is close to $0eV$, whatever the angular momentum J), might then be trapped if their energy drops below this threshold. So detrapping induces new trapping by means of potential feedback. It seems now clear that this mechanism is a good candidate to explain the robustness of the trapped population in the sheath, in spite of non-negligible collisional detrapping. However, one should verify if this feedback trapping is strong enough to compensate the losses in the trapped population. Only in this case would it be possible to get a steady-state non-vanishing trapped population at infinite times, both in the simulation and in the ionosphere. The intuition that such a balance is possible comes from the fact that the trapping due to the scattering and loss of a trapped orbiter depends proportionally on the collisional detrapping frequency, since the potential response $\delta\Phi_{detrapped}(r)$ to detrapping is proportional to the amount (the total charge) of lost orbiters.

M. Martínez-Sánchez proposed a few assumptions, which actually allow to find how the trapped population in the sheath may look like at collisional times . First, he neglected momentum change due to collisions, focusing only on the collisional sink effect. Keeping then the assumption of conserved momentum, and given that the (physical) collisional times are larger than the adiabatic time scale, we can still apply the adiabatic approximation for the Vlasov equation where J has been eliminated. One must not forget the existence of a collisional sink term on the RHS, though:

$$\frac{\partial f_{tr}}{\partial t} + \left\langle -e \frac{\partial \Phi}{\partial t} \right\rangle_{\tau} \frac{\partial f_{tr}}{\partial E} = -\nu f_{tr}, \quad (5.68)$$

where ν is the effective collision frequency, either numerical, or physical, including all kinds of collisions involving electrons. $\left\langle \frac{\partial \Phi}{\partial t} \right\rangle$ is the potential variation, due to the loss of trapped electrons (through collisions) only, averaged along one orbiter period. It does not include effects due to other changes in the space charge distribution. Therefore, $\left\langle \frac{\partial \Phi}{\partial t} \right\rangle_{\tau}$ can be calculated by considering the potential created by the trapped charge only.

The rotational symmetry makes the analysis easier. At a given time, consider an elementary ring of trapped electrons $[\rho, \rho + d\rho]$, which cross section area is $2\pi\rho d\rho$ and where the trapped density is $n_{tr}(\rho)$. For $r > \rho$, according to Gauss' theorem, with the boundary condition $\delta\Phi_\rho^{tr}(R_s) = 0$ (we assume that this effect is restricted to the sheath only), the space charge in this ring induces a potential:

$$\delta\Phi_\rho^{tr}(r > \rho) = 2[-en_{tr}(\rho) \times 2\pi\rho d\rho] \ln \frac{R_s}{r}. \quad (5.69)$$

Inside the ring, the charge in $[\rho, \rho + d\rho]$ does not have any effect on the potential, so $\delta\Phi_\rho(r < \rho)$ is constant. Using, the potential continuity at ρ , we get:

$$\delta\Phi_\rho^{tr}(R \leq r \leq \rho) = -4\pi e \rho n_{tr}(\rho) \ln \frac{R_s}{\rho} d\rho. \quad (5.70)$$

Then, an integration over the whole trapped population in the sheath yields:

$$\Phi^{tr}(r) = -4\pi e \times \left[\int_R^r \ln \frac{R_s}{r} \rho n_{tr}(\rho) d\rho + \int_r^{R_s} \ln \frac{R_s}{\rho} \rho n_{tr}(\rho) d\rho \right]. \quad (5.71)$$

Now, we consider time variations of the trapped density n_{tr} , and thus of the potential caused by the collisional detrapping of orbiters:

$$\left[\frac{\partial n_{tr}(\rho)}{\partial t} \right]_{detrapp} = - \iint_{E,J} \nu(E) \frac{f_{tr}(J, E, \rho)}{\sqrt{J_r^2(E) - J^2}} dJ dE. \quad (5.72)$$

Usually $\nu = \nu(E)$ depends on the particle energy (like numerical collisions for instance), at least, so we should keep the form:

$$\left\langle -e \frac{\partial \Phi}{\partial t} \right\rangle_{detrapp} = -4\pi e^2 \times \left[\ln \frac{R_s}{r} \int_R^r \iint_{E,J} \frac{\nu f_{tr} dJ dE}{\sqrt{J_r^2(E) - J^2}} \rho d\rho + \int_r^{R_s} \ln \frac{R_s}{\rho} \iint_{E,J} \frac{\nu f_{tr} dJ dE}{\sqrt{J_r^2(E) - J^2}} \rho d\rho \right], \quad (5.73)$$

which is a function of r only (it is already integrated over E and J):

$$-e \frac{\partial \Phi}{\partial t} = -g(r) \leq 0, \quad (5.74)$$

Now, we can deduct some features of the solution of the steady state version of Equation 5.68:

$$\frac{1}{f_{tr}} \frac{\partial f_{tr}}{\partial E} = -\frac{\nu(E)}{g(r)} \quad (5.75)$$

$$\ln [f_{tr}(r, E, J)] = -\frac{1}{g(r)} \int_{E_{\min}}^E \nu(E) dE + \ln [f_{tr}(r, E_{\max}, J)] \quad (5.76)$$

$$f_{tr}(r, E, J) = h(r, J) \exp \left[-\frac{1}{g(r)} \int_{E_{\min}}^E \nu(E) dE \right] \quad (5.77)$$

$$f_{tr}(r, E, J) = h(r, J) \exp \left[-\frac{\nu E}{g(r)} \right], \text{ for } \nu = cst. \quad (5.78)$$

At given r and J , the distribution in energy space can be easily computed from the collision function $\nu(E)$. For the simple case, where ν is constant in energy space, which might be a decent approximation for different collisions if the relevant energy range is not too large, we get an exponential dependence on energies for trapped particles at r with angular momentum r . Each (r, J) population can be considered as a (cut) Maxwellian energy distribution.

In order to solve easily Equation 5.68, we further make the assumption that the distribution function depends on E only when driven by collisions. This is probably inappropriate, as one may think from the form of f_{tr} during the adiabatic trapping without collisions (In Appendix IV, we show how f_{tr} depends on both E and J). However, such an approximation allows us to make further steps in the analysis and should eventually give a hint on whether collisions may renew permanently the trapped population or not.

Under this assumption, we can then redefine now $f_{tr} = f_{tr}(E, r)$, such that $n_e^{tr}(r) = \int f_{tr}(E, r) dE$. If we additionally assume a constant collision frequency ν , the analysis is much

more simple, since we can do the E integration inside the r integrals). Then, the steady-state Vlasov equation becomes:

$$-4\pi e^2 \times \left[\int_R^r \ln \frac{R_s}{\rho} n_{tr}(\rho) \rho d\rho + \ln \frac{R_s}{r} \int_r^{R_s} n_{tr}(\rho) \rho d\rho \right] \frac{\partial f_{tr}}{\partial E} = f_{tr}, \quad (5.79)$$

which can be integrated over the energy range:

$$-4\pi e^2 \times \left(\ln \frac{R_s}{r} \int_R^r n_{tr}(\rho) \rho d\rho + \int_r^{R_s} \ln \frac{R_s}{\rho} n_{tr}(\rho) \rho d\rho \right) [f_{ntr}(E_{\max}) - f_{tr}(E_{\max})] = n_{tr}, \quad (5.80)$$

where E_{\min} and E_{\max} are respectively the minimum and maximum possible energy of a trapped electron. The non-trapped distribution function value $f_{ntr}(E_{\max})$ must be used rather than $f_{tr}(E_{\max})$ since we get a flux from the untrapped to the trapped population. Note that $f_{ntr}(E_{\max}) \neq f_{tr}(E_{\max})$ only if no mixing in energy space occurs (inelastic collisions). $f_{ntr}(E_{\max})$ is known from the OML calculations (f_{ntr} is a depleted Maxwellian).

Let us now define the operator:

$$K(r, \rho) = \rho \ln \frac{R_s}{r}, \forall \rho < r \quad (5.81)$$

$$K(r, \rho) = \rho \ln \frac{R_s}{\rho}, \forall \rho \geq r. \quad (5.82)$$

Equation 5.80 becomes then:

$$\int_R^{R_s} K(r, \rho) n_{tr}(\rho) d\rho = \lambda n_{tr}(r), \quad (5.83)$$

where $\lambda = \frac{f_{ntr}(E_{\max}) - f_{tr}(E_{\min})}{4\pi e^2}$ is assumed here to be independent of time and radius in the collisional steady state. This assumption should be evaluated more carefully though in a thorough analysis. For this purpose, the connection between the trapped population distribution

f_{tr} and the untrapped one f_{ntr} should be analyzed, depending on the exiting mixing process (most collisions actually depend on energy, which would yield the continuity of the distribution at E_{\max}).

Equation 5.83 is an eigenvalue problem, for the eigenvectors $n_{tr}(r)$ and the corresponding eigenvalues λ of the operator K , which might have (non-zero) solutions $n_{tr}(r)$.

Because of the numerous assumptions (probably undermining any quantitative interpretation of the following results), this equation can actually be solved analytically. Let us derive differentiate Equation 5.83 with respect to r :

$$-\frac{1}{r} \int_R^r n_{tr}(\rho) \rho d\rho + n_{tr}(r) r \ln \frac{R_s}{r} - n_{tr}(r) r \ln \frac{R_s}{r} = \lambda \frac{dn_{tr}}{dr}; \quad (5.84)$$

$$\frac{R_s}{r} \int_R^r n_{tr}(\rho) \rho d\rho = -\lambda \frac{dn_{tr}}{dr}. \quad (5.85)$$

A multiplication by $\frac{r}{R_s}$ to eliminate it from the denominators, followed by another differentiation yield the simple expression:

$$rn(r) = -\frac{\lambda}{R_s} \frac{dn_{tr}}{dr} - \frac{\lambda r}{R_s} \frac{d^2 n_{tr}}{dr^2}, \quad (5.86)$$

which simplifies into:

$$\frac{d^2 n_{tr}}{dr^2} + \frac{1}{r} \frac{dn_{tr}}{dr} + \kappa^2 n_{tr} = 0, \quad (5.87)$$

a 0^{th} order Bessel equation, with parameter $\kappa = \sqrt{\frac{R_s}{\lambda}}$, whose general solution is:

$$n_{tr} = A \times J_0(\kappa r) + B \times Y_0(\kappa r), \quad (5.88)$$

where J_0 is the Bessel function of the first kind at order 0, and Y_0 the Bessel function of the second kind at order 0.

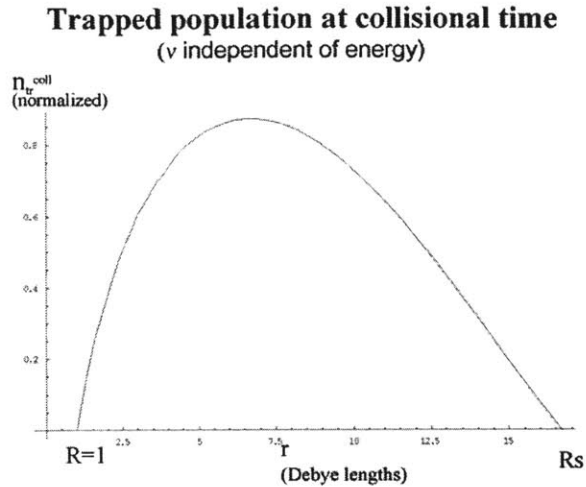


Figure 5-30: This trapped population profile can be sustained at collisional times, the depletion of trapped electron by collisions being then compensated by new trapping induced by the feedback on the electric potential. Note that this profile does not give a specific level of trapping in the sheath, but only how the radial dependence of n_{tr} should be in a steady state with energy independent collisions.

We shall now use the boundary condition $n_{tr}(R_s) = n_{tr}(R) = 0$, since the potential at these boundaries is fixed after the transient (which is actually not the case in our numerical PIC model), and thus no new trapping can occur there.

We get numerically: $\kappa = 0.19$, and $\frac{B}{A} = 0.88$. The corresponding trapped density profile is plotted in Figure 5-30, for the 45V biased probe ($R_s = 18\lambda_{De}$).

This means that there is a non-vanishing profile, which can result from collisional detrapping. With this specific profile, the depletion of the trapped population is perfectly compensated by new trapping due to the feedback of the detrapping on the potential.

This specific result is based on many assumptions, which are probably far from being verified, but it suggests anyway, that detrapping due to collisions probably do not deplete completely the adiabatically trapped electrons. We could expect the following steps for an electrodynamic tether, which is turned on in space:

1. During the potential switch, which is much slower than the typical electron motion near the probe, many electrons are adiabatically trapped, according to the "adiabatic trapping" section above. This phenomenon yields a dense and narrow distribution of orbiters in the sheath.
2. Then, at much longer times, collisions become relevant for long-life orbiters, which are progressively scattered into the probe (even by energy conservative elastic collisions)
3. However, such detrapping induces a decrease of the potential in the sheath, which traps new electrons. The distribution of trapped particles in the sheath "relaxes" in the sheath, until it gets to a profile, which allows the two mechanisms (detrapping and new-trapping) to compensate exactly. The existence of such a non-zero profile is suggested by the results of the paragraph above.

Note that collisional trapping, such as studied by [[35]]Lampe et al. might occur in the long term as well, but it is hard to evaluate for ionospheric electrons and is not required to get a non vanishing steady trapped population. We noticed occasionally in our simulations a few collisional trapping of particles, which got trapped when they entered the sheath, well *after the initial transient*. The importance of this effect, relatively to the stabilization process presented above has not been evaluated yet, though.

5.5.2 Numerical collisions and trapped population renewal in the simulations

Figure 5-31 shows that the electric field oscillates naturally around ω_{pe} and $2\omega_{pe}$, without external excitation. This effect decreases when the number of particles per cell is increased (typically, we cannot afford more than 36, though). These electric fluctuations "collide" with the particles, acting in a similar way as actual collisions. Due to the high fluctuation level in our simulations, the equivalent numerical collision frequency ν is much higher than for physical (electron-electron elastic, ion-electron and neutral-electron inelastic) collisions. This strong effect explains the fast renewal rate of the trapped population as shown below.

Note that numerical collisions are not completely similar to physical collisions. For instance, their frequency ν is inversely proportional to the number of macroparticles per cell :

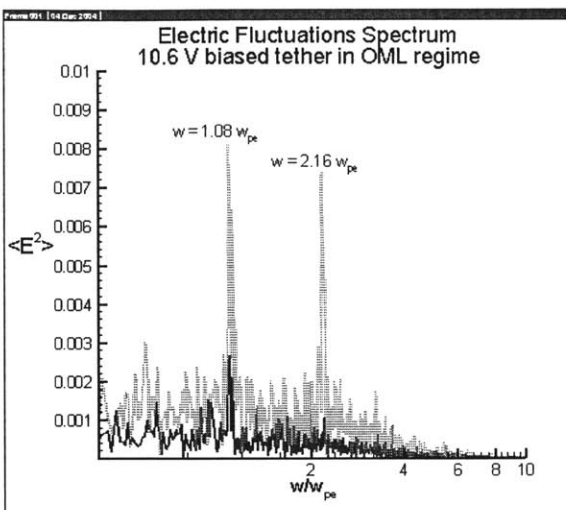


Figure 5-31: The time dependent electric field was measured in two cells, $10 \lambda_{D_e}$ and $40 \lambda_{D_e}$ respectively from the tether. A Fourier Transform allowed us then to get the spectrum, which exhibits two main peaks at the plasma frequency and its second harmonic. These fluctuations also occur in a non-perturbed domain (due to the finite number of particles per cell)

$$\nu \propto \frac{1}{n_{part/cell}} \quad (5.89)$$

Moreover, it is far from being independent of the particle energy. Typically:

$$\nu \propto \frac{1}{E} \quad (5.90)$$

In order to study the life time of trapped particles, we kept track of all $E < 0$ electrons in the sheath between two successive time steps. This allowed us to plot the rate of change within the trapped population located in the sheath, by measuring how many particles with $E < 0$ at step $n + 1$ were not trapped in the sheath at the previous time step n . Figure 5-32 shows this renewal rate. It turns out that within one time step, more than 50% of the $E < 0$ electrons are scattered out of the trapped population, or because they were captured by the probe, even because they were scattered out of the sheath. A thorough look at this plot shows that the rate is especially high close to the tether. This was expected, since particles orbiting very close to

the tether are much more likely to be quickly captured due to numerical collision effects. There seems to be a region, $r \in [5\lambda_{De}; 9\lambda_{De}]$ to the tether center, where the relative detrapping rate is higher (corresponding to the flat region on Figure 5-32), which means that trapped electrons orbiting in this area live longer there.

The important collisional renewal rate in the trapped population in the PIC simulations shows that the numerical collisions are not negligible with the chosen numerical parameters (16 particles per species per cell). Numerical collisions strongly affect the trapping process, even during the initial potential transient. This means, that we cannot clearly distinguish an adiabatic trapping time scale from a collisional renewal rate for the trapped population. Except for the first time steps, when the trapped population profile is quite narrow, the trapped population profile is then driven by the collisional trapping/detrapping rate, which yields a somewhat similar profile, with the same boundary conditions and a maximum close to the tether, but which is broader than expected from mere adiabatic trapping. In ionospheric conditions, inelastic collisions on electrons would have a similar effect to numerical collisions, inducing permanent renewal of the trapped population in the sheath, but the collision rate would be much smaller than the adiabatic time scale. In this case, the potential transient, when the power on the tether is turned on, would first trap electrons, and at longer times, rare collisions would relax the trapped population profile to a non-zero steady state, which might be different from the initial adiabatically trapped population.

In order to determine whether this renewal effect of the trapped population could be justified by numerical collisions, we evaluated it for different particle discretizations: 16 macroelectrons per cell (Figure 5-34) and 36 macroelectrons per cell (Figure 5-35). Since numerical collisions are mainly due to electric fluctuations at the electron plasma frequency, induced by the finite number of macroparticles per cell, the higher the number of particles per cell, the lower the numerical collision frequency. Figures 5-34 and 5-35 show surfaces of the trapped density, whereas the coloured contour represents the relative renewal rate $\frac{1}{n_e^{tr}} \frac{dn_e^{tr}}{dt}$, where the unit time is one time step $dt = 0.1\omega_{pe}^{-1}$. It seems that the renewal rate near the tether is lower for a lower collision frequency (more particles per cell, Figure 5-35): 15% per time step close to the surface in Figure 5-34, versus 5% per time step in Figure 5-35. Note that this phenomenon is difficult to analyze with much insight, such as evaluating quantitatively the dependence of the

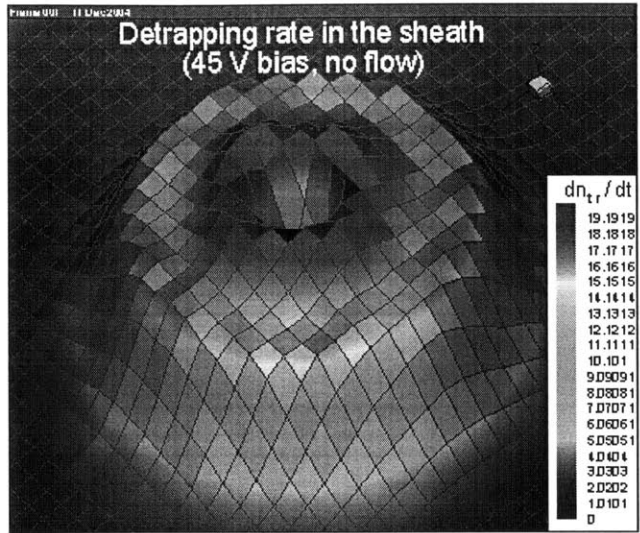


Figure 5-32: The rate of change in the trapped population is high due to numerical collisions (units: $w_{pe.n_0}$). Within a timestep around 50% of the trapped population is renewed.

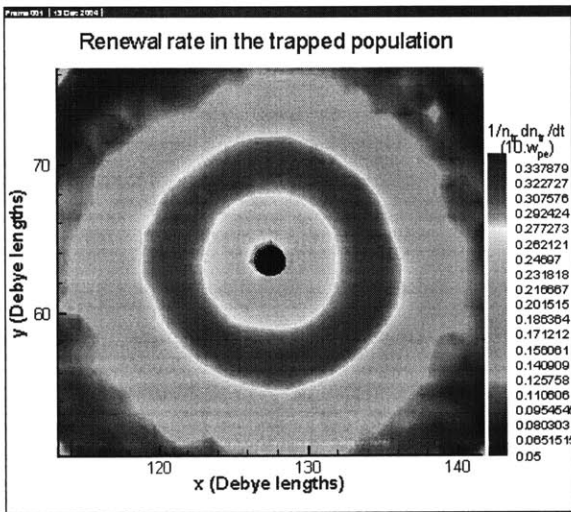


Figure 5-33:

renewal rate on the numerical collisions. Indeed, numerical collisions are also due to the mesh discretization, and changing the number of particles per cell seems to have some effects on the trapped population profile, as indicated by Figures 5-34 and 5-35. Therefore, our present assessments should only be considered as a qualitative analysis.

5.6 Current collection contribution

5.6.1 OML regime

During the potential transient, a trapped population builds up in the sheath. In both the non-flowing cases and flowing cases, the electric potential becomes stationary with respect to the plasma (in the sense defined by [[34]]Gurevich, 1968), when the transient period is finished, after thousands of plasma periods, say. Unlike, what might be inferred from [[2]]Onishi et al., there is no adiabatic trapping in the steady state, even with orbital velocity (or a flow onto the probe). Since the electron energy in the moving frame is conserved, they do not get trapped if the potential is steady in this frame. Orbiting around the probe is not a feature which depends on the reference frame. Indeed, the qualitative nature of motion holds in all reference frames, as long as their relative motion is a translation, which is the case for a constant satellite orbital velocity. So, no trapping occurs in the terrestrial frame as well. This means, that in both the no-flow and flow cases, adiabatic trapping only occurs during the initial transient when the power is turned on. The "potential motion" meant by [[34]]Gurevich (1968) are actual non-stationarities of the field in all Galilean referentials, which means either decay or growth. No qualitative difference in the electron trapping should then be expected between the no-flow and flow-cases.

In this steady state, the PIC simulations show that the trapped population density is stable and remains much higher than the background density after the initial transient, in spite of numerical collisional effects, which scatter trapped electrons into the tether or towards the edge of the sheath. Indeed, we have shown that any collisional detrapping is compensated by new trapping due to the detrapping-induced increase of potential.

Although the collision frequency does not have any effect on the trapped population density, it does of course have an impact on the amount of collected current, due to detrapped particles,

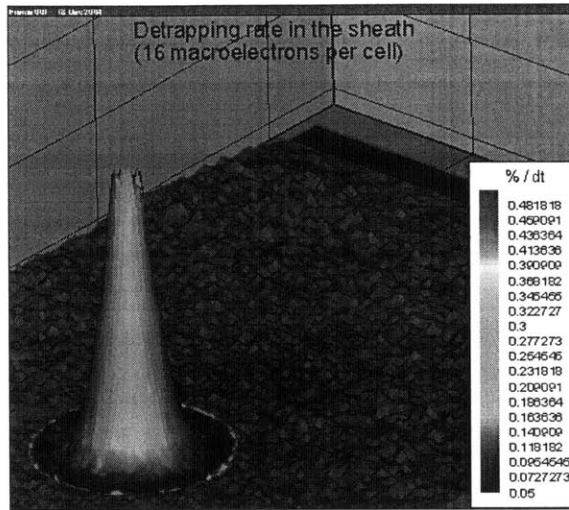


Figure 5-34: The 3D surface shows the trapped density, whereas the contour colour shows the renewal rate of the trapped particles.

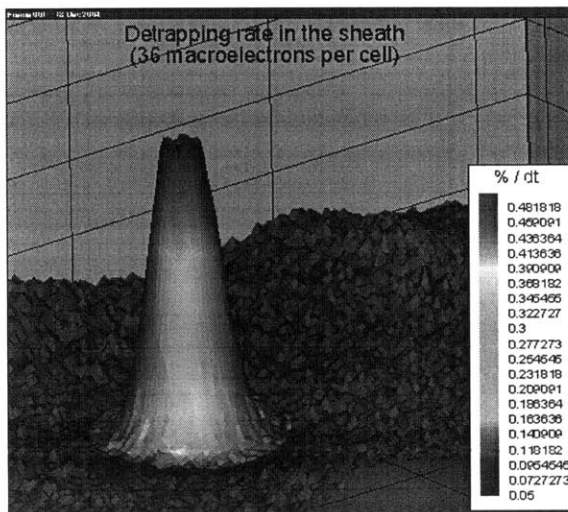


Figure 5-35:

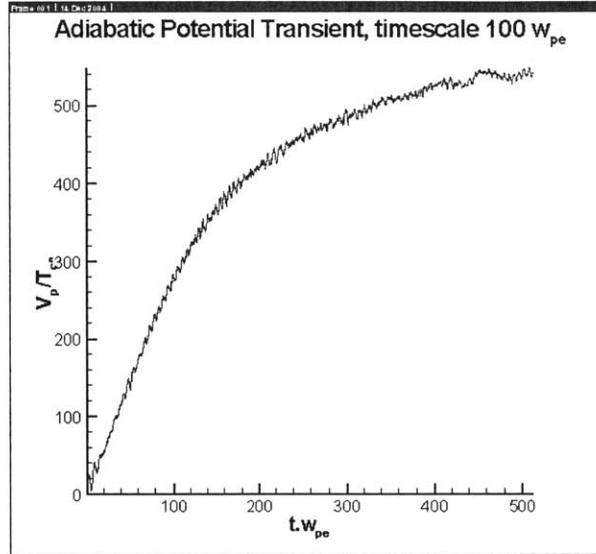


Figure 5-36: Example of a controlled potential transient in the simulation: the line charge at the tether follows the evolution: $q \left(1 - \exp\left[-\frac{t}{\tau}\right]\right)$, where the adiabatic timescale $\tau = 100\omega_{pe}^{-1}$ here. The fast bias oscillations at ω_{pe} are a numerical artifact (finite number of particles per cell, cf. paragraph on "numerical collisions")

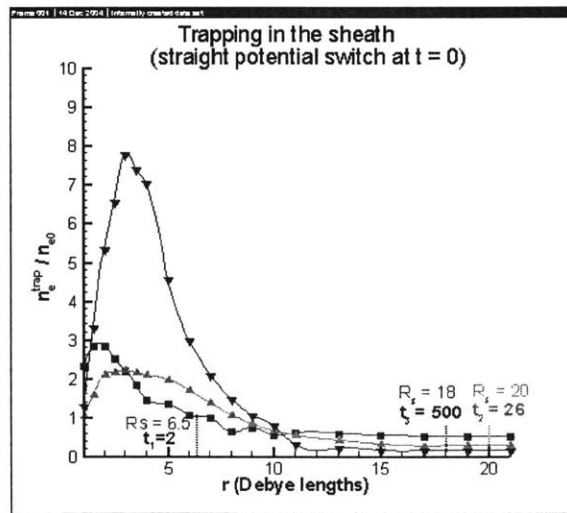


Figure 5-37: When the potential switch is suddenly turned on (maximum line charge at $t = 0$), important trapping occurs very quickly in the sheath, the relaxes due to numerical collisions (green Δ) before reaching a steady state profile probably driven by numerical collisions (blue ∇).

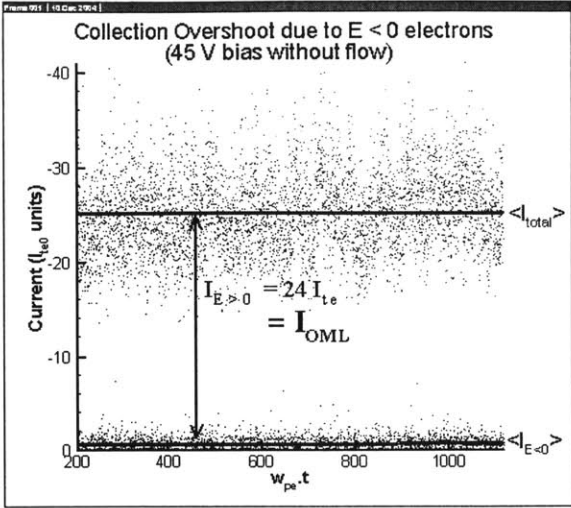


Figure 5-38: The total collected current and "E < 0 current" in steady state is shown. Both unaveraged raw data and means are plotted. The E < 0 is very small, but still explains the overshoot observed in Figure 3-23

which were eventually scattered to the probe surface. Given the fact that most of the trapped particles have negative energy as mentioned above, we may call conveniently this current "E < 0 current", which is proportional to the detrapping or collision frequency. This contribution to the collection has not been taken into account in the OML theory, where only $E > 0$ and non-trapped particles are considered to be collected. Therefore, we expect numerical collisions in the simulations to induce some overshoot in the collected current. Figure 3-23 shows clearly that we do get a time-averaged current that is slightly higher than the OML upper bound. This phenomenon could be due by the collection of $E < 0$ detrapped particles. In order to verify this hypothesis, we computed separately the current collection from $E < 0$ electrons. In all cases, this contribution represents only a few percent of the total current, and we could verify that the current actually produced by $E > 0$ electron collection was exactly the OML current, as expected. (Figure 5-38)

5.6.2 Ionospheric conditions

Orbital velocity effects

According to the previous remarks on the absence of adiabatic trapping in steady state, even with orbital velocity, we show here that the trapped population behaviour in our simulations seems very similar in the no-flow and flow cases.

Figure 4-10 shows that an 8km/s orbital velocity can enhance current collection by a factor 2, compared to the OML upper bound. In order to study the role of the " $E < 0$ " current in this case, we plotted separately the total current and the " $E < 0$ " contribution on Figure 5-39. The " $E < 0$ " current is of the same order of magnitude in this case as in the no-flow case, which could be expected since the same processes (numerical collisions, NOT adiabatic potential motion) are responsible for this current. Therefore, this effect cannot explain most of the enhancement due to the orbital velocity. This conclusion can be drawn as well from [1]Onishi's PIC simulations.

Since trapping does not seem to be the reason for observing current enhancement in the flow case, one should study more carefully how the ion density and temperature map, which are strongly non axisymmetric, affect electron motion near the tether. As mentioned by Sanmartín (unpublished), one should first take a non axisymmetric model of the ion temperature and re-derive analytically the particle densities and currents, which would be a first correction of the OML calculations in the axisymmetric case.

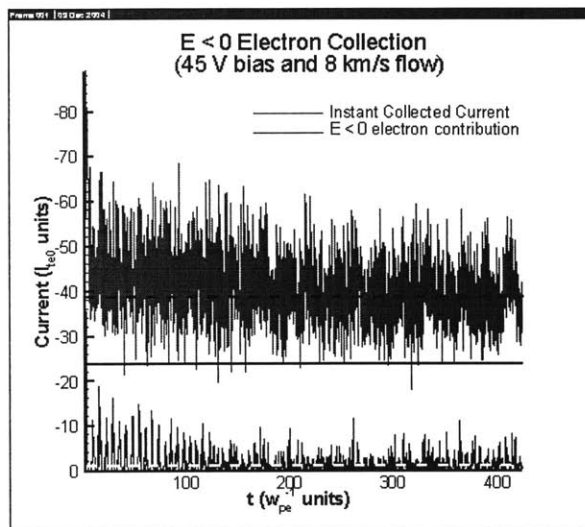


Figure 5-39: The OML current is shown with a solid line. The collection excess beyond this limit cannot be explained by a strong trapped particle current in the probe, since this current remains very low, like in the axi-symmetric case.

Chapter 6

Electric fluctuations and Plasma heating

When the tether potential is suddenly turned on at the start, the local potential increases suddenly everywhere in the domain, because the plasma does not introduce any shielding on the bias yet. This effect is instantaneous because the Poisson Solver suddenly has to solve the field consistently with the Van Neumann or Dirichlet boundary conditions. We mentioned previously that the tether does have a heating effect on the plasma in steady state, due to random accelerations of particles, which actually miss the probe. In order to understand how fast the temperature increases throughout the domain once the bias is turned on, some temperature measurements have been done at various times and distances from the tether (propagation seems roughly axisymmetric). Probe 1 was located at $15\lambda_{D_e}$ from the tether, probe 2 at $20\lambda_{D_e}$, probe 3 at $30\lambda_{D_e}$, probe 4 at $40\lambda_{D_e}$. These measurements are plotted on Figures 6-1 and 6-2. They show the propagation of a heat wave through the domain, which is actually very fast (one order of magnitude faster than the thermal velocity). This fast propagation is probably due to a very strong acceleration of all electrons in the domain at the start, when the potential is not shielded yet. This phenomenon cannot be physical, since the (numerical) bias switch actually takes place on a much slower time scale than the plasma frequency. However, this initial numerical artifact probably does not have long term effects on the simulation. Indeed, the temperature in the presheath scales fairly well with the potential there (Picture 3-18), as

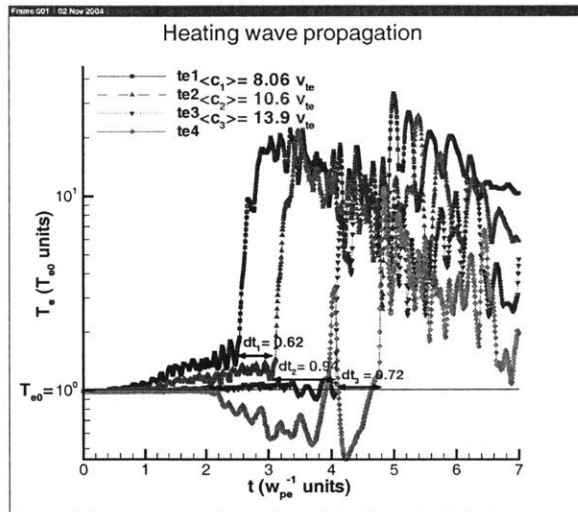


Figure 6-1:

expected from this heating mechanism.

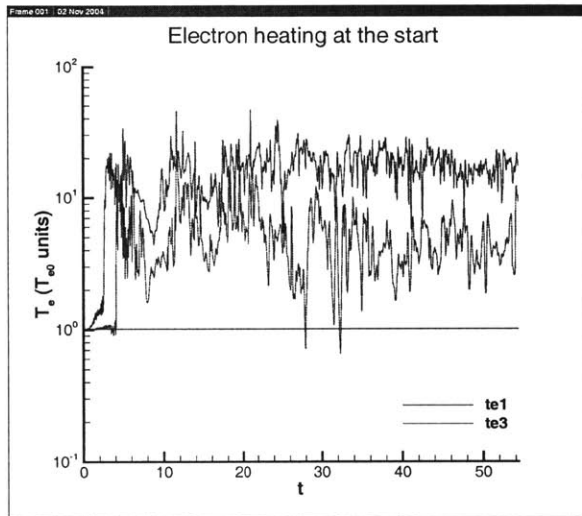


Figure 6-2:

Chapter 7

CONCLUSION

7.1 summary and contributions

A full PIC numerical model of an electrodynamic ionospheric tether (EDT) has been designed, which includes 3V kinetic modeling with proper boundary conditions, injecting a fully thermalized plasma into a two-dimensional domain. The model can now handle realistic ionospheric collection, with arbitrary orbital velocity and Earth's magnetic field configurations. Thanks to our Fast Poisson Solver, the whole plasma perturbation (including the wake) could be embedded in a large simulated domain, more than ten times larger than previous PIC models. Therefore, we believe the simulation results with plasma flow to be more reliable than previous works, since the whole plasma perturbation (including the wake) could be embedded in a steady self-induced field effects have also been implemented, and the capacity to simulate arrays of parallel wires.

The Orbit Motion Limited collection regime, which often prevails as the most accurate theory of electron collection by a positively biased probe, has been reproduced with satisfactory accuracy in the case of a $1\lambda_{D_e}$ probe in a stationary unmagnetized plasma. Although this upper bound applies to such a simplified case, we obtained a significant increase in the collected current, by simulating the effects of the satellite orbital velocity only. Such an enhancement had already been observed in previous numerical work, but we predict a strong enhancement up to twice the OML limit in the bias range $[10V - 90V]$, and probably much above. Some qualitative analysis of the physics of collection has been made in more refined conditions,

including the Earth's magnetic field and self-induced magnetic field, due to the current flowing into the tether. If, it is strong enough the latter is shown to change completely the particle orbits, and probably results in strong collection reduction.

The still incomplete theory of current collection has been further developed, by showing the existence of an important trapped population, which builds up during the potential transient (power switch). Our PIC simulations support this assertion, and show as well, that the OML regime remains valid under these conditions, although the plasma structure is significantly different from what was predicted in previous analysis. Because of the long life time of such orbiters around the probe, the long term effects of collisions on the trapped population had to be evaluated, even if collisional effects are usually neglected when considering particle with a short passing time in the probe region.

7.2 recommendations for future work

First, the analysis of the adiabatic trapping and collisional effects on the trapped electrons should be analyzed more carefully. The assumptions we made in our derivation are often not fully justified, and one should evaluate whether they actually matter or not. Some less analytical but more accurate description of trapping could be done easily with any numerical solver.

The problem we faced while trying to get some numerical evidence of this phenomenon is the difficulty in our PIC model to eliminate artifacts, which artificially detrap and trap particles in steady state, on a time scale, which is much shorter than could be expected from similar physical effects occurring in space (physical collisions). Then, we could not distinguish clearly in the simulations an adiabatic trapping regime, as presented in the analysis, from longer "collisional" times. Eliminating such artifacts seems a tough task today, given the limitations in particle resolution when one wants to simulate a large domain.

The trapped population stability issue should be handled more carefully as well, by evaluating what phenomena do matter in the ionosphere, and how they might sustain or not the trapped population distribution, which would be a nice refinement of our qualitative analysis and remarks.

Eventually, the many features of the PIC code should be used to evaluate these effects in more complex configurations. We expect the role of the self-induced magnetic field to be very influential on current collection, when the current flowing in the tether is high (say about $10A$). This effect could be even stronger than expected from analytical works, if an important electron confinement in the magnetic separatrix occurs and strongly shields the potential, as may be suspected from the few results we get under these conditions. Understanding such collection reduction effects would be instrumental in ED tether design, since it would provide limitations on the maximum current, one should expect to collect. Indeed, the more current you collect, the highest the collection reduction through self-field effects is. Although particle trapping does not seem to be change the current collection in the stationary and orbital velocity cases, it might though be influential in other regimes, when magnetic effects are considered, for instance if it provides a shielding, which is strong enough to limit the capture of free electrons by the probe.

Chapter 8

Appendix I: analytical potential for several charge distributions

The electric potential Φ in vacuum is solution of a Laplace equation:

$$\Delta\phi = 0 \tag{8.1}$$

We can then use the two-dimensional representation of the field by an analytical function (which expands into a series onto its whole domain) of a complex variable:

$$F(z = x + iy) = \phi + i\chi \tag{8.2}$$

where χ is the magnetic potential in the case of a current line.

8.1 Fields due to distributions of line sources (Morse and Feshbach, 1953)

Let us consider line sources as a simple model for an infinitely thin tether. The field due to a line source at $z = 0$ may be written in complex notation:

$$F(z) = -2q \ln z = -q \ln(x^2 + y^2) - 2qi \arctan(y/x),$$

where q is the unit charge per length.

For a finite distribution of tethers (unit charges per length: q_1 at $z_1 \dots q_n$ at $z_n \dots$), we have:

$$F(z) = -2 \ln \prod_i (z - z_i)^{q_i}$$

which allows to compute analytically the electric potential:

$$\varphi(z) = -2 \ln \prod_i |z - z_i^{q_i}|. \quad (8.3)$$

8.2 Infinite linear array of line sources

Because of our periodic boundary conditions along y , we can actually model infinite arrays of source lines with a constant distance l between them and a constant charge per unit length q .

For such a linear array, the analytical field function is:

$$F(z) = -2q \ln \left[2 \sin \left(i\pi \frac{z}{l} \right) \right],$$

from Morse and Feshbach (1953), p.1236, after a $+\pi/2$ rotation, yielding:

$$\phi(z) = -q \ln 4 \left[\sin^2 \left(\pi \frac{y}{l} \right) + \sinh^2 \left(\pi \frac{x}{l} \right) \right] \quad (8.4)$$

$$\chi(z) = 2q \arctan \left[\cot \left(\pi \frac{y}{l} \right) \tanh \left(\pi \frac{x}{l} \right) \right]. \quad (8.5)$$

At large distance from the grid of line charges, $\phi(z) \underset{y \rightarrow \pm\infty}{\sim} -\frac{2\pi}{l} q |y|$, which corresponds to a uniform electric field, such as is created by a charged plane. So, for a very large grid or parallel probes in vacuum, the extent of the electric perturbation is very large in the direction perpendicular to the grid as well.

8.2.1 Two-dimensional array of line sources

Exact analytical solutions using elliptic functions are given by Morse and Feshbach. No interesting collecting tether array configuration is available in their study, for they alternate positive and negative line sources. Still, they provide some interesting benchmarking data to make sure our code is able to simulate a multiple tether operation. For a tether array with alternating positive and negative line charge q or $-q$ (cf. Figure):

$$F(z) = 2q \ln \left\{ \operatorname{sn} \left[\frac{K}{l} z, k \right] \operatorname{sn} \left[\frac{K}{z} (z + a), k \right] \right\} \quad (8.6)$$

where sn is defined and K chosen as indicated in Morse and Feshbach (1953), p.487 and p.1239.

Note that only $\phi = \Re(F)$ matters for an electrostatic configuration, or self-field effects (magnetic field induced by the tether current) are neglected. Nonetheless, when we study self field effects, the induced magnetic field for such a distribution is:

$$B_x = \Re(\imath F') \quad (8.7)$$

$$B_y = \Im(\imath F'), \quad (8.8)$$

where F' is the complex derivative: $F' = \frac{dF}{dz} = \frac{\partial \Re(F)}{\partial x} + \imath \frac{\partial \Im(F)}{\partial y}$.

The charge density q_j must then be substituted by $4\pi\mu_0 I_j$, where I_j is the current flowing in the line j .

Chapter 9

Appendix II: Feedback control on the background density

We made an attempt to maintain the plasma density far from the probe at an expected level, by operating some feedback control on this density. The density of each species is measured regularly in the "density control stripes" and compared to the expected background plasma density. The incoming flux is then modified, i.e. increased if the measured density is too low and decreased if it is too high. This means that the incoming flux Φ_{in} is multiplied by a coefficient K_t , which is computed at each time step from the measured density. This process is actually done independently four times at each time step, in each "density control stripe" for each of the two species (ions/electrons). This is a very simple feedback control on incoming flux, with the density as input. Specific correction laws have to be chosen, indicating by how much the flux has to be modified for every possible measured density.

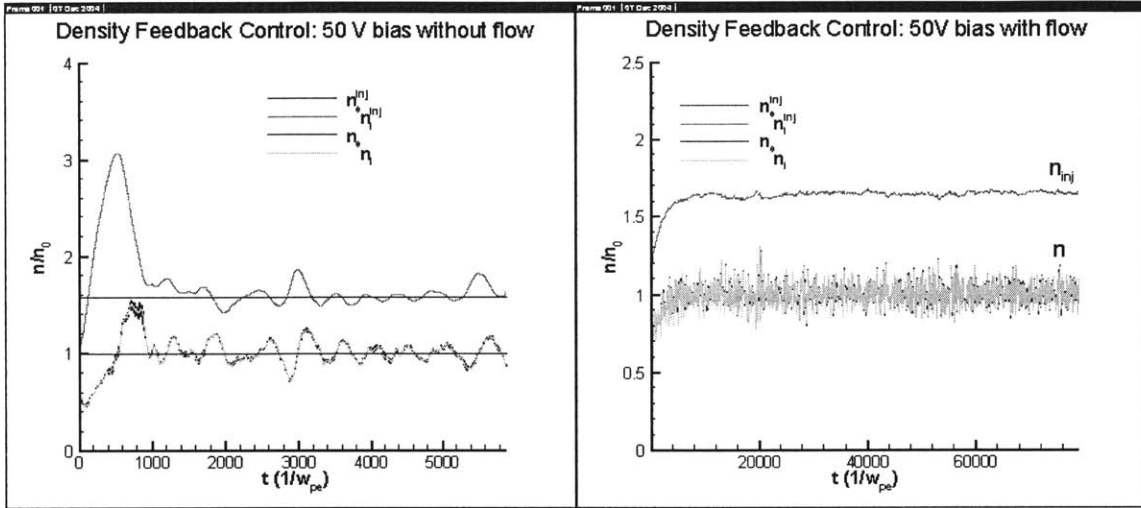
At each time step, K_{t+dt} is computed from K_t and the measured density n_t/n_0 . The flux is then computed according to $\Phi_{in}^{t+dt} = K_{t+dt} \cdot \Phi_{in}^t$.

Two kinds of corrections were implemented and tested:

- proportional: $K_{t+dt} = \lambda \left(\frac{n_t - n_0}{n_t} \right) K_t$
- power: $K_{t+dt} = \frac{K_t}{(n/n_0)^\alpha}$

Two parameters could be adjusted in these laws: the proportionality coefficient λ or the

power α and the number of time steps between each measurement and feedback. Both have effects on the stability and the time scale of the correction process. Figures...show density feedback control examples for the two kinds of corrections and various parameters. When the coefficient λ or α are empirically chosen in order to get stability, the control process turns out to be pretty slow and in all cases, when a steady state is obtained, the actual density fluctuates by around 10% within a short time scale (a few dozens of Langmuir periods) around the expected density, which seems to be a poor modelling of the background plasma.



We realized afterwards, that such poor results were due to an improper definition of the control laws. If one plans to operate such a feedback in a similar open system, one should build the following controller:

Measure the actual density far from the probe n_{far} , near the boundaries.

Evaluate the outgoing fluxes Γ_{out} at both right and left boundaries from the (measured) density far from the probe: $\Gamma_{out} = \frac{n_{far} \bar{v}}{4}$.

Operate an integral correction on the injected flux Γ_{in} , from the evaluated current error $\Gamma_{in} - \Gamma_{out}$.

This would lead a second order evolution law for the density (written as Laplace Transform):

$$\frac{n(s)}{n_0} = \frac{1}{1 + \frac{s \bar{v}}{\lambda 4} \left(1 + \frac{2L}{\bar{v}} s\right)} \quad (9.1)$$

where L is the characteristic length of the domain. The integrating feedback would allow to suppress the natural tracking error due to the control delay related to the non-zero characteristic length L . It should be both accurate and stable, provided that the evaluation of the flux at the boundary $\Gamma_{out} = \frac{n_{far} \bar{v}}{4}$ is a good approximation of the actual outgoing flux. Such an approach could be worked out further and compared to our "weight modification" method.

Chapter 10

Appendix III: Layered structure

Thin layers around the tether can be found, where the quasineutral solution for $\Phi(r)$ becomes singular. There, $n_e - n_i$ cannot be neglected anymore:

1. in the outer thin layer: $r \in [r_2, r_1]$
2. in the inner thin layer $r \lesssim r_2$, $\Phi(r) \propto (r_2 - r)^{4/3}$
3. near the tether, for $r \in [R, r_2]$, the space charge is negligible and we get Laplacian potential:

$$\Phi(r) = \Phi_p \left[1 - \frac{1}{\ln \sqrt{\sigma_1 \frac{e\Phi_p}{kT_i}} - b} \right] \ln \frac{r}{R}. \quad (10.1)$$

The position and width of these layers have been analytically calculated in [19]:. When $T_e = T_i$, their results yield:

$$r_2 \simeq r_1 \simeq 2\sqrt{\frac{e\Phi_p}{kT}} R \sim 20cm, \text{ for a } 0.1eV \text{ plasma and a probe radius } R = 1mm \text{ at } \Phi_p = 100V.$$

Therefore, we shall simulate a much larger domain to avoid strong boundary effects.

Chapter 11

Appendix IV: Calculation of $f_{tr}(E, J)$

Consider an (E, J) electron in the steady state t_∞ , after the transient time, when the potential has become stationary. It can be characterized by the adiabatic invariant: $I(E, J, \Phi_p)$ according to Equation 5.23, which has been conserved during the entire particle history, as long as the potential variation were slow. E, J, Φ_p indicate values at t_∞ .

When this electron was trapped, at the time t_{trap} , the bias and the sheath were different from the values at t_∞ (smaller in the case of our switch-on transient), $\Phi_p(t_{trap})$ and $R_s(t_{trap})$ respectively. However, we can use the conservation of I between the times t_{trap} and t_∞ . Since the angular momentum J has been conserved as well :

$$I(E, J, \Phi_p) = I[E_{\max}^J(t_{trap}), J, \Phi_p(t_{trap})] \text{ or} \quad (11.1)$$

$$I(E, J, \Phi_p) = I\left[\frac{J^2}{2m_e R_s(t_{trap})}, J, \Phi_p(t_{trap})\right]. \quad (11.2)$$

This relation, combined with Equation 1.11, relating R_s and Φ_p , can be solved to find $R_s(t_{trap})$ and $\Phi_p(t_{trap})$ as a function of E and J , and Φ_p . Eventually the limiting energy at the trapping time can be found:

$$E_{\max}^J(t_{trap}) = E_{\max}^J(E, J, \Phi_p). \quad (11.3)$$

Rigorously, this value, and not $E_{\max}^J(t_\infty)$ should be used to determine $f_{tr}(E, J)$, according

to the boundary condition 5.30:

$$f_{tr}(E, J) = f_{ntr}(E_{\max}^J(E, J, \Phi_p)) = \sqrt{\frac{m_e}{2\pi T_{e0}}} \exp\left[-\frac{E_{\max}^J(E, J, \Phi_p)}{kT_{e0}}\right]. \quad (11.4)$$

However, because of the complex integral form of the adiabatic invariant I , Equation 11.1 is not straightforward to solve. In the following, we present the simplifications proposed by M. Martínez-Sánchez in order to compute $E_{\max}^J(E, J, \Phi_p)$:

First, rewrite the adiabatic invariant, using the Laplacian model for the potential:

$$I(E, J, \Phi_p) = \sqrt{\frac{e\Phi_p}{\ln \frac{R_s}{R}}} \int_{r_1}^{r_2} \sqrt{\left(1 + \frac{E}{e\Phi_p}\right) \ln \frac{R_s}{R} - \frac{J^2}{2m_e r^2 e\Phi_p} \ln \frac{R_s}{R} - \ln \frac{r}{R}} dr, \quad (11.5)$$

or:

$$I(E, J, \Phi_p) = \frac{J}{\sqrt{2m_e}} \int_{\rho(r_1)}^{\rho(r_2)} \sqrt{\left(1 + \frac{E}{e\Phi_p}\right) \ln \frac{R_s}{R} - \frac{1}{\rho(r)} - \ln \frac{\rho(r)}{\rho(R)}} d[\rho(r)], \quad (11.6)$$

where we define the normalized radius $\rho(r) = \sqrt{\frac{2em_e\Phi_p}{J^2 \ln \frac{R_s}{R}}} r$. We define then:

$$\Gamma = \left(1 + \frac{E}{e\Phi_p}\right) \ln \frac{R_s}{R} + \ln \rho(R) \quad (11.7)$$

$\rho(r_1)$ and $\rho(r_2)$ are actually determined by the radii where the radial velocity direction changes. They are then the two positive solutions of the equation:

$$v_r(r) = 0 \quad (11.8)$$

$$\text{or } \Gamma - \frac{1}{\rho} - \ln \rho = 0, \quad (11.9)$$

they depend *only* on Γ :

$$\rho(r_1) = \rho_1(\Gamma), \quad (11.10)$$

$$\rho(r_2) = \rho_2(\Gamma). \quad (11.11)$$

We can now write:

$$I = I(J, \Gamma) = \frac{J}{\sqrt{2m_e}} \int_{\rho_2(\Gamma)}^{\rho_1(\Gamma)} \sqrt{\Gamma - \frac{1}{\rho} - \ln \rho} d\rho. \quad (11.12)$$

Since J and I are both invariants of the motion, this relation between I, J and Γ exclusively shows that Γ must be an adiabatic invariant as well, which is much simpler to evaluate for a given particle than the (integral form) I .

Let us write then the conservation of Γ along a trajectory, between the trapping time t_{trap} and the present time t_∞ after the transient, as we did above for I .

$$\Gamma(E, J, \Phi_p) = \Gamma[E_{\max}^J(t_{trap}), J, \Phi_p(t_{trap})]. \quad (11.13)$$

Plugging Equation 1.11 to eliminate $\Phi_p(t_{trap})$ and obtain an equation on $R_s^{tr} = R_s(t_{trap}) = R_s(E, J, R_s)$ (note that Φ_p appears, but can be written as a function of R and R_s through Equation 1.11 as well), we get eventually:

$$\ln \frac{R}{R_s^{tr}} + \frac{J^2}{2m_e k T_{e0} (R_s^{tr})^2} \times \beta (R_s^{tr})^{\frac{4}{3}} - \frac{1}{2} \ln \frac{J^2}{2m_e k T_{e0} R^2} \times \beta (R_s^{tr})^{\frac{4}{3}} = \left(1 + \frac{E}{e\Phi_p}\right) \ln \frac{R_s}{R} - \frac{1}{2} \ln \frac{2em_e R^2 \Phi_p}{J^2 \ln \frac{R_s}{R}}, \quad (11.14)$$

with $\beta \simeq 2.554$.

This non-linear equation should be solved numerically for every (E, J) in the integration range used to compute the trapped density. $E_{\max}^J(t_{trap}) = \frac{J^2}{2em_e (R_s^{tr})^2}$ could then be used in the integral form of the trapped density, allowing a complete and more accurate numerical calculation of the trapped density without space charge. However, in the Chapter "Particle

Trapping", we used the limiting energy value at infinite time $E_{\max}^J(t_\infty)$, which is lower than $E_{\max}^J(t_{trap})$. Since the factor $\exp -\frac{J^2}{2em_e(R_s^{tr})^2}$ in the expression of $f_{tr}(E, J)$ becomes very small for a small R_s^{tr} , the additional contribution to the trapped density integral 5.35, that was omitted by taking $R_s(t_\infty)$ should not change dramatically the numerical results. As it is the case in 1D (cf. [34]Gurevich,1968), and as we noticed a posteriori in our calculations (cf. Figures 5-22 and 5-20), almost all trapped electrons actually have a negative energy, although the limiting energies E_{\max}^J are always strictly positive.

Bibliography

- [1] T. Onishi, *Numerical Study of Current Collection by an Orbiting Bare Tether*, Ph.D. thesis, 2002
- [2] T. Onishi, M. Martínez-Sánchez, D.L. Cooke, J.R. Sanmartín, *PIC computation of Electron Current Collection To a Moving Bare Tether In the Mesothermal Condition*, 27th IEPC, Pasadena, California, USA, October 15-19, 2001.
- [3] J.B. Ferry, *Electron Collection by an Electrodynamic Bare Tether at High Potential*, M.S. thesis, 2003
- [4] O.V. Batishchev and M. Martínez-Sánchez, *Adaptive Mesh PIC and PIC-Vlasov Hybrid Methods for Space Electrodynamic Tether and Anomalous Transport Modeling*, p.391, 18th ICNSP, Cape Cod, 7-10 September, 2003.
- [5] J-M. Deux, O.V. Batishchev, M. Martínez-Sánchez, *Advanced Kinetic Model for Electrodynamic Space Tether*, Proc. 4th Intl. Space Prop. Conf., Cagliari, Italy, June 2-4, 2004.
- [6] J-M. Deux, O.V. Batishchev, M. Martínez-Sánchez, *Space tether current collection: an advanced kinetic model*, APS Bulletin 49 (8) 299, November 2004.
- [7] J. Rubinstein and J.G. Laframboise, *Upper bound current to a cylindrical probe in a collisionless magnetoplasma*, Phys.Fluids, 21, 1655, 1978
- [8] J.G. Laframboise, and L.W. Parker, *Probe design for orbit-limited current collection*, Phys. Fluids, 16, 629, 1973
- [9] Parker, L.W. and B. L. Murphy, *Potential buildup on an electron-emitting ionospheric satellite*, J. Geophys. Res., 72, 1631, 1967

- [10] Singh, Nagendra, W.C. Leung and B.I. Vashi, *Potential structure near a probe in a flowing magnetoplasma and current collection*, Journal of Geophysical Research, Vol.102, N0.A1,195-208, Jan.1997
- [11] G.V. Khazanov, N.H. Stone, E.N. Krivorutsky, K.V. Gamayunov and M.W. Liehmohn, *Current-produced magnetic field effects on current collection*, Journal of Geophysical Research, Vol.105, N0.A7,15,835-15,842, July 1, 2000
- [12] G.V. Khazanov, N.H. Stone, E.N. Krivorutsky and M.W. Liehmohn., *Current induced magnetic field effects on bare tether current collection: A parametric study*, Journal of Geophysical Research, Vol.106, N0.A6,10565-10579, June 1, 2001
- [13] J.R. Sanmartín and R.D. Estes, *Magnetic self-field effects on current collection by an ionospheric bare tether*, Journal of Geophysical Research, Vol.107, N0.A11,1335, doi:10.1029/2002JA009344, 2002
- [14] J.G. Laframboise and J. Rubinstein, *Theory of a cylindrical probe in a collisionless magnetoplasma*, Phys.Fluids, Vol.19, 1900, 1976
- [15] E.P. Szuszczewicz and P.Z. Takacs, *Magnetosheath effects on cylindrical Langmuir probes*, Phys. Fluids, Vol. 22 No.12, December 1979
- [16] D. Naujoks, *Charge shielding in magnetized plasmas*, Contrib. Plasma Phys. 41 (2001) 4, 375-386
- [17] J.G. Laframboise, *Current collection by a positively charged spacecraft: Effects of its magnetic presheath*, Journal of Geophysical Research, Vol.102, N0.A2, 2417-2432, February 1, 1997
- [18] J.V. Parker, *Collisionless plasma sheath in cylindrical geometry*, 1863
- [19] J.R. Sanmartín and R.D. Estes, *The orbital-motion-limited regime of cylindrical Langmuir probes*, Phys. Plasmas, Vol.6, No. 1, January 1999
- [20] R.D. Estes and J.R. Sanmartín, *Cylindrical Langmuir probes beyond the orbital-motion-limited regime*, Phys. Plasmas, Vol.7, No. 10, October 2000

- [21] F.F. Chen, C. Etievant and D. Mosher, *Measurements of low plasma densities in a magnetic field*, Phys. Fluids, Vol.11, No. 4, April 1968
- [22] J.R. Sanmartín and R.D. Estes, *Interference of parallel cylindrical Langmuir probes*, Phys. Plasmas, Vol.8, No. 9, September 2001
- [23] E. Choinière, B.E. Gilchrist and S.G. Bilén, *Enhancement of electrodynamic tether electron current collection using radio frequency power*
- [24] I.H. Hutchinson, *Principles of plasma diagnostics*, Cambridge University Press 1987
- [25] J.R. Sanmartín, *Active charging control and Tether*
- [26] E. Choinière and B.E. Gilchrist, *Modeling Long Probes in Flowing Plasmas using KiPS-2D, a Novel Steady-State Vlasov Solver*, 39th AIAA/ASME/SAE/ASEE Joint Propulsion Conference and Exhibit, 20-23 July 2003, Huntsville, Alabama
- [27] E. Choinière, B.E. Gilchrist, S.G. Bilén and K.R. Fuhrhop, *Measurement of Cross-Section Geometry Effects on Electron Collection to Long Probes in Mesosonic Flowing Plasmas*, 39th AIAA/ASME/SAE/ASEE Joint Propulsion Conference and Exhibit, 20-23 July 2003, Huntsville, Alabama
- [28] Yu.N. Grigoriyev, V.A. Vshivkov and M.P. Fedoruk, *Numerical "Particle-In-Cell" Methods, Theory and Applications*, VSP BV 2002
- [29] D.G. Swanson, *Plasma Waves*, Academic Press, Inc., 1989
- [30] J.D. Huba, 200 revised *NRL plasma formulary*, The Office of Naval Research
- [31] I.H. Hutchinson, *Ion Collection by a Sphere in a Flowing Plasma: 1. Quasineutral*, Plasma Phys. Control. Fusion **44** (2002) 1953-1977
- [32] I.H. Hutchinson, *Ion Collection by a Sphere in a Flowing Plasma: 2. Non-Zero Debye Length*, Plasma Phys. Control. Fusion **45** (2003) 1477-1500
- [33] I.H. Hutchinson, *Ion Collection by a Sphere in a Flowing Plasma: 3. Floating Potential and Drag Force*, Plasma Phys. Control. Fusion, still unpublished.

- [34] A.V. Gurevich, *Distribution of captured particles in a potential well in the absence of collisions*, Soviet Physics JETP **26**, 575 (1968)
- [35] M. Lampe, G. Joyce, G. Ganguli and V. Gavrishchaka, *Interactions between dust grains in a dusty plasma*, Phys. Plasmas, Vol.7, No.10, October 2000.
- [36] Z. Sternovsky, S. Robertson and M. Lampe, *The contribution of charge exchange ions to cylindrical Langmuir probe current*, Phys. Plasmas, Vol.10, No.1, January 2003.
- [37] M. Lampe, R. Goswami, Z. Sternovsky, S. Robertson, V. Gavrishchaka, G. Ganguli and G. Joyce, *Trapped ion effect on shielding, current flow, and charging of a small object in a plasma*, Phys. Plasmas, Vol.10, No.5, May 2003.